

2009

Annual Report Jahresbericht

Remote Sensing Technology Institute

Department
Atmospheric Processors



Published by	German Aerospace Center (DLR) A member of the Helmholtz Association
	Remote Sensing Technology Institute Institut für Methodik der Fernerkundung (IMF)
	Department Atmospheric Processors (IMF-AP)
Department Head	Prof. Dr. Thomas Trautmann
Editorial Team	Prof. Dr. Thomas Trautmann Dr. Manfred Gottwald Brigitte Rüba
Layout	Dr. Manfred Gottwald
Cover	Annual mean CO densities for the year 2004 as retrieved from SCIAMACHY measurements (see chapter 3.5). The sources of CO are both anthropogenic and natural in origin.

Contents

1.	Foreword	3
2.	Atmospheric Remote Sensing – Instrument Operation, Calibration and Measurement Techniques	5
2.1	The Multi-Axis DOAS Instrumentation for the Schneefernerhaus and for Mobile Applications.....	5
2.2	GOME Calibration & Degradation Monitoring together with Level 1 Data Reprocessing.....	9
2.3	SCIAMACHY Level 0-1b Improvements.....	12
2.4	SCIAMACHY Operations Support	14
2.5	SCIAMACHY Configuration in the Mission Extension Phase	19
2.6	CEOS Workshop on Sea Surface Temperature Sounding.....	21
3.	Atmospheric Remote Sensing – Retrieval Methods	24
3.1	O3M-SAF Retrieval of Water Vapour Column Amounts from GOME-2.....	24
3.2	GOME-2 Formaldehyde: A New Operational O3M-SAF Product	26
3.3	SCIAMACHY Level 1b-2 Processing.....	29
3.4	Improving Old and Implementing New SCIAMACHY Nadir UV-VIS Products	31
3.5	Carbon Monoxide and Methane Retrievals from SCIAMACHY Nadir IR Observations	33
3.6	Comparing Carbon Monoxide Retrievals from SCIAMACHY and AIRS Nadir Observations	36
3.7	Constrained Regularization Methods for Ozone Profile Retrieval from UV-VIS Nadir Sensors	39
3.8	Data Processing for Limb Emission Sounding.....	40
3.9	First Results of a Runge-Kutta Type Inversion Method for SCIAMACHY and IASI Retrievals	43
3.10	Radiative Transfer in Highly Variable Cloud Scenarios.....	47
3.11	PIRATES, the Programmer’s Interface to Radiative Transfer Algorithms.....	50
3.12	Multiple Scattering of Scalar Waves on an Ensemble of Non-penetrable Particles.....	52
3.13	Iterative T-Matrix Approach for Spheres with an Impressed Surface Irregularity.....	54
4.	Atmospheric Remote Sensing – Applications	56
4.1	Total Ozone Trends from the 14-Years GOME/SCIAMACHY/GOME-2 Data Record.....	56
4.2	Air Quality Measurements During the Beijing Olympic Games with GOME-2	60
4.3	Monitoring of Volcanic Sulfur Dioxide Emissions for Early Warning of Volcanic Hazards.....	63
4.4	SCIAMACHY and the Goddess of Love - Venus Observations from Earth Orbit	66
4.5	Modelling the Venus Spectrum as Observed with SCIAMACHY	70
4.6	ECMWF Surface Pressure Quality Analysis and its Impact on Gravity Field Determination	72
5.	Documentation	75
5.1	Books and Book Contributions.....	75
5.2	Journal Papers.....	75
5.3	Conference Proceeding Papers and Presentations	76
5.4	Attended Conferences and Professional Leaves.....	80
5.5	Diploma and Doctoral Theses.....	81
	Abbreviations and Acronyms	82

1. Foreword

The annual report of the year 2009 is again an attempt to summarize and describe the achievements of our department Atmospheric Processors (AP) of DLR's Remote Sensing Technology Institute (IMF) to the interested reader. It is a mix between operational tasks and research aiming at improving methods and knowledge in atmospheric remote sensing. The modified structure of the report reflects these activities by distinguishing between instrument operations and calibration, investigating new retrieval methods and finally scientific applications.

What were the highlights of the previous year? Certainly widening our GOME-2 data portfolio in the framework of the O3M-SAF was one of the main achievements. Of similar quality was the development and successful implementation of an improved processor for the retrieval of operational SCIAMACHY products as part of our involvement in the SQWG. These activities have a twofold benefit: They demonstrate our capabilities in atmospheric remote sensing and set the stage for acquiring interesting tasks in future atmospheric Earth Observation missions such as e.g. Sentinel-4 and 5 including its precursor. On the other hand they are needed for generating accurate long time series of geophysical parameters, a pre-requisite for space-borne investigations of our changing environment. This is nicely illustrated in one of the subsequent chapters where the timescales for detecting ozone trends are described. In the previous year we also participated in a rather unusual remote sensing activity – the observation of our solar system neighbour Venus with SCIAMACHY. It was by no means only an intellectual challenge for instrument operations but also delivered interesting spectral data from the atmosphere of another terrestrial planet.

While the annual report is always a once a year effort, we have now set up in addition a permanent AP related information channel. This is the ATMOS website (<http://atmos.caf.dlr.de/>) which was refurbished in 2009. Here we communicate past and present activities of our department.

We thank all our staff for their efforts and achievements in 2009 and their contributions to this annual report.

Prof. Thomas Trautmann
Dr. Manfred Gottwald

2. Atmospheric Remote Sensing – Instrument Operation, Calibration and Measurement Techniques

2.1 The Multi-Axis DOAS Instrumentation for the Schneefernerhaus and for Mobile Applications

P. Valks, N. Hao, T. Trautmann

Multi-Axis Differential Optical Absorption Spectroscopy (MAX-DOAS) is a novel technique to measure important stratospheric trace-gases (NO_2 , ozone, BrO and OCIO), as well as key tropospheric species, like NO_2 , ozone, SO_2 , formaldehyde, HONO and aerosols simultaneously. The MAX-DOAS instrument is based on an optical UV-VIS spectrometer that observes scattered sunlight from multiple viewing directions (fig. 2-1). Zenith sky measurements are usually performed during sunset and sunrise. Zenith measurements are mainly sensitive to stratospheric absorbers, while measurements close to the horizon have a long light path through the troposphere and are sensitive to tropospheric trace gases. By combining the zenith sky and horizon viewing directions, total trace gas amounts and vertical profile information can be derived from the recorded spectra, using the well-established Differential Optical Absorption Spectroscopy (DOAS) method (Platt 1994).

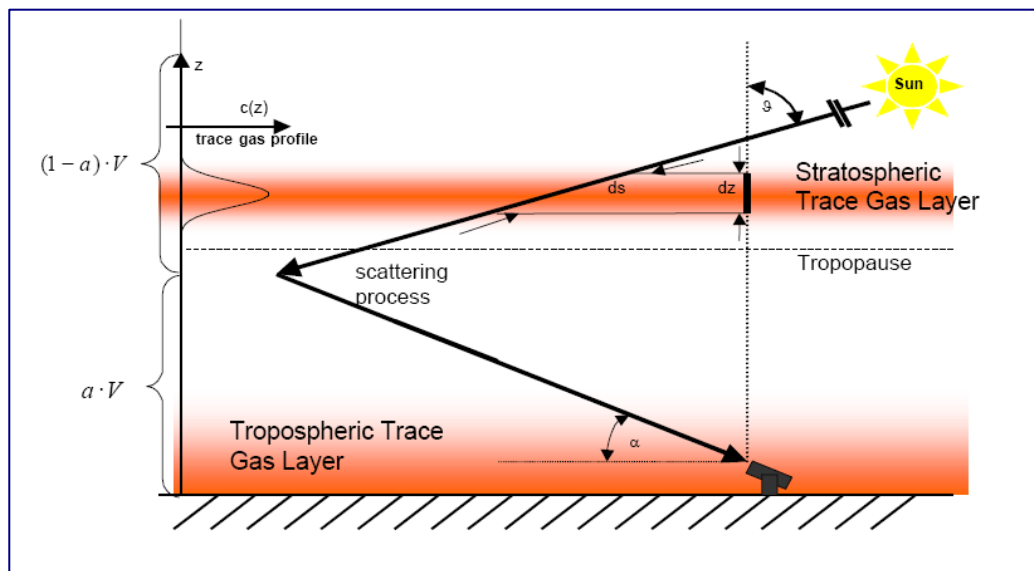


Fig. 2-1: Measurement principle of the Multi-Axis DOAS instrument. Adapted from Hönniger (2002).

Compared to traditional instruments such as the LIDAR and sun-photometer, the relatively new MAX-DOAS instrument has a much simpler construction (Hönniger 2002). Both the regular measurements as well as the calibration measurements of the MAX-DOAS instrument are fully automated, and the instrument can be remote-controlled via Internet link. This makes the MAX-DOAS instrument very suitable for building continuous and long-term measurement series.

MAX-DOAS instruments are used at several measurement-sites around the world to study the impact of anthropogenic activities on the atmospheric composition and air quality. Furthermore, MAX-DOAS measurements are invaluable for the long-term validation of satellite trace-gas measurements, such as those from the SCIAMACHY, GOME-2 and OMI instruments. From 2009 onwards, IMF-AP exploits two new MAX-DOAS instruments as described below.

MAX-DOAS instrument on the Schneefernerhaus observatory

In 2009/2010, a MAX-DOAS instrument is installed on the Environmental Research Station Schneefernerhaus (UFS, fig. 2-2), which is located at Germany's highest mountain Zugspitze (47°N, 10°E; 2650 m above sea level). The instrument is provided by the Institute of Environmental Physics (IFU) from the University of Heidelberg and will be exploited through a cooperation of IMF-AP and IFU, within

the framework of the UFS Development plan 2008-2011 (Bittner et al. 2008). The MAX-DOAS instrument consists of a weatherproof 2D Scanner including a telescope for both zenith/off-axis observations and horizontal scanning, three spectrometers to cover a large wavelength range (290-790 nm) and fiber bundles (fig. 2-3).



Fig. 2-2: The Environmental Research Station Schneefernerhaus at the mountain Zugspitze.

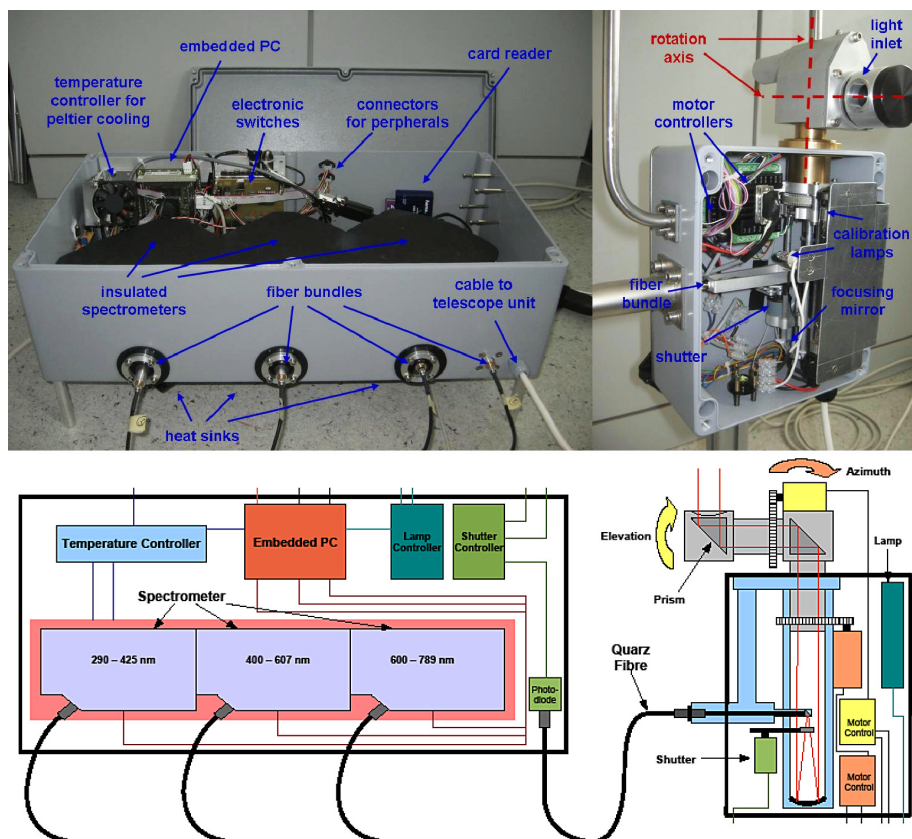


Fig. 2-3: The Multi-Axis DOAS instrument with three compact spectrometers (top) and a schematic view of the instrument (bottom).

The UFS mountain station is one of the few places in Germany and central Europe with (mostly) clean, unpolluted air (fig. 2-4), and is an optimal location for both stratospheric composition measurements as well as for trace gas measurements in the free-troposphere (between ~2-10 km altitude). Total column amounts of important stratospheric trace gases such as NO₂, ozone, OClO and BrO can be retrieved with high accuracy from the zenith-sky observations (Wagner *et al.* 2004). The DOAS measurements at UFS will provide valuable information on the stratospheric processes in the northern mid-latitudes, and will be used for the validation of SCIAMACHY and GOME-2 measurements of ozone, NO₂ and BrO. Another aim is to use the MAX-DOAS measurements for stratospheric trace gases monitoring within the Network for the Detection of Atmospheric Composition Change (NDACC).

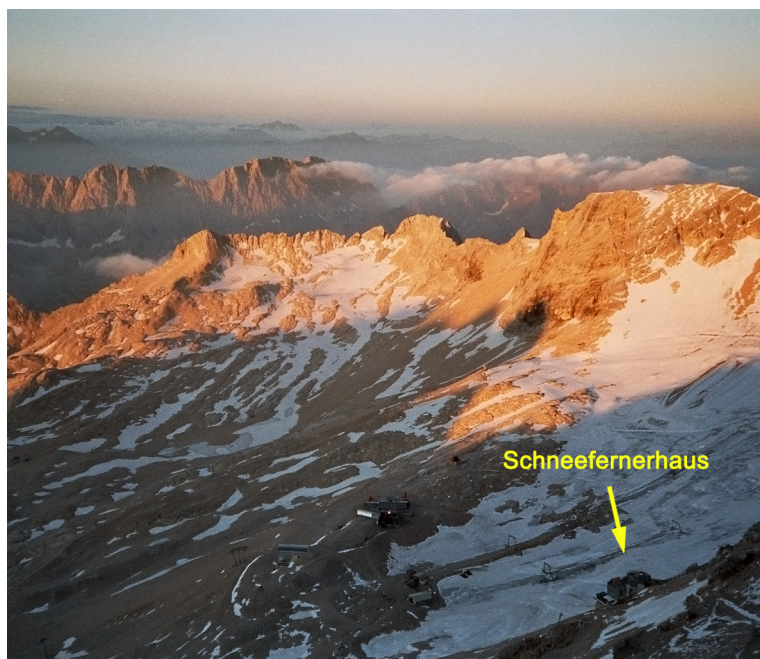


Fig. 2-4: The unspoiled view from the Schneefernerhaus.

Information on trace-gases in the free-troposphere (NO₂, ozone, HONO, formaldehyde and also BrO) can be retrieved from the off-axis measurements in the horizon viewing directions. The location of UFS at 2650 m altitude is optimal to detect pollution events in the free-troposphere. Although the free-troposphere is usually clean (in contrast to the polluted boundary layer below ~2000 m), significant enhancement of free-tropospheric NO₂ has been measured at UFS, which is an indication of short- or long-range transport (Richter *et al.* 2005). These free-tropospheric measurements are of great importance, since worldwide, only a very limited set of instruments deliver tropospheric profile information of NO₂ and ozone.

The retrieval of trace gas profile information from zenith and off-axis MAX-DOAS measurements involves complex radiative transfer calculations (Wagner *et al.*, 2004). The expertise at IMF-AP and the University of Heidelberg on radiative transfer modelling and regularization/inversion methods will be used to further improve the MAX-DOAS retrieval algorithms.

The MAX-DOAS observations will be investigated synergistically with other atmospheric trace gas observations at the Zugspitze, such as the FTIR measurements from the Karlsruhe Institute of Technology (Sussmann *et al.*, 2005). In addition, the measurements at UFS can be combined with the Brewer, LIDAR and sonde measurements at the nearby Hohenpeissenberg (OHP) observatory, and with the extensive set of regular in-situ trace gas and aerosol measurements at UFS and OHP. An important application of the synergetic use of these ground-based observations is the validation of tropospheric ozone and NO₂ measurements from the SCIAMACHY and GOME-2 satellite instruments.

Mobile mini MAX-DOAS instrument

In 2009, a compact and relatively small mini MAX-DOAS instrument, developed by the University of Heidelberg in cooperation with the Hoffmann Messtechnik GmbH, has been obtained by IMF-AP. The portable, low power automated properties make it ideal for long-term measurement at remote

locations, for example to monitor trace gas emissions from active volcanoes. Like all MAX-DOAS instruments, it is highly sensitive and allows specific detection of many trace gases and their vertical profile information; for instance SO₂, NO₂, HCHO and ozone.

The mini MAX-DOAS instrument consists of a hermetically sealed metal box containing entrance optics, fiber coupled spectrograph and all electronics (fig. 2-5). The total instrument has a weight of 4.5 kg and can be mounted on a standard tripod. The entire system operates on a standard car battery for about 24 hours.

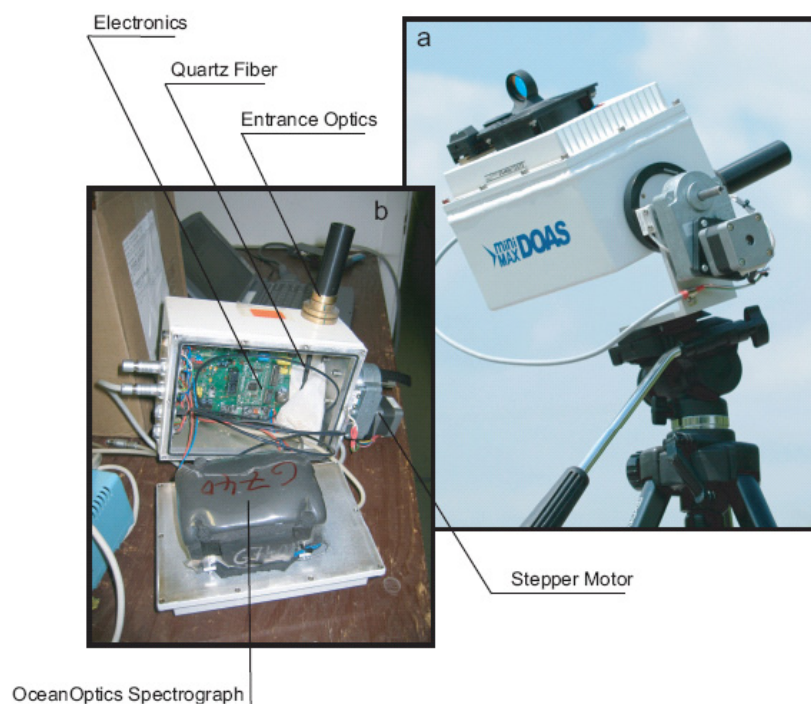


Fig. 2-5: Photographs of the mini MAX-DOAS instrument: (a) a mini MAX-DOAS instrument during measurements. (b) Main components of the mini MAX-DOAS system. Adapted from *Bobrowski and Filsinger (2005)*.

Most of the time, the mini MAX-DOAS instrument will be installed at IMF-AP in Oberpfaffenhofen (48°N, 10°E) for regular tropospheric NO₂ measurements, but it will be used for various measurement campaigns as well. From April to October 2010, the mini MAX-DOAS instrument will be installed in Shanghai during the World Exposition (Expo 2010). It is expected that the air pollution in Shanghai will be an important issue during the Expo 2010. Our MAX-DOAS measurements, together with other local in-situ and ground-based measurements, will be combined with SCIAMACHY and GOME-2 satellite measurements to provide a unique insight into the regional air quality around Shanghai and air pollution transport from surrounding provinces.

References

Bittner, M. et al.: Programmatische Ausrichtung des Virtuellen Instituts Umweltforschungsstation Schneefernerhaus (UFS) – Entwicklungsprojektplan – 2008-2011, Version 4.0, 2008

Bobrowski, N. and F. Filsinger: Mini-MAX-DOAS Manual, Institute of Environmental Physics, University of Heidelberg, 2005

Hönninger, G.: Halogen Oxide Studies in the Boundary layer by Multi Axis Differential Optical Absorption Spectroscopy and Active longpath-DOAS, PhD thesis, Heidelberg University, Germany, 2002

Platt, U.: Differential Optical Absorption Spectroscopy (DOAS). In M. W. Sigrist (Ed.), *Monitoring by Spectroscopic Techniques*. New York: John Wiley & Sons, Inc., 1994

Richter, A., R. de Beek, S. Fietkau, A. Heckel, A. Loewe, T. Medeke, H. Oetjen, M. Weber, F. Wittrock, and J.P. Burrows: Validation von SCIAMACHY level-2 Daten mit bodengebundenen DOAS-Messungen, Endbericht 50EE0005, 2005

Sussmann, R., W. Stremme, J. P. Burrows, A. Richter, W. Seiler, and M. Rettinger: Stratospheric and tropospheric NO₂ variability on the diurnal and annual scale: a combined retrieval from ENVISAT/SCIAMACHY and solar FTIR at the Permanent Ground-Truthing Facility Zugspitze/Garmisch, Atmos. Chem. Phys., 5, 2657-2677, 2005

Wagner T., B. Dix, C. v. Friedeburg, U. Frieß, S. Sanghavi, R. Sinreich, and U. Platt: MAX-DOAS O₄ measurements: A new technique to derive information on atmospheric aerosols – Principles and Information content, J. Geophys. Res., 109, D22205, 2004

2.2 GOME Calibration & Degradation Monitoring together with Level 1 Data Reprocessing

M. Coldewey-Egbers, B. Aberle, S. Slijkhuis, D. Loyola, P. Hoffmann (University of Leipzig)

Since 1995 GOME, the Global Ozone Monitoring Experiment, measures solar and backscattered spectra in the ultraviolet and visible wavelength range. The ground segment for the GOME instrument includes a Level 0-1 processing chain together with the archive of the entire GOME data set. Since a new version of the GOME Data Processor (GDP) for level 0-1 processing was implemented in 2009, this data set has been reprocessed using the new GDP version 4. The improvements of GDP 4 comprise

- update of degradation correction algorithm
- SAA avoidance
- dark signal correction
- spectral calibration and stability
- PPG correction
- adding cloud properties

Long-term monitoring of GOME's calibration and degradation properties (*Coldewey-Egbers et al. 2008*) was a pre-requisite for improving the level 0-1 chain.

Degradation

Sun mean reference spectra from 1997 to 2009 compared to the corresponding spectrum of 1996 (reference day is January 9th) show that in channel 1 (240-316 nm) the intensity decreased by 80-95% (see fig. 2-6). The decrease in channel 2 is still 40-80%, whereas the degradation in channels 3 and 4 is lower. In channel 3 the decrease started in 2001, when the Sun measurements were additionally affected by an ERS-2 pointing problem. The ratios exhibit several structures of high and low frequency. The high frequency residual is due to changes in the etalon structure in all channels, due to changes in dichroic structures in channels 3 and 4, and due to changes in the light source (the sun itself), mainly in channel 1. The low frequency structure can be described with polynomials for each channel. The correction algorithm for the channel degradation comprises two parts. First, each individual solar spectrum is fitted by polynomials in wavelength, and subsequently the time dependence of the polynomial coefficients is now described by a look-up-table. A low-pass filtering, which is defined as a weighted moving average with weighting given as a polynomial of degree 2 (Savitzky-Golay smoothing filter) is applied to the fitted coefficients. The look-up table contains approximately one set of correction coefficients per month for the whole period from July 1995 to October 2009.

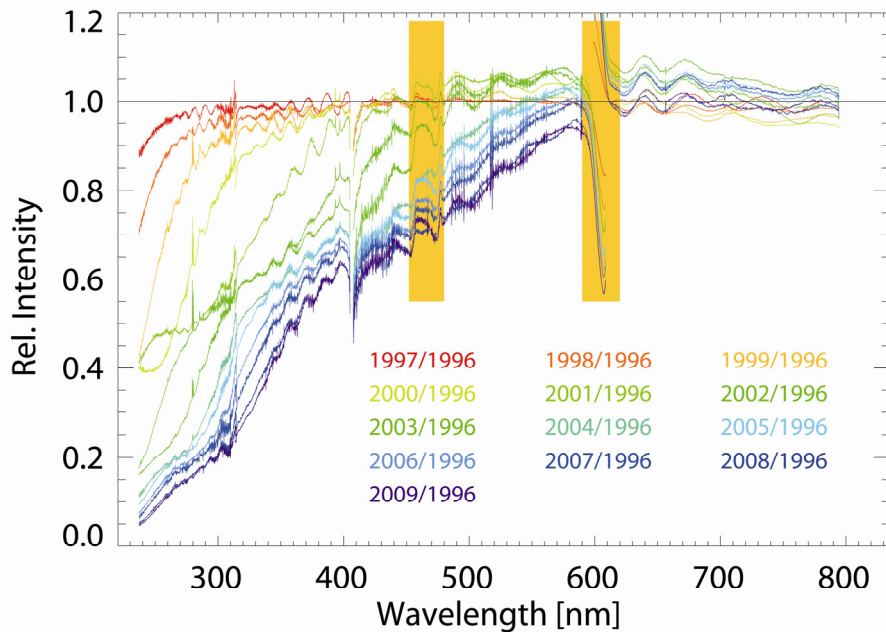


Fig. 2-6: Sun mean spectra of GOME from 1997 to 2009 compared to the corresponding reference spectrum from the 9th January 1996

PMD noise and South Atlantic Anomaly

The noise of the detector pixel readouts and the PMD noise level displayed a distinct seasonal cycle until June 2003 (see fig. 2-7, left panel). We identify this as influence of the SAA region, from which only few measurements were available after 2003 when the ERS tape recorder failed. For this reason, the updated version 4.0 of the GDP Level 0-1 processor includes an algorithm to automatically discard anomalous calibration measurements such as the ones over the SAA region – calibration packets are checked for the PMD noise, whether this value is below or above a certain threshold (see fig. 2-7). An overestimation of the dark current and the resultant underestimation of the real signal can be avoided thereby.

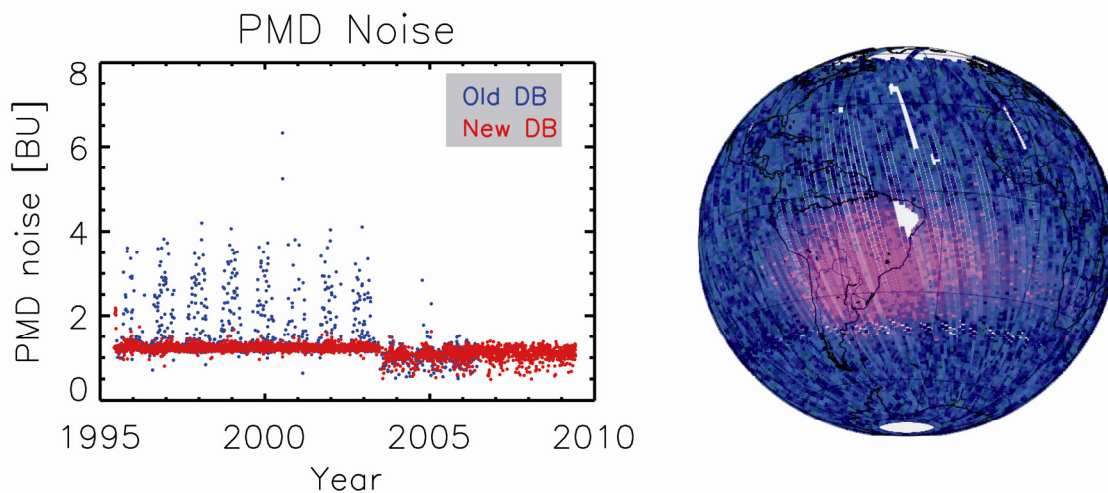


Fig. 2-7: Left panel: PMD noise values - new filtered version (red), and old unfiltered version (blue); right panel: PMD noise in July 2000 clearly outlining the SAA.

Dark current

The GOME detectors suffer from a certain amount of leakage current produced by thermal leakage. Dark measurements are taken every orbit on the eclipse side for all integration time patterns separately. The leakage current itself depends not only on the orbital position of the spacecraft, but also alters with the instrument's lifetime due to sensor degradation. Over the in-orbit lifetime an increase of the dark

signal is observed (fig. 2-8 top left). As this increase, measured in binary units (BU), is proportional to the integration time, the changes were converted to BU/s. For all time patterns similar values of 3.5-4.5 BU/s in 10 years were found with a maximum in channel 2.

Predisperser temperature

One of the key elements in the optical system of GOME is a quartz predisperser prism with a refractive index depending both on wavelength and temperature. Temperature variations are usually caused by seasonal variations, GOME's orbital position and by the rate of degradation of thermally sensitive optical elements. In operational processing the actual temperature selects the corresponding spectral parameters from the calibration database. Fig. 2-8 (bottom left) shows the time series of the predisperser temperature from 1995 to 2009 with an increase of ~3K due to degradation of the thermal system. Outliers below ~279K are connected to instrument and cooler switch-offs. Regular peaks of ~+1.5K denote temperature increase during the monthly calibration sequence.

PPG correction

GOME's individual detector pixels show slightly different sensitivities. This is compensated by deriving the pixel-to-pixel gain correction from LED measurements providing a uniform illumination. Measured signal values are then multiplied with those correction spectra. Since the tape recorder failure, LED measurements are limited to two or three spectra per year. When comparing channel wise the correction factors for individual years since 1995 it is obvious that their distribution becomes wider with increasing mission lifetime due to degradation (fig. 2-8 top right).

Spectral calibration stability

GOME allows spectral calibration via a PtCrNe hollow cathode emission lamp. Analysing the stability of all 65 selected atomic emission lines over the whole instrument's lifetime reveals that 9 of them are too unstable for an exact wavelength calibration. These spectral calibration lines were not used in GDP V4 reprocessing.

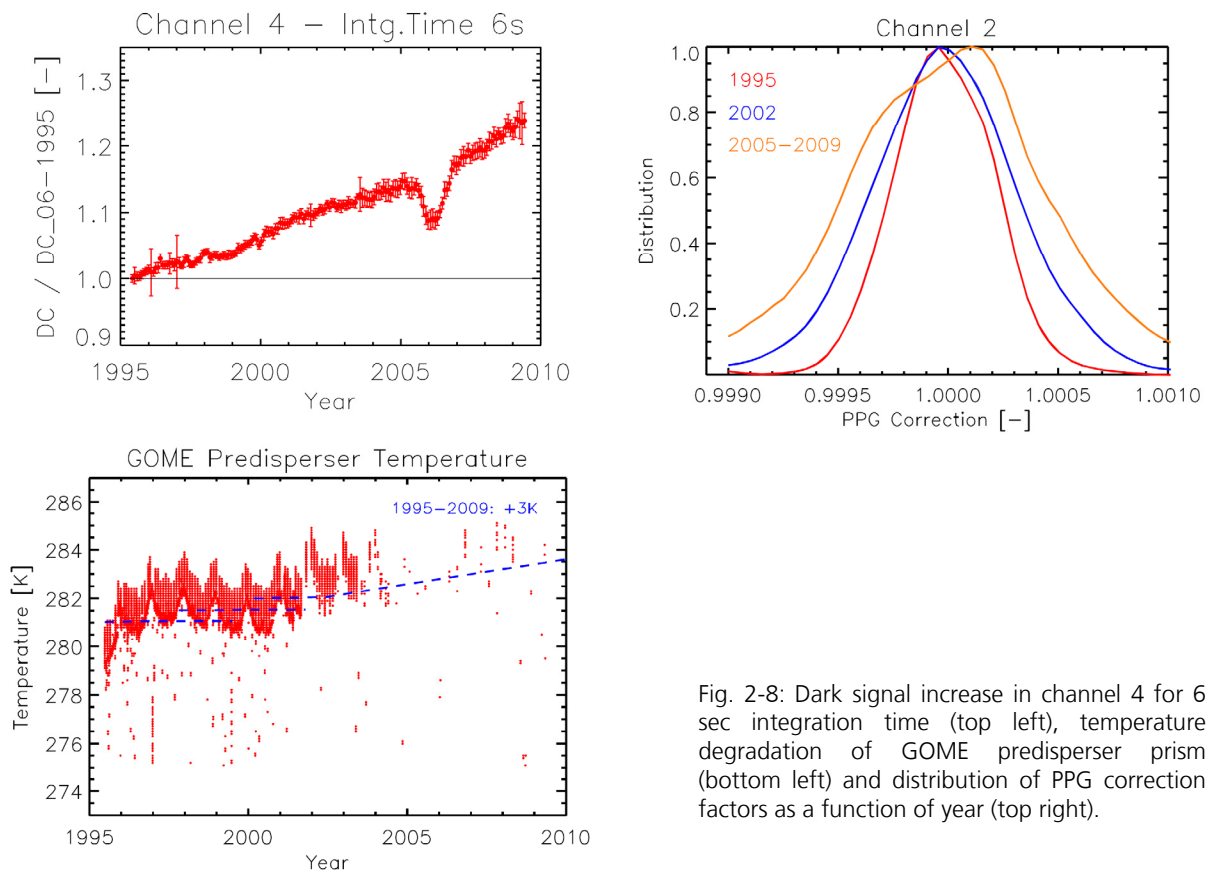


Fig. 2-8: Dark signal increase in channel 4 for 6 sec integration time (top left), temperature degradation of GOME predisperser prism (bottom left) and distribution of PPG correction factors as a function of year (top right).

Added cloud information

The new GOME level 1 product contains the three cloud parameters derived from GOME (fig. 2-9) and needed for trace gas retrieval: cloud fraction, cloud-top pressure (height) and cloud optical thickness (cloud-top albedo). These parameters are retrieved with the OCRA/ROCINN (Loyola *et al.* 2007) algorithms used since 2004 for the operational level 2 total column products.

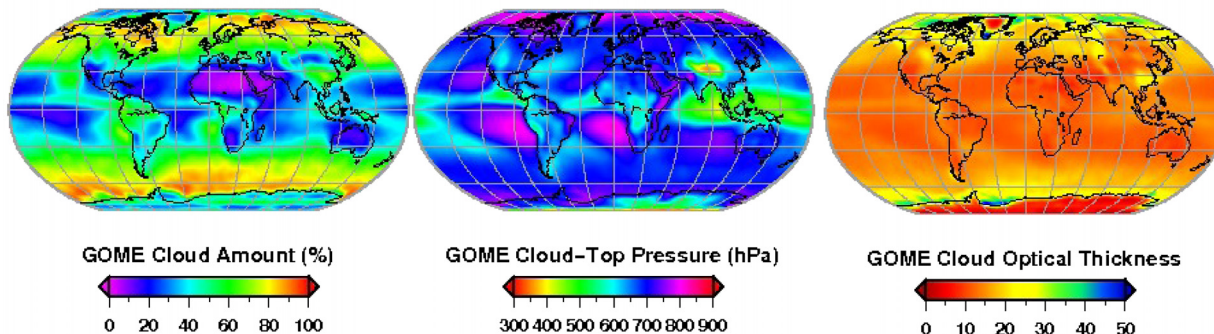


Fig. 2-9: Cloud parameters as derived from GOME, here averaged over the period 1996-2003. These parameters are contained in the level 1 product.

References

Coldewey-Egbers, M., S. Slijkhuis, B. Aberle, and D. Loyola: Long-term analysis of GOME in-flight calibration parameters and instrument degradation, *Applied Optics*, 47(28), 4749-4761, 2008

Loyola, D., W. Balzer, B. Aberle, M. Bittner, K. Kretschel, H. Muehle, T. Ruppert, C. Schmid, S. Slijkhuis, R. Spurr, W. Thomas, T. Wieland, and M. Wolfmueller: Ground Segment for ERS-2/GOME Sensor at the German D-PAF, 3rd ERS Scientific Symposium, Florence, Italy, ESA SP-414, 591, 1997

Loyola, D., W. Thomas, Y. Livschitz, T. Ruppert, P. Albert, and R. Hollmann: Cloud properties derived from GOME/ERS-2 backscatter data for trace gas retrieval, *IEEE Transactions on Geoscience and Remote Sensing*, 45, 2747-2758, 2007

2.3 SCIAMACHY Level 0-1b Improvements

G. Lichtenberg, S. Slijkhuis, B. Aberle, D. Scherbakov, M. Gottwald

The SCIAMACHY quality working group (SQWG) was initiated in March 2007 to coordinate, harmonise and streamline the development of SCIAMACHY operational data processing. Members are IUP-IFE (University of Bremen) as the prime, DLR-IMF, BIRA and SRON. Additionally it cooperates with KNMI. The SQWG acts as the sole interface to the agencies ESA, DLR, NIVR and BIRA for the evolution of the data processors. After the successful first contract the funding agencies decided to renew the SQWG contract for further development of the operational processing.

Apart from the further evolution of the data processing, IMF-AP also provides expert support for the maintenance of the operational processors and the quality of the data products. The tasks include investigation and solution of product or processor anomalies, answering helpdesk requests and supporting ESA for the implementation of the operational processing chain.

The starting point for our activities in SCIAMACHY data processing is the transfer of the level 0 measurement data to calibrated radiances, i.e. the level 0-1 processing. It includes three facilities:

- SciCal: This facility was developed by IMF in order to provide calibration data such as dark correction, sun reference spectra. It extracts all necessary calibration data from Level 0 products

and writes them to Auxiliary Data Files (ADF) which are subsequently used to calibrate the spectra.

- Level 0-1 prototype: The processor converts spectra from binary units per detector pixel into intensity per wavelength. It is the basis for the implementation of the operational Level 0-1 processor done by industry and under constant development at IMF.
- SciaL1c: The SciaL1c tool is a command line tool that allows users to generate calibrated data from Level 1b (called Level 1c data). Each calibration step can be switched according to the users choice. SciaL1c can also list states in the product and export data to an ASCII file.

Level 0-1 prototype development

The prototype development continued throughout 2009. The main improvements, planned for the next version, are

- matrix stray light correction for channel 3-8
- improvement of dark correction, especially for channels 6-8
- improvement of the correction of effects of the detector electronics like memory effect and non-linearity
- improvement of the PMD scaling of co-added data.

All changes had been successfully implemented and were ready for verification in early 2010. In order to prepare the re-processing in 2010, all calibration data from 2002 to 2009 were newly processed with the prototype.

SciCal

The main focus of the past year for SciCal was the improvement of the detector monitoring in SciCal. Detector pixels are damaged due to proton impact, mostly in the SAA. Therefore, an in-flight monitoring of the detector performance is necessary. This is done by analysing calibration measurements and defining quality parameters for each channel. Pixels that do not meet the quality thresholds are placed in the so-called Dead and Bad Pixel Mask (DBPM) and are excluded from all retrievals. The DBPM was further optimised with respect to the retrieval of CO and other trace gases. We processed masks for the full mission for evaluating the quality of the algorithm. Fig. 2-10 displays some results for channel 5 (as an example for a UV-VIS channel) and the SWIR channels 6 and 8. The fraction of pixels that are flagged as 'bad' is steadily increasing for the SWIR channels, while the number in the UV-VIS channels remains constant. This is due to the different detector material in the channels. In the UV-VIS channels pixels are usually only flagged at the edges of the channel, where 10 pixels were blinded to monitor the detector electronics, and during decontaminations. Between 2002 and 2009 eight decontaminations were performed. During decontaminations all detectors are heated, but measurements are still executed. However, the higher temperature leads to a very low signal-to-noise ratio, which is used as one quality criterion in the DBPM calculation.

The top right figure below shows the number of times a pixel was flagged as bad in channel 5. As expected, outside the edges of the channel the number never exceeds the number of decontaminations, i.e. the channel behaves normally under nominal conditions. The same is true for the other UV-VIS channels which are all made of silicon. For the SWIR channels the situation is different. Here the light detecting layer ($\text{In}_x\text{Ga}_{(1-x)}\text{As}$) was grown on an InP substrate. The Indium fraction x in the SWIR channels was varied to adjust the quantum efficiency for the desired spectral bands. The lattice constant of the $\text{In}_x\text{Ga}_{(1-x)}\text{As}$ changes with the fraction of Indium, leading to a higher susceptibility to radiation damage with higher wavelength. This is clearly visible in the bottom left figure: channel 6 is divided in two parts with different material and the doping in the material for pixel numbers larger than 794, the so-called *channel 6+*, leads to a higher number of bad pixels.

The analysis of a weekly mask for the SWIR channels in the time range from 2002-2009 shows that some pixels are flagged for the entire time range (all 352 weeks). These pixels were probably damaged during the production process or during the first months in orbit in the commissioning phase. However, since the mask has only two quality levels ('good' = use, 'bad' = do not use), the number of unusable pixels is perhaps overestimated. A new algorithm is under development which evaluates each pixel with respect to its usefulness for a given retrieval. Once this algorithm is implemented we hope to have more pixels again available for scientific retrievals.

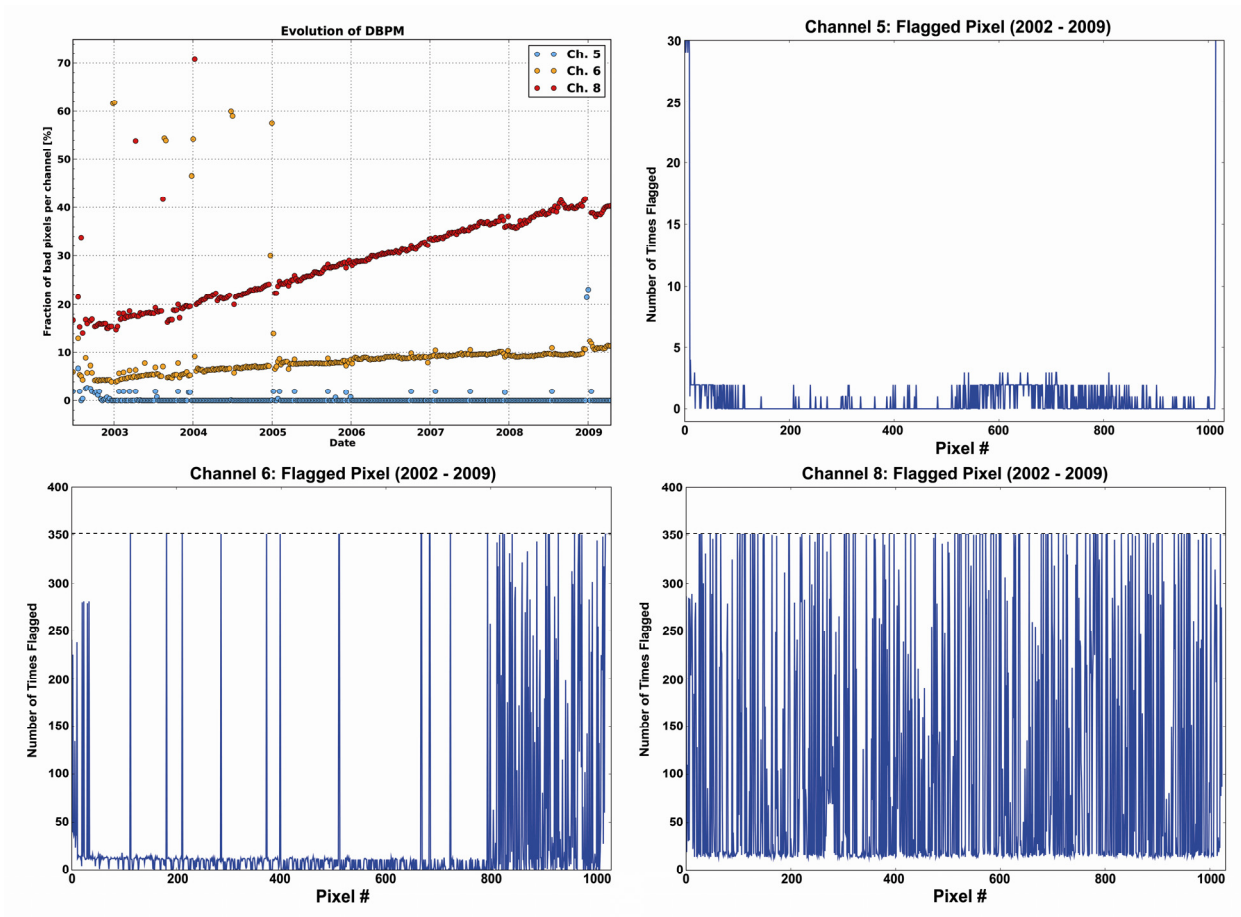


Fig. 2-10: DBPM evolution (weekly masks) for three channels 5, 6 and 8. Clockwise from topleft: Fraction of pixels flagged as bad and number of times a pixel was flagged from 2002 to 2009 for channels 5, 8 and 6. For details see text.

2.4 SCIAMACHY Operations Support

M. Gottwald, E. Krieg (TwIG), K. Reissig (IBR), J. How (TwIG)

One of the criteria indicating a flawless functioning of SCIAMACHY is the low visibility of the SCIAMACHY Operations Support Team (SOST), formed by personnel from IMF-AP and IUP-IFE (University of Bremen). This was also the case in 2009 where we continued our close collaborations with the Quality Working Group (SQWG) and ESA (flight operations at ESOC, post launch support at ESTEC and payload data segment at ESRIN).

The annual statistics indicate that the overall instrument availability remained at a very high level (fig. 2-11), even though the excellent figures of 2008 were not fully met. In 175 (2008: 84) out of 5224 orbits SCIAMACHY had been transferred to a mode lower than MEASUREMENT TIMELINE. Of these unavailabilities 117 orbits can be attributed to an instrument anomaly while the transfer to STANDBY in 15 orbits was a planned post-decontamination activity. For the remaining fraction data from 15 orbits were lost due to an anomaly of the on-board High Speed Multiplexer (HSM) while another 28 orbits saw SCIAMACHY in IDLE mode during planned out-of-plane orbit control manoeuvres (OCM). The instrument related anomalies can be attributed to Single Event Upsets (SEU), i.e. high energy particles impinging onto instrument electronic components and – for the first time since February 2006 the well-known CCA MCMD check error. Thus in total measurements were executed in about 97% of all possible orbits.

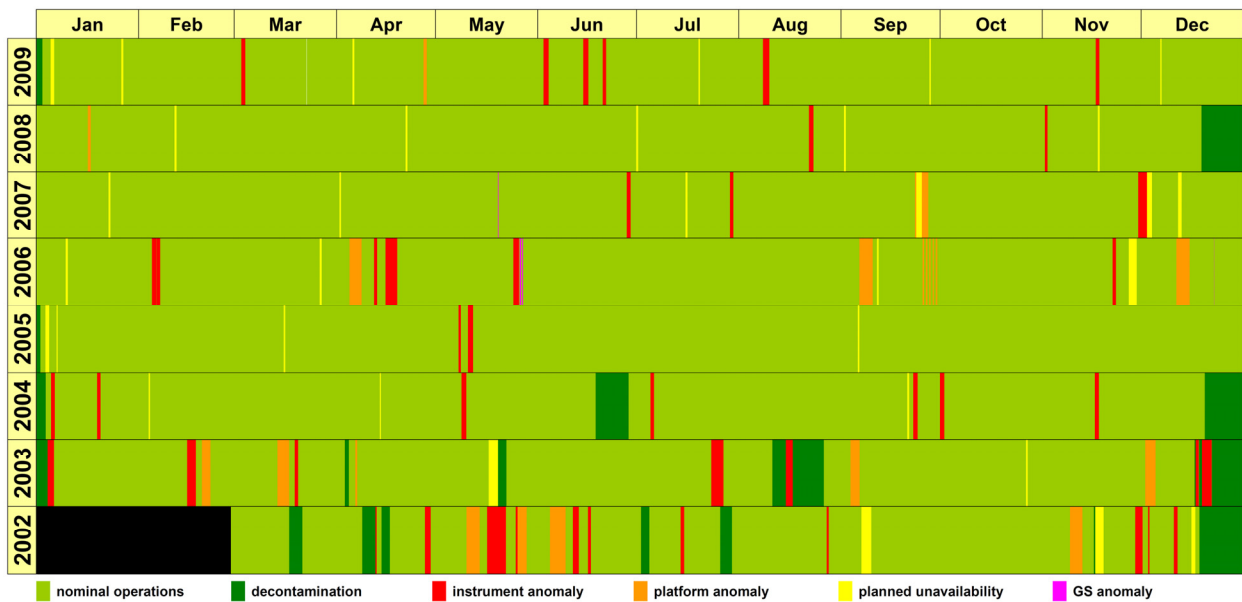


Fig. 2-11: Instrument availability since launch

Even on a monthly basis the availability did not drop below 95% (fig. 2-12) except for June when a triple of SEU induced anomalies occurred.

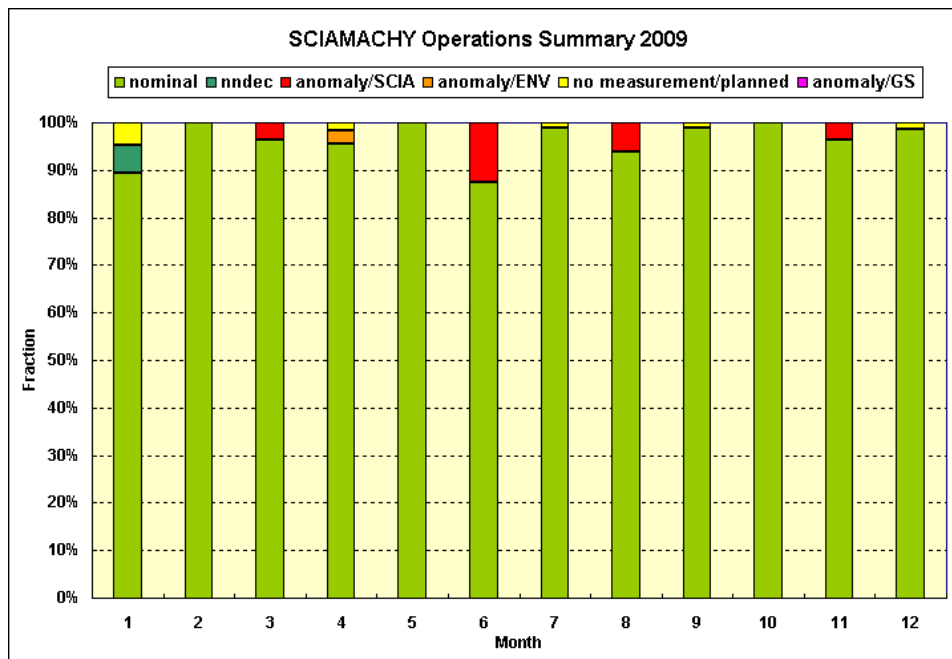


Abb. 2-12: Availability in 2009 on a monthly basis

Operation Change Requests

The reporting period required implementation of only 3 Operation Change Requests (OCR), transferring SCIAMACHY's routine final flight status into a temporary non-nominal configuration. Two of the OCRs were in support of specific measurement campaigns: in June/July the CEOAS/GEOMON campaign in Cabauw to better characterize the quality of tropospheric NO₂ and in October phytoplankton studies in the Pacific Ocean. The third OCR originated in 2008 but its execution had to await 2009. The OCR's subject was observing the planet Venus for calibration purposes. In this context very valuable scientific information was successfully gained on two occasions in March and June. Details of the Venus observations are described in two separate chapters 4.4 and 4.5.

Routine Operations

The routine operation tasks were executed as required and planned. This applies measurement planning, on-board configuration and long-term monitoring. Particular attention required the scanner monitoring (see below) and studies of the Line-of-Sight (LoS) pointing knowledge, particularly in limb and occultation viewing configuration (see below).

SCIAMACHY operations information was made publicly available via the SOST webpages (<http://atmos.af.op.dlr.de/projects/scops/>), as usual.

Scanner Monitoring

Scanner monitoring was based both on analyzing a 4 orbit sequence of Non-Nominal Telemetry formats for state 65 execution, commanded and acquired in June and studying specified scanner current telemetry HK parameters during regular execution of state 65. The NNT readings resulted in ASM/ESM scanner readouts every second thus enabling derivation of current profiles with improved time resolution for both scanners (for details see annual report of 2008). Analysis of the recorded 2009 NNT readings indicated identical current behaviour. Levels with almost constant current values did not change between 2008 and 2009. Only during the high acceleration part at the end of the measurement phase of the state execution slightly higher ESM_MEAN values, by about 2mA, as compared to 2008 could be derived. However, even if this increase would persist thus indicating a degradation of the ESM, it would be much too small for endangering scanner operations in the mission extension until the end of 2013.

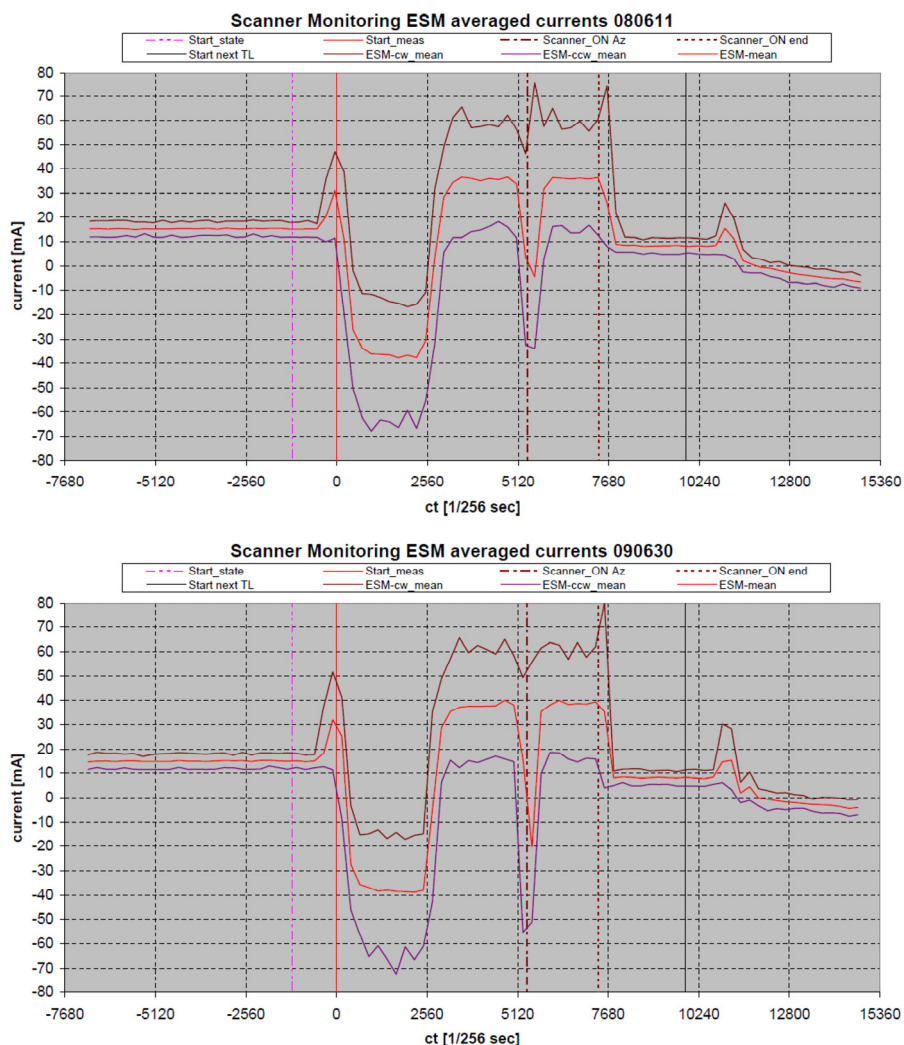


Abb. 2-13: ESM scanner currents (CW, CCW and MEAN), averaged over 4 orbits with NNT in 2008 (top) and 2009 (bottom). In both years the profiles are identical. Note that the different shapes of the spikes can be attributed to statistical effects.

The scanner behaviour since the early mission phase can be inferred from the ASM/ESM scanner currents obtained during each state 65 execution. As explained in the 2008 annual report, despite the coarse time resolution of 1/16 Hz, the state design causes a distinct current pattern. Changes would point towards a changing scanner performance. When analyzing all current telemetry parameters from 2002 onwards the patterns of fig. 2-14 were obtained. Around the turn of 2007/2008 (orbit 30000) the ESM readings began to increase. This triggered a detailed study by Astrium for ruling out a significantly degrading ESM scanner. Meanwhile the increase has stopped however and the current readings decreased again. Although the cause for this behaviour is not understood no countermeasures are considered necessary. Close scanner monitoring continues throughout the mission lifetime.

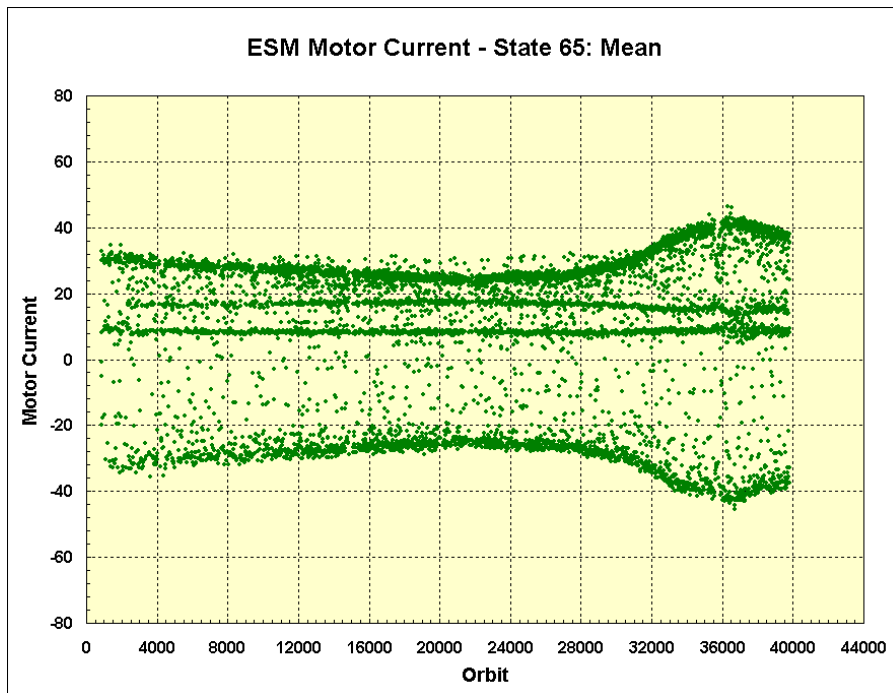


Fig. 2-14: Mean ESM scanner current from 2002 to October 2009

Line-of-Sight Pointing Knowledge

The line-of-sight pointing knowledge is one of the key parameters defining the quality of SCIAMACHY’s measurement data. Particularly for observation geometries with long light paths, i.e. limb and sun or moon occultations, a high LoS pointing knowledge accuracy ensures assigning correct tangent altitudes to retrieved atmospheric parameters.

In the annual report for the year 2007 we had described our approach to quantify the extra misalignment of SCIAMACHY’s LoS. Applying the corresponding pitch, roll and yaw mispointing angles in geolocation retrievals with ENVISAT’s Customer Furnished Items (CFI) significantly reduced the observed limb tangent height offsets from more than 1000 m to almost zero with an uncertainty of about 200 m. SOST has continued in 2008 the regular monitoring of SCIAMACHY’s pointing status by analyzing the ASM/ESM scanner behaviour at the time of Sun Follower activations. These data clearly show a seasonal variation in the order of 0.002-0.003°. However no explanation has been found yet. This is also true for a trend in the pointing knowledge claimed by our colleagues at IUP-IFE (University of Bremen) which seems to exist when comparing results from the scientific TRUE approach with limb geolocations from scanner readings. Both effects are at the accuracy limits of the pointing knowledge. Since several components – on-ground planning, platform attitude, scanner control – contribute to the final LoS orientation it requires very detailed investigations to determine the origin of these effects and compensate for it. Together with IUP-IFE and ESA we have started analyses of various LoS related datasets from ENVISAT measurement data and CFI simulations hoping to proceed further on this matter.

Consolidated Level 0 Master Archive

In 2009 SOST continued to maintain its master archive of consolidated level 0 (cL0) data in the Data Information Management System (DIMS) environment of the German Remote Sensing Data Center (DFD) at DLR. This archive serves as a reference for the cL0 repository used in reprocessing campaigns and supports SCIAMACHY product debugging in ENVISAT's Payload Data Segment (PDS). Details of the master archive generation can be found in the 2007 annual report. In brief consolidated level 0 data are regularly transferred to DIMS once they passed a sequence of checking routines. These verify the integrity of specific cL0 product properties.

By the end of 2009 more than 39000 cL0 products have been quality checked and transferred to DIMS. This includes orbits with incomplete consolidation provided they do not exhibit any other anomalies. The accumulated amount of useful measurement data in such orbits has been found to be equivalent to a measurement duration of about 50-60 full orbits. Further activities have been initiated to also derive the amount of useful data in orbits where the quality checks on the associated cL0 products have exhibited different anomalies (e.g. Reed Solomon, sync bit errors). Once this has occurred such cL0 products will also be transferred to DIMS.

The statistics for the years 2002-2009 is displayed in fig. 2-15. Note that for 2008 and 2009 the results are only preliminary since the second re-consolidation at ESA has not yet been performed. For the years 2002-2007 all verification steps, except the further handling of orbits with Reed Solomon and sync bit anomalies as described above, have been executed leading to cL0 availabilities as high as 97%. The detailed cL0 availability on single orbit level is given at the SOST website (<http://atmos.caf.dlr.de/projects/scops/>).

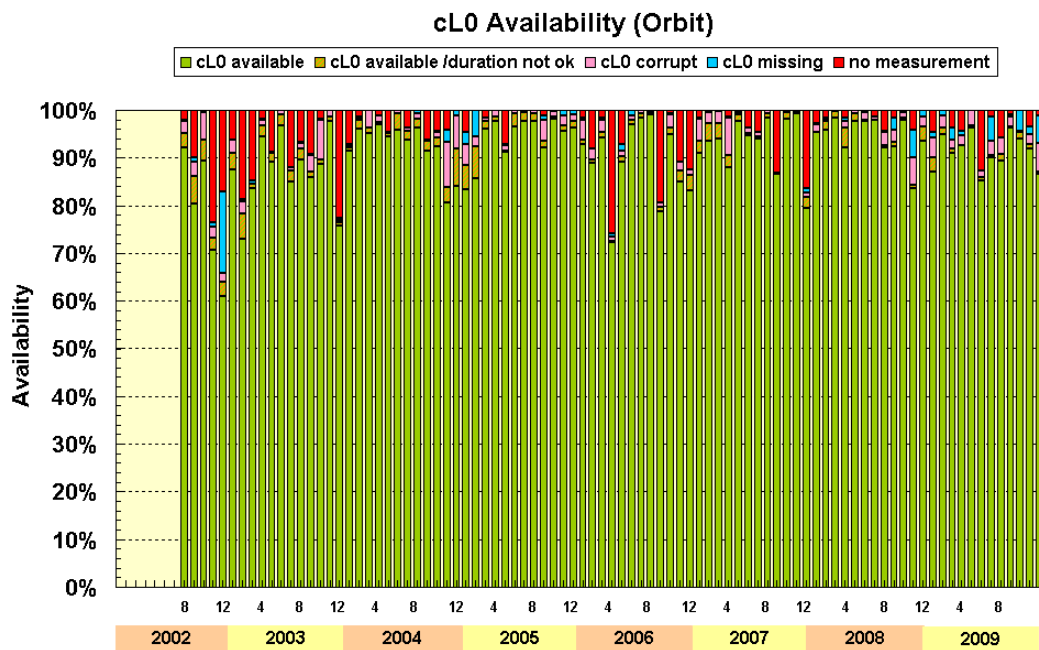


Fig. 2-15: cL0 statistics for the years 2002-2007 (final) and 2008-2009 (preliminary).

2.5 SCIAMACHY Configuration in the Mission Extension Phase

M. Gottwald, E. Krieg (TwIG)

In 2009 the preparations for the ENVISAT mission extension until the end of 2013 entered the phase where detailed implementation activities started. Since the extension concept requires lowering of the platform altitude with subsequent abandoning of fuel consuming inclination manoeuvres all instruments, including SCIAMACHY, have to adapt their Line-of-Sight (LoS) control accordingly. The tentative date for the orbit altitude manoeuvre is presently October 25th, 2010.

Orbit Analysis

In late 2008 ESA had delivered the updated operational ENVISAT CFIs (Customer Furnished Items) permitting to propagate the modified orbit (fig. 2-16). This CFI version 5.7 was used by SOST for a detailed orbit analysis simulating SCIAMACHY operations until the end of 2013. It includes functionalities describing the modified ENVISAT orbit such as

- new repeat cycle and cycle length of 30 days / 431 orbits
- drifting inclination starting at the current inclination of 98.549°
- drifting MLST starting at the current MLST of 22:00

Orbit propagation was performed for the time period 1st January 2010 to 25th October 2010 assuming a nominal ENVISAT orbit (35 days repeat cycle) and from 25th October 2010 to 31st December 2013 using the modified orbit specified above. When deriving the LoS specifying parameters, e.g. azimuth and elevation, it was assumed that the platform three axis attitude knowledge (pitch, roll, yaw) does not degrade in the mission extension phase. In addition ENVISAT will continue to operate in Stellar Yaw Steering mode (SYSM) using the nominal model with the current AOCS parameters.

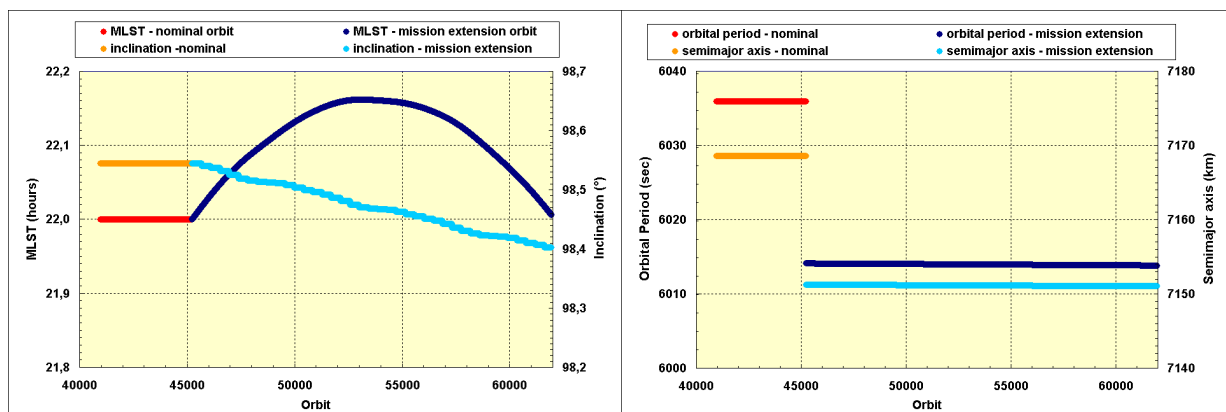


Fig. 2-16: MLST / inclination (left) and orbital period / semi-major axis (right) at ANX for the ENVISAT orbit between beginning 2010 and end 2013.

SCIAMACHY's in-orbit measurement operations are completely driven by the definition of the 70 on-board states and 63 timelines. Many of the parameters describing both states and timelines are reflecting the LoS orientation or sun/moon related event occurrences, e.g. sunrise, eclipse start, moonrise or subsolar phase, along the orbit. These refer to either time intervals between such events or azimuth/elevation angles at certain conditions. In order to specify required changes to the current state and timeline final flight configurations we simulated the SCIAMACHY LoS for the full period of the mission extension together with the period in 2010 when ENVISAT still occupies the nominal orbit. Fig. 2-17 presents two examples for the evolution of time intervals from 2010 to 2013 while fig. 2-18 illustrates two examples how azimuth and elevation evolves. In each figure the curve in red corresponds to the nominal orbit while the curve in blue represents the results for the mission extension with the modified orbit.

Our orbit analysis showed that for all time intervals relevant in SCIAMACHY operations the orbit modification causes only very moderate changes. These are well below the margins used in the definition of the timelines for the current nominal operations phase. Therefore no timeline changes are required for the mission extension phase as long as durations of orbital intervals (sun or moon related) are considered.

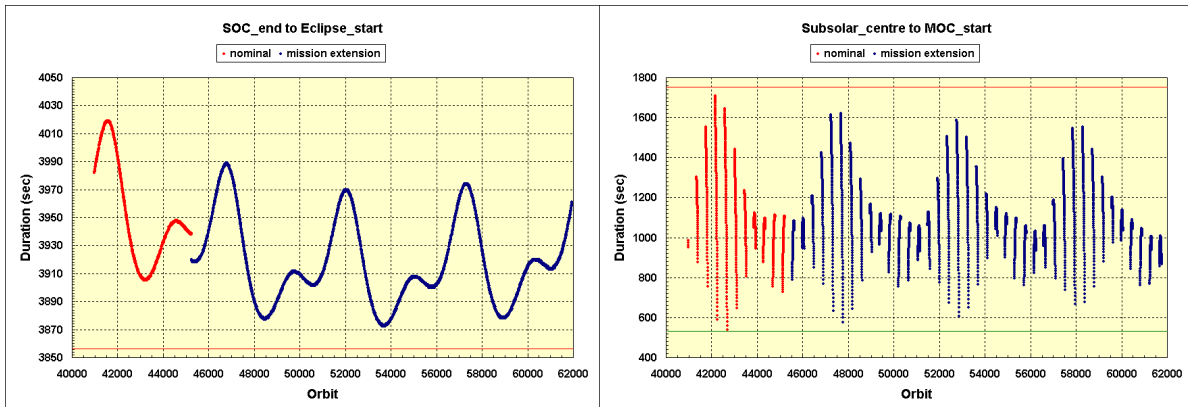


Fig. 2-17 Left: Duration of the time interval from the end of the SO&C window to the start of the eclipse phase. The horizontal red line indicates the presently defined timeline length for this period. Right: Duration of the time interval from the centre of the subsolar window to the start of the MO&C window. The horizontal red line indicates the presently defined maximum, the green line the minimum timeline length for this period.

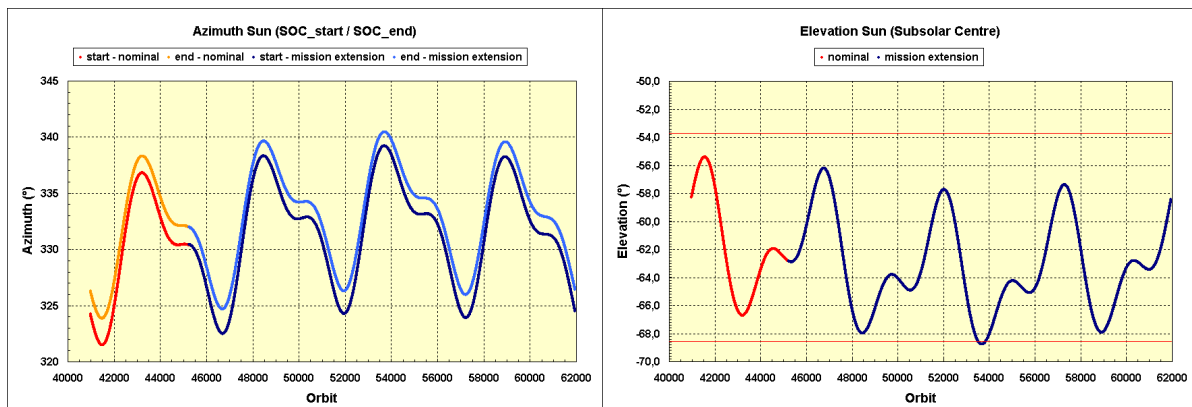


Fig. 2-18 Left: Azimuth of the Sun at the start and end of the SO&C window. Right: Elevation of the Sun in the subsolar window. The two red horizontal lines show the elevation limits of the subsolar window.

While the duration of sun/moon related orbital segments impacts mainly the definition of timeline durations, the angular orientation of the LoS is relevant for determining the impact of the orbit change on scanner control. Only certain azimuth/elevation angles and/or rates in the Basic Scan Profile table will be affected. Thus no other measurement parameter table needs updating as long as the state measurement definitions remain stable.

Limb/Nadir Matching

One of the unique features of SCIAMACHY operations is the matching of the geolocation of limb states with associated nadir states. Whether the matching of limb and nadir states is affected by the orbit modification has an across-track and an along-track aspect. The across-track issue is dealt with via the on-board s/w maintenance investigations by EADS-Astrium (yaw steering correction table). To ensure the along-track component of the limb/nadir matching it is necessary to verify how the elapsed time between the initial observation in limb mode of a certain volume of air and the observation of the same volume at the subsatellite point in nadir mode changes in an orbit with smaller semi-major axis. Thus our orbit analysis simulated one day of nominal measurements in the orbit with reduced altitude. As expected, because of the reduced length of SCIAMACHY's limb LoS, the limb ground pixel overlapped earlier with the corresponding nadir pixel. Re-establishing the performance of the current limb/nadir matching required shortening each limb state by the final horizontal scan thus achieving a maximum limb altitude of 90 km only (fig. 2-19). Specifying a limb state with less horizontal scans necessitates adaption of the State Duration table and of the Scanner State tables. Shortening each limb state even by only a small amount also alters the duration of the corresponding timelines. Thus these have to be modified as well. In essence it requires the generation of a new timeline set for the mission extension phase.

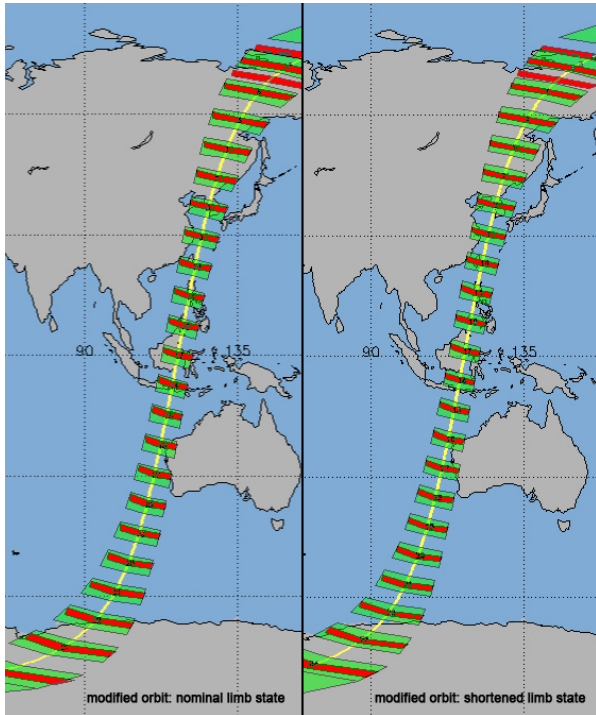


Fig. 2-19: Limb/nadir matching in the modified orbit with nominal limb state (left) and with shortened limb state (right) on the dayside of the orbit. The limb ground pixel (red) is defined by the tangent point while the nadir ground pixel (green) refers to the nadir start/stop times.

In summary our orbit analysis has shown that continuing SCIAMACHY operations in a lower ENVISAT orbit requires update of the Basic Scan Profile, State Duration and Scanner State tables. Additionally a new Timeline Set has to be generated. These changes will be implemented using the nominal operational interfaces. Since the date and time when the modified orbit becomes operational is part of the parameter file, the actual tables for upload will be generated once both are known. Our results, together with the modifications derived by Astrium for engineering parameters and potentially on-board s/w, e.g. yaw steering correction table, provide ESA with all information required to continue successful SCIAMACHY operations in the mission extension phase.

2.6 CEOS Workshop on Sea Surface Temperature Sounding

C.H. Köhler, P. Gege (IMF-EV), W. Vreeling (IMF-EV)

In May 2009 the Working Group on Calibration and Validation (WGCV) of the Committee for Earth Observation Satellites (CEOS) conducted a workshop in cooperation with the Rosenstiel School of Marine and Atmospheric Science (RSMAS) at the University of Miami. The workshop was hosted by Dr. N. Fox of the UK's National Physical Laboratory, chair of the WGCV Infrared and Visible Optical Sensor Subgroup (IVOS), and Prof. Dr. P. Minnett, Head of the RSMAS Division of Meteorology and Physical Oceanography (MPO).

The workshop aimed at a cross-comparison of several ground based instruments applied in sea surface temperature (SST) sounding for satellite calibration and validation. It included laboratory measurements as well as field measurements, both conducted at the RSMAS site in Miami. The laboratory measurements used mainly two high-accuracy black bodies of RSMAS and the United States National Institute of Standards and Technology (NIST). These black bodies were observed at different temperatures by all instruments participating in the workshop, in order to determine the radiometric accuracy of each instrument under laboratory conditions. The quality of the black bodies was ensured by a high-precision radiometer provided and operated by a team from NIST. In addition to the laboratory measurements all instruments were set up along a pier enabling simultaneous measurements of the SST under field conditions. Responsible for the scientific coordination of IMF workshop contributions was P. Gege (IMF-EV), who also initiated the participation in the workshop and who is

responsible for the scientific evaluation of the data. Our measurements were done with the D&P Model 102 FTIR which was operated by C.H. Köhler (IMF-AP) and W. Vreeling (IMF-EV). This is the same instrument used for the SAMUM2 campaign in January 2008 (see IMF annual report of 2008).

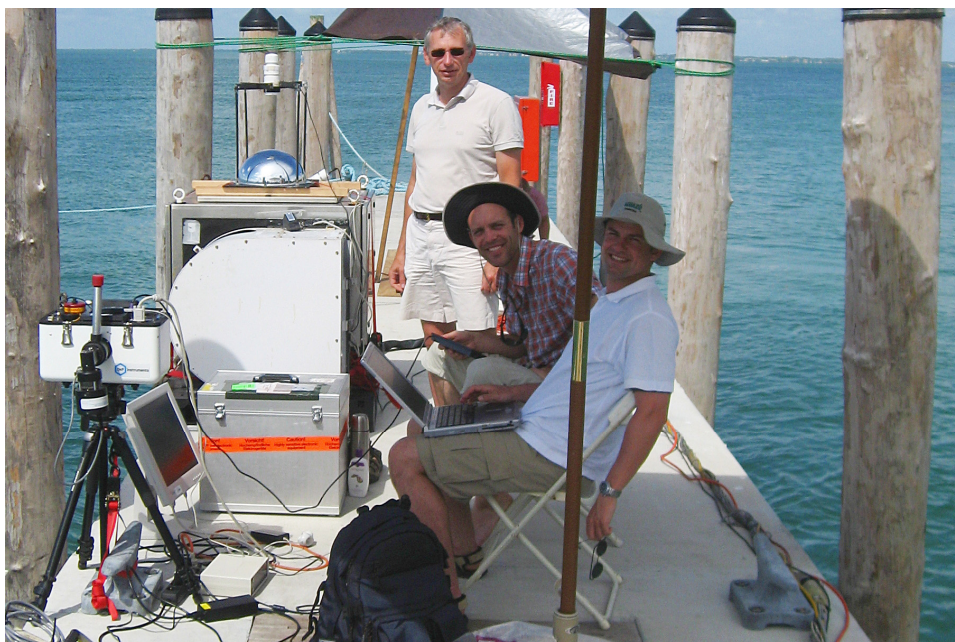


Fig. 2-20: The instruments D&P (left) and MAERI (background) during SST measurements at the RSMAS pier. From left to right: P.Gege, W. Vreeling and C.H. Köhler.

Although IMF-AP is not involved in the scientific work connected to this campaign, an interesting opportunity arose providing valuable information within the SAMUM-2 framework. Together with colleagues from IMF-EV we participated in the SAMUM-2 field campaign on the island of Cape Verde in 2008. Then the same D&P FTIR used for the CEOS workshop were operated. Since the SAMUM-2 campaign was the first campaign conducted with the Model 102, error estimation and quality assurance remained still open issues, especially for zenith view thermal emission measurements. During the CEOS workshop parallel measurements with a MAERI (Marine Atmospheric Emitted Radiance Interferometer) instrument, a Fourier Transform Infrared Spectrometer owned by RSMAS and developed and manufactured by the Space Science and Engineering Centre of the University of Wisconsin, were performed. MAERI, designed to operate in a marine environment, is a modification of the AERI instrument which is an advanced version of the high spectral resolution interferometer sounder (HIS). The latter was designed and fabricated at the University of Wisconsin to investigate up-welling infrared radiances from an aircraft. MAERI is a fully automated ground-based passive infrared interferometer that measures down-welling atmospheric radiance from $\lambda = 3.3\text{-}18.2\ \mu\text{m}$ (wavenumber $550\text{-}3000\ \text{cm}^{-1}$) with a time resolution better than 10 min and a spectral resolution of less than one wavenumber. It is very well calibrated and characterized and has proven to deliver excellent results of down-welling atmospheric radiances and therefore poses a good choice for an instrument validation of the D&P Model 102 field FTIR. This is particularly interesting regarding the atmospheric measurements performed during the SAMUM-2 field campaign.

MAERI was set up on the same pier as the instruments participating in the CEOS comparison and operated in an automated continuous mode, while the D&P instrument was operated either on the pier or in the laboratory as required for the instrument comparison. Each MAERI cycle consists of two calibration measurements followed by three scene measurements at 0° , 55° and 125° (all angles relative to zenith). The D&P instrument was operated manually and set to the same viewing angles as MAERI for the comparison. Fig. 2-21 shows a comparison of a MAERI zenith measurement with a simultaneous Model 102 zenith measurement during clear sky conditions on 14th May 2009 at 3:20 p.m. (local). In order to enable a better comparison, the MAERI spectrum was sinc-convolved to the resolution of the Model 102 spectrum. In addition to the measurements a radiative transfer simulation for a midlatitude-summer atmosphere is displayed, with temperature, pressure and relative humidity profiles taken from a radiosonde ascent at Miami airport at 5:06 p.m. (local). The figure displays a good agreement of all

three spectra over almost the whole spectral domain. Only a slight deviation of the Model 102 spectrum from simulation and the MAERI measurement can be observed between 1000 and 1100 cm^{-1} . This is most probably due to non-linear behaviour of the built-in MCT detector of the D&P instrument. The instrument comparison of the Model 102 FTIR with MAERI will allow a good assessment of the data quality for measurements performed with the Model 102 and will be especially helpful in characterizing systematic errors due to detector non-linearity for the SAMUM 2 project.

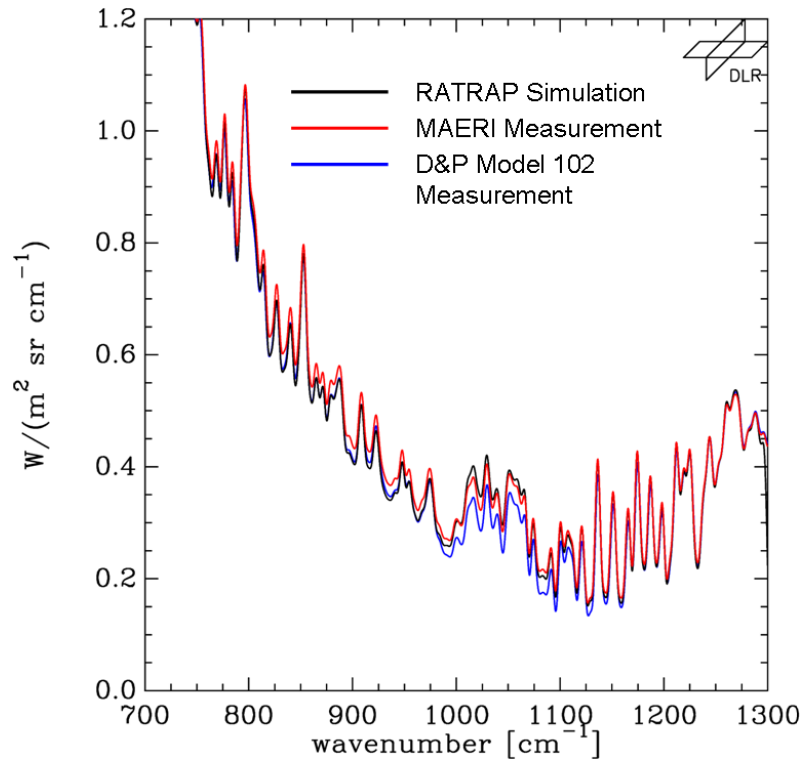


Fig. 2-21: Comparison of a Model 102 zenith measurement with a simultaneous MAERI measurement and a radiative transfer simulation for a midlatitude summer atmosphere under inclusion of a close-by radiosonde ascent.

3. Atmospheric Remote Sensing – Retrieval Methods

3.1 O3M-SAF Retrieval of Water Vapour Column Amounts from GOME-2

S. Slijkhuis, S. Emmadi (TUM), D. Loyola, T. Wagner (MPI for Chemistry, Mainz), K. Mies (MPI for Chemistry, Mainz)

Atmospheric water vapour (H₂O) is the most important natural (non-anthropogenic) greenhouse gas, which accounts for about 2/3 of the natural greenhouse effect. Despite this importance, its role in climate and its reaction to climate change are still difficult to assess. Many details of the hydrological cycle are poorly understood, e.g. the process of cloud formation, or the transport and release of latent heat contained in the water vapour. In contrast to other important greenhouse gases like CO₂ and Methane, water vapour has a much higher temporal and spatial variability. Global monitoring of H₂O by satellite is therefore a key to understanding its impact on climate.

Long time series of global satellite measurements of total column H₂O have traditionally been derived from microwave instruments. The series of SSM/I instruments and the microwave instruments on TOVS and ATOVS have been providing H₂O records since the late 1980's. The dependence of microwave retrievals on surface temperature limits reliable H₂O retrievals to ocean surfaces. In recent years, global H₂O satellite measurements over land have become available from near-infrared hyperspectral imagers such as MODIS on AQUA/TERRA, MERIS on ENVISAT, VISSR on GOES and SEVIRI on MSG, but their accuracy has to be established. High-precision H₂O measurements over land are available from radiosonde and GPS networks, but with restricted spatial coverage.

Several studies have shown the capability to retrieve total column H₂O from space-born spectrometers operating in the visible spectral region, in particular for the GOME family of instruments. The GOME/SCIAMACHY/GOME-2 series of instruments will cover a projected time-span of at least 20 years. This climatologically relevant time span, and the ability to retrieve H₂O over sea and over land, makes the GOME family of sensors interesting for climatology studies of water vapour.

The current GOME H₂O retrieval schemes have the advantage that they do not rely on external data - in contrast, the microwave data are usually calibrated on the radiosonde data, and GPS retrievals usually employ temperature input from Global Climate Models. While the GOME retrieval method may not allow the highest absolute accuracy, it does make the GOME H₂O dataset a truly independent one. On the downside, GOME measurements are hampered by clouds (like the near-infrared imagers); an H₂O climatology from GOME will therefore not be completely independent of cloud climatology.

Since 2007 the O3M-SAF (Satellite Application Facility on Ozone and Atmospheric Chemistry Monitoring) at DLR provides data products from the GOME-2 instrument on EUMETSAT's MetOp satellite, for total column amounts of Ozone and other atmospheric trace gases. In 2009, an algorithm for the retrieval of water vapour (fig. 3-1) was implemented and validated. In December 2009 the O3M-SAF review board approved the algorithm for operational data processing.

The first step has been to select a basis for the algorithm. Two scientific developments were considered:

- The AMC-DOAS method from University of Bremen (*Noël et al. 1999*). The algorithm uses the H₂O bands around 695 nm, in combination with the O₂-B band.
- A classical DOAS method from MPI Mainz / University of Heidelberg (*Wagner et al. 2006*). The algorithm uses the H₂O bands around 650 nm, in combination with the O₂-C band.

Data from these two algorithms were compared to each other, to data of the SSM/I F15 instrument, and to data of the global radiosonde network (latter work performed at FMI, Helsinki).

Inter-comparisons

A direct comparison of the Bremen algorithm to the Mainz algorithm was done for both, GOME data (using selected dates from 2002 and 2003) and GOME-2 data (fig. 3-2 left). This comparison showed a surprisingly narrow correlation, although with a systematic bias. The bias is similar for both the GOME instruments. The narrowness of the correlation indicates that the algorithms effectively use similar assumptions for the conversion from measured slant columns to vertical total column amounts. Only near twilight conditions a deviation from the general correlation is present. The GOME data were then

compared to data from SSM/I (available only over ice-free ocean). Fig. 3-2 (right) presents the data in 2D histogram form: the H_2O values from SSM/I (x-axis) are binned into 2 kg/m^2 (0.2 g/cm^2) wide bins, and the differences in H_2O values GOME – SSM/I (y-axis) are binned into 0.5 kg/m^2 (0.05 g/cm^2) wide bins; the number of points in each bin is colour-coded from grey-blue to red-brown.

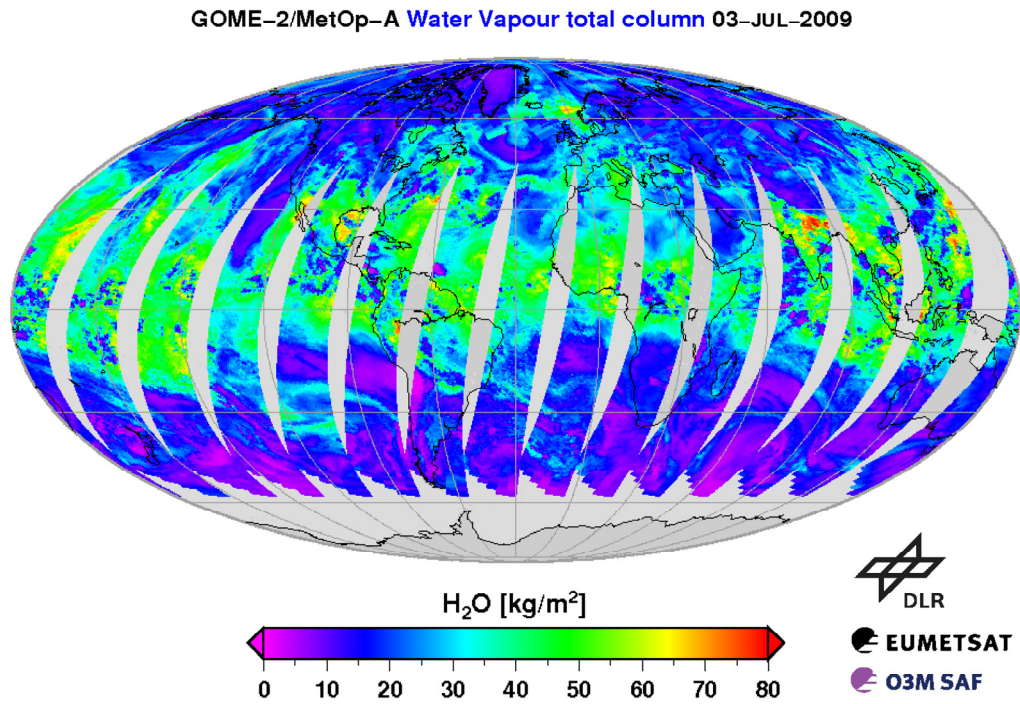


Fig.3-1: Water vapour total column, one day of GOME-2 measurements, not filtered for clouds

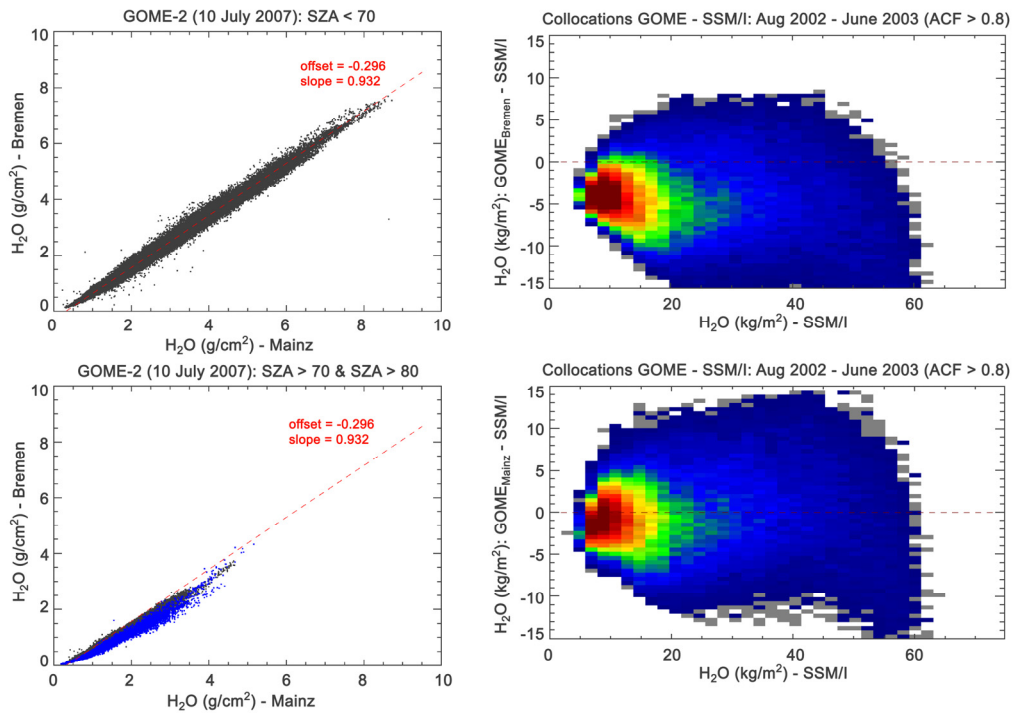


Fig. 3-2: Comparison of H_2O retrieval results. Left: Scatterplot of total H_2O (g/cm^2) from GOME-2, Bremen algorithm versus Mainz. The top panel is for data with solar zenith angle (SZA) below 70° , bottom panel is for $70^\circ < \text{SZA} < 80^\circ$ (gray) and $\text{SZA} > 80^\circ$ (blue, overplotted). Right: 2D-histograms of difference (GOME – SSM/I) versus SSM/I (kg/m^2), top: H_2O from Bremen, bottom: H_2O from Mainz.

We found that both algorithms show several more or less subtle differences against SSM/I and radiosonde data. On the whole, we find that the performance of the two algorithms, in comparison to external data, is balanced. On the basis of our comparisons there is no strong argument to prefer one algorithm over the other.

Implementation

The algorithm from Mainz was chosen for implementation, mainly because the algorithmic structure is much closer to the algorithms which are already present in the data processor (UPAS), for other trace gases. A 'visiting scientist' contract was established with scientists from the Mainz group, to perform further development of the algorithm and to assist in verification of the data processor results. Operational data release is foreseen for the beginning of 2010.

Review

Two years of GOME-2 water vapour, computed with UPAS, were validated with radiosondes by FMI with the results being reviewed in the Operational Readiness Review – Part 3 (ORR-B3) held in December 2009 at the DLR premises. This review was successful and the review board recommended to update the status of the O3M-SAF water vapour product to 'pre-operational'.

References

Loyola, D., Valks, P., Ruppert, T., Richter, A., Wagner, T., Thomas, W., van der A, R., Meisner, R.: The 1997 El Niño impact on clouds, water vapour, aerosols and reactive trace gases in the troposphere, as measured by the Global Ozone Monitoring Experiment, *Advances in Geosciences*, 6, 267-272, 2006

Noël, S., Buchwitz, M., Bovensmann, H., Hoogen, R., and Burrows, J. P.: Atmospheric Water Vapor Amounts Retrieved from GOME Satellite Data, *Geophys. Res. Lett.* 26, p.1841, 1999

Slijkhuis, S., Beirle, S., Kalakoski, N., Mies, K., Noël, S., Schulz, J., Wagner, T.: Comparison of H₂O retrievals from GOME and GOME-2, Proc. 2009 EUMETSAT Meteorological Satellite Conference, Bath, 2009, available under

http://www.eumetsat.int/Home/Main/AboutEUMETSAT/Publications/ConferenceandWorkshopProceedings/groups/cps/documents/document/pdf_conf_p55_s6_34_slijkhui_p.pdf

Wagner, T., Heland, J., Zöger, M., and Platt, U.: A fast H₂O total column density product from GOME – Validation with in-situ aircraft instruments. *Atmos. Chem. Phys.* 3, pp 651-663, 2006

3.2 GOME-2 Formaldehyde: A New Operational O3M-SAF Product

N. Hao, P. Valks, D. Loyola, W. Zimmer, S. Emmadi (TUM), M. Van Roozendaal (BIRA-IASB), I. De Smedt (BIRA-IASB)

Formaldehyde (HCHO) is one of the most abundant hydrocarbons in the atmosphere and is an important indicator of non-methane volatile organic compound (NMVOC) emissions and photochemical activity. HCHO is a primary emission product from biomass burning and fossil fuel combustion, but its principle source in atmosphere is the photochemical oxidation of methane and non-methane hydrocarbons. Satellite measurements of HCHO can be used to constrain NMVOC emissions in current state-of-the-art chemical transport models (*Abbot et al., 2003*).

The HCHO vertical column algorithm for GOME-2 has been developed in cooperation with BIRA-IASB (*De Smedt et al. 2008*). In the first step, the HCHO slant column density is retrieved with the Differential Optical Absorption Spectroscopy (DOAS) method using the 328.5-346 nm wavelength range. Secondly, the vertical column density is obtained by dividing the slant column by an appropriate air mass factor (AMF), calculated with the radiative transfer model LIDORT 3.3. An important aspect of the AMF calculation for tropospheric trace gases such as HCHO is the dependence of the AMF on the a priori vertical profile shape of the trace gas. For the GOME-2 algorithm, monthly averaged a priori HCHO profiles are obtained from the IMAGESv2 global chemistry transport model (*Stavrakou et al. 2009*), and

interpolated for each measurement location. As an example, the HCHO total column distribution for 2008 as measured by GOME-2 is shown in fig. 3-3. Clearly visible in this figure are the high HCHO emissions in the Tropics (Amazonia, Africa and Indonesia) as a result of biomass burning, the Eastern United States and South eastern Asia as a result of the oxidation of biogenic VOCs.

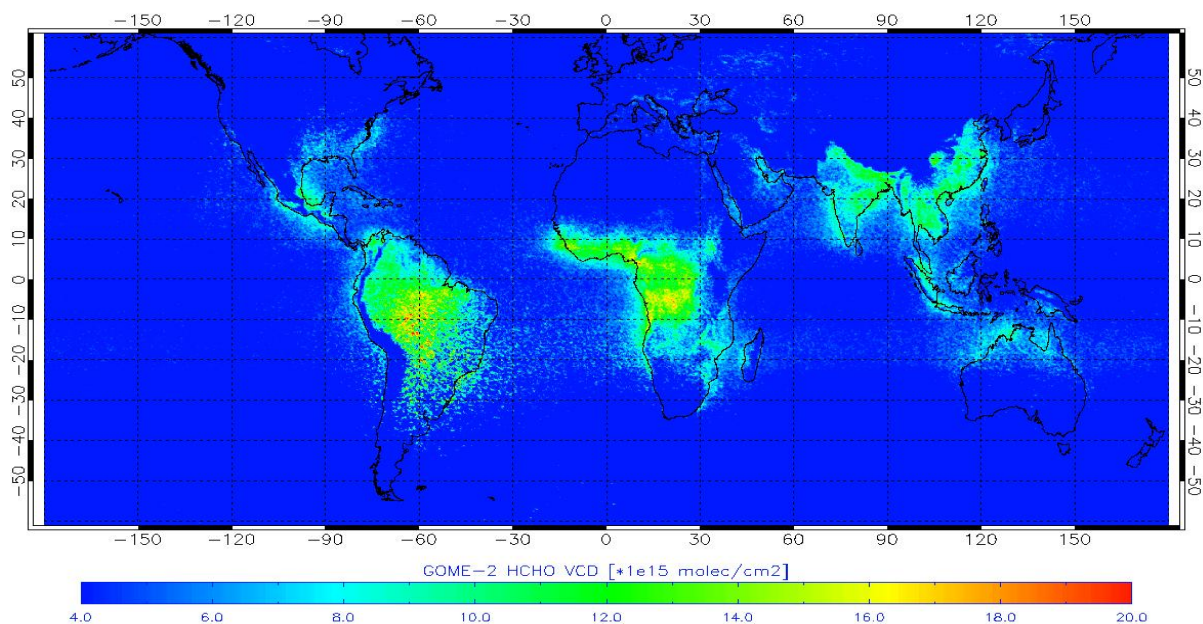


Fig. 3-3: Yearly averaged vertical HCHO columns for 2008, as measured with GOME-2.

A verification and initial validation of the GOME-2 HCHO columns has been carried out by BIRA-IASB and IMF-AP for the period January 2007 to August 2009. In order to validate the GOME-2 HCHO columns, comparisons have been performed with correlative data sets from other satellite instruments, such as GOME and SCIAMACHY, as well with ground-based measurements. Fig. 3-4 presents a comparison of monthly averaged SCIAMACHY and GOME-2 HCHO columns with ground-based Fourier Transform Infrared (FTIR) measurements at Reunion Island in the Indian Ocean. The seasonal variation of formaldehyde is well reproduced and we find no bias between the satellite and the FTIR measurements. Fig. 3-5 shows a comparison of GOME-2 HCHO columns with SCIAMACHY and ground-based MAX-DOAS measurements in Beijing. Here, the GOME-2 columns also display a good agreement with the SCIAMACHY and ground-based measurements. The correlation between GOME-2 columns and the MAX-DOAS observations is 0.7, and the regression line presents a slope of 26%.

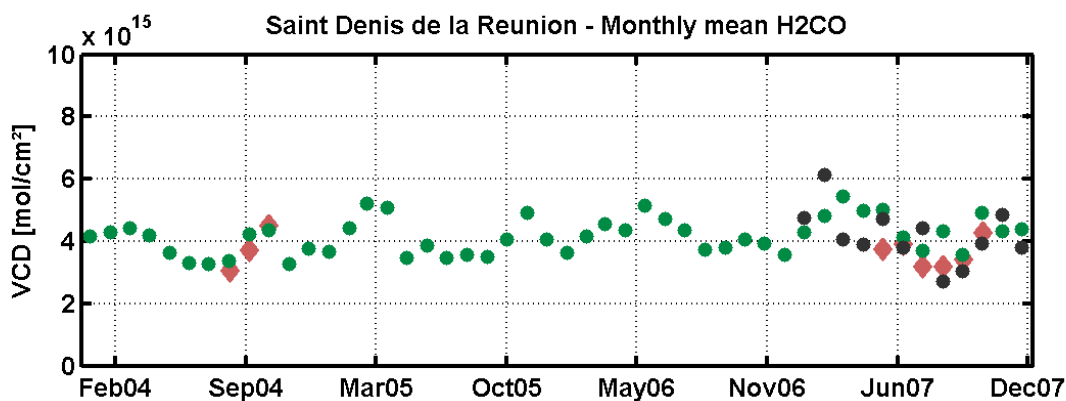


Fig. 3-4: Comparison between monthly average SCIAMACHY (green) and GOME-2 (black) HCHO columns, with FTIR measurements at Reunion Island (21S, 56E) (pink). Satellite measurements within a radius of 500 km around Reunion Island have been used.

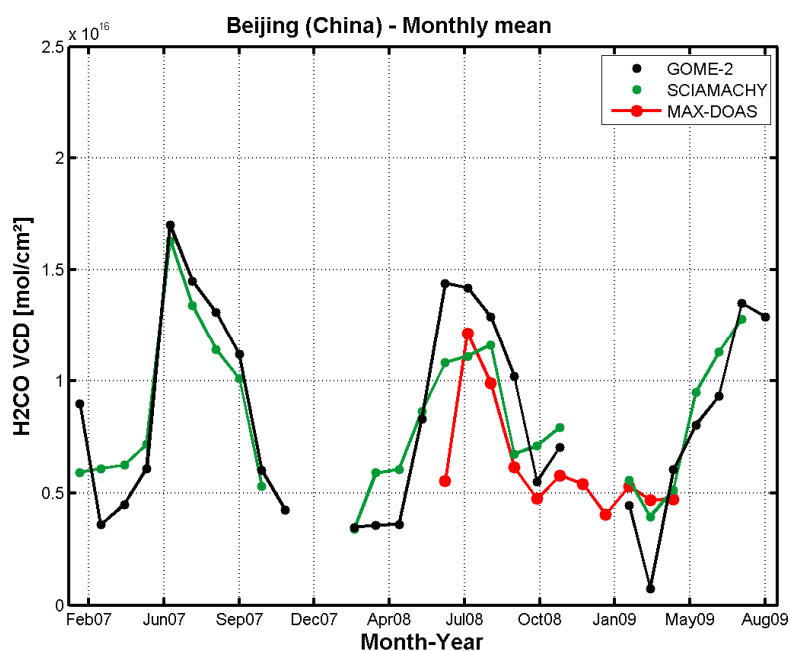


Fig. 3-5: Monthly averaged SCIAMACHY (green) and GOME-2 (black) HCHO columns compared with MAX-DOAS measurements in Beijing (40N, 116E) (red). For this comparison, satellite measurements within a radius of 200 km around Beijing and MAXDOAS data at the satellite overpass time have been used.

GOME-2 total column products of ozone and other minor trace gases (NO₂, BrO, SO₂ and HCHO) have been developed by IMF-AP in the framework of EUMETSAT's Satellite Application Facility on Ozone and Atmospheric Chemistry Monitoring (O3M-SAF). These trace gas column products are generated operationally by DLR using the GOME Data Processor (GDP) version 4.4. The new GOME-2 HCHO product was reviewed at the Operation Readiness Review – Part 3 (ORR-B3) in December 2009. The validation report from BIRA/IASB confirmed the high quality reached by the HCHO column product, fulfilling the O3M-SAF user requirements in terms of accuracy. Hence, the ORR-B3 review board recommended the new O3M-SAF HCHO product to be declared operational. The start of the Operational dissemination shall start in the beginning of 2010.

References

- Abbot, D.S., Palmer, P.I., Martin, R.V., Chance, K.V., Jacob, D. J., and Guenther, A.: Seasonal and interannual variability of North American isoprene emissions and interannual variability of North American isoprene emissions as determined by formaldehyde column measurements from space, *Geophys. Res. Lett.*, 30, 17, 1886, doi: 10.1029/2003GL017336, 2003
- De Smedt, I., Müller J.-F., Stavroukou T, van der A, R., Eskes, H. and Van Roozendael, M.: Twelve years of global observation of formaldehyde in the troposphere using GOME and SCIAMACHY sensors. *Atmos. Chem. Phys.*, 8 (16), 4947-4963, 2008
- Stavroukou, T., Müller, J.-F., De Smedt, I., Van Roozendael, M., van der Werf, G. R., Giglio, L., and Guenther, A.: Evaluating the performance of pyrogenic and biogenic emission inventories against one decade of space-based formaldehyde columns, *Atmos. Chem. Phys.*, 9, 20 1037–1060, 2009

3.3 SCIAMACHY Level 1b-2 Processing

G. Lichtenberg, A. Doicu, S. Gimeno García, S. Hrechanyy, K. Kretschel, M. Meringer, F. Schreier

In the previous year the SCIAMACHY Quality Working Group (SQWG) finished the development and verification of version 5 (V5) of the off-line processor. In June 2009 this processor was delivered to ESA and development of the next – further improved – version 6 was started. An overview of how the processor evolved from V3.01, which was operational in the end of 2009, to V5.01 is given in tables 3-1 and 3-2. It will become operational in February 2010 and will be validated in spring/summer 2010¹. Some of the products in version 5 are already in ‘maintenance mode’, i.e. no major algorithm change in the immediate future is foreseen except for bug fixes and minor corrections. However, compared to V3.01, V5 introduces seven new products bringing the total of operationally retrieved products to 13. The delivery of version 6 with three new products and some improvements is planned for the first half of 2010. More details about the roadmap, algorithm details and contributors can be found in (Bovensmann et al. 2009).

Product	V3.01 (2007-2010)	V 5.01 (from 2010)	Planned for V6
O3	improvements from validation	introduction of radiometric degradation correction	maintenance
NO2	improvements from validation	maintenance	maintenance
SO2	unavailable	VCD with Background correction	maintenance
OCIO	unavailable	SCD	maintenance
BrO	unavailable	VCD	maintenance
H2O	unavailable	VCD	maintenance
CO	unavailable	VCD	maintenance
CH4	unavailable	unavailable	VCD
CHOCHO	unavailable	unavailable	SCD
HCHO	unavailable	unavailable	VCD
AAI	introduction of algorithm using DAK	maintenance	use O3 from same orbit for RTM
Cloud Parameters	improvements from validation	new reflectance database	add snow/ice separation

Table 3-1: Nadir products in the Level 1b-2 offline processor (SCD = slant column density, VCD = vertical column density)

Product	V3.01 (2007 – 2010)	V5.01 (from 2010)	Planned for V6
O3	stable	improve retrieval parameters after validation	add altitudes 40 – 65 km
NO2	stable	improve retrieval parameters after validation	maintenance
BrO	unavailable	profile	maintenance
Cloud Parameters	unavailable	introduction of water cloud and PSC detection	addition of NLC detection

Table 3-2: Limb Products in Level 1b-2 offline processor (for details see text)

¹ Version 4 was delivered to ESA, but never operational due to delays in the ground segment switch to Linux.

For the new version of the processor, we proposed a changed verification scheme (see fig. 3-6). In the past, all algorithm modifications were bound to a fixed release date and done in a single, intensive implementation campaign of 2 months with intermediate testing on a few orbits. The verification with the full data set of 180 orbits only occurred at the end of the implementation. Due to the complexity of the offline processor some changes led to unforeseen side effects which required additional phases of debugging and altering the code. The new approach includes the following steps

- Implementing individual algorithms (or groups of algorithms) as they become available. Level 2 data are generated from Level 1b data from the latest verified Level 0-1 processor. The version of Level 1b is then fixed until the delivery of the Level 1b-2 processor.
- Verifying the algorithm with the full set of 180 orbits
- After successful verification of the individual algorithm do a dedicated 'regression test' of all products, i.e. also those that were not changed, to discover side effects

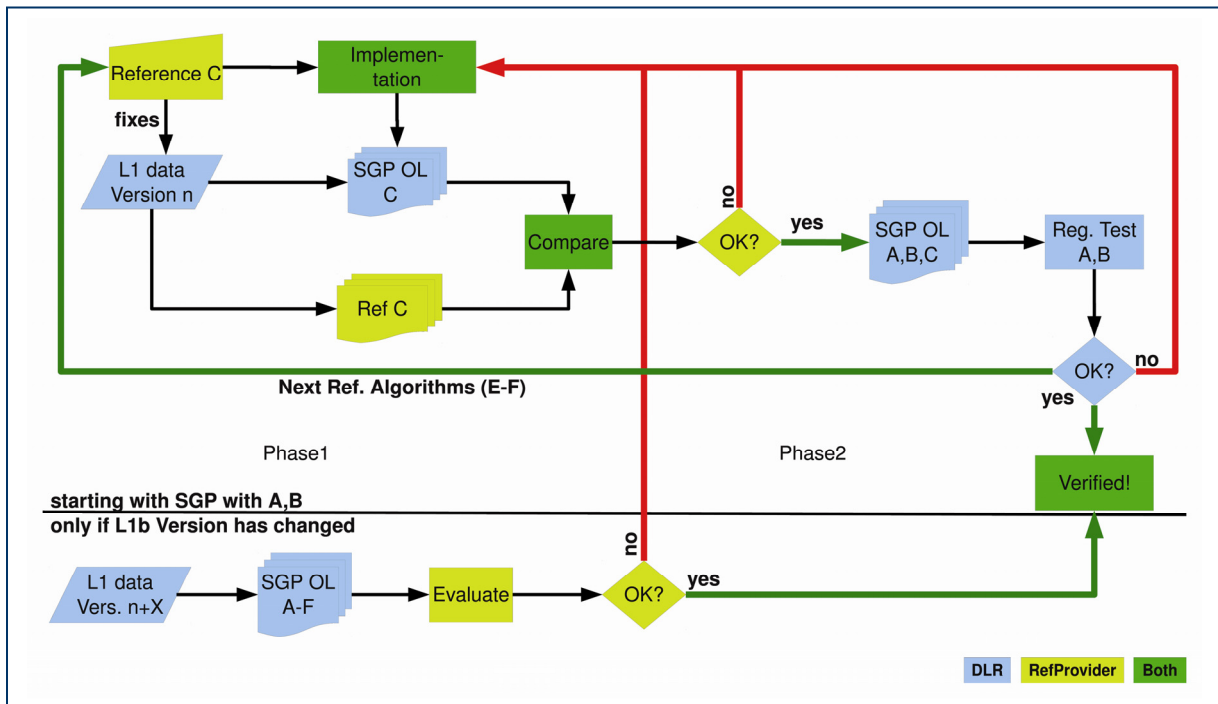


Fig. 3-6: New verification scheme for the offline Level 2 processor.

The above approach will generate intermediate versions of the processor which are fully verified, i.e. the release date is no longer fixed and the development work is more evenly distributed over the year. Whenever the processor has accumulated enough changes to justify a full mission reprocessing, it can be released. In the case that the level 1b version has changed since the start of the verification, a final verification for all products using the latest level 1 version will be done. This has the added benefit that impact of level 1 changes on the level 2 product can be separated from changes in the product caused by the update of the level 2 processor. The additional work caused by the additionally needed regression and level 1b tests can be easily automated and will thus not cause longer release cycles.

References

Bovensmann, H., K.-U. Eichmann, S. Noel, A. Richter, M. Buchwitz, C. von Savigny, A. Rozanov, G. Lichtenberg, A. Doicu, F. Schreier, S. Hrechanyy, K. Kretschel, M. Meringer, M. Hess, M. Gottwald, A. Friker, S. Gimeno García, J.A.E. van Gijssel, L.G. Tilstra, R. Snel, C. Lerot, M. Van Roozendael, A. Dehn, H. Förster, T. Fehr: Development of SCIAMACHY Operational ESA Level 2 Products towards Version 5 and Beyond. ESA Atmospheric Science Conference, ESA SP-676, Barcelona, 2009

SQWG: SCIAMACHY Level1b-2 data processing: Verification Report OL V 5.0, Technical Note, ENV-VPR-QWG-SCIA-0095, issue 2, 2009

3.4 Improving Old and Implementing New SCIAMACHY Nadir UV-VIS Products

S. Hrechanyy, K. Kretschel, G. Lichtenberg, M. Meringer

In 2009 version 5 (V5) of the SCIAMACHY off-line processor was implemented and delivered to ESA. Compared to the previous version, a number of the new features had been introduced. From the UV-VIS bands in nadir geometry V5 of the processor now retrieves the following new products:

- BrO vertical columns
- SO₂ vertical columns (two scenarios are considered: anthropogenic pollution and volcanic eruption)
- OCIO slant columns
- H₂O vertical columns

All new products were verified under the auspices of the SCIAMACHY Quality Working Group (SQWG) using the extensive verification data set containing 180 orbits equally distributed over the SCIAMACHY mission. The delivery of V5 to ESA was required within a limited time period. Therefore, in the follow-up after the submission deadline, it was required to identify and remove some of the remaining shortcomings.

One of them concern fitting a low-order polynomial for accounting the broadband molecular and aerosol scattering (*Richter 2006*). After implementation it turned out that the number of polynomial coefficients for OCIO retrieval was not optimal. This led to a slight disagreement, which, however, was found acceptable. However it was well demonstrated that after correcting the polynomial degree, the agreement between the reference algorithm of IUP-IFE, University of Bremen and the off-line processor improves significantly, i.e. the offset between the two data sets decrease noticeably (fig. 3-7). Thus the improvement will be introduced into V6 of the SCIAMACHY off-line processor planned for release in 2010.

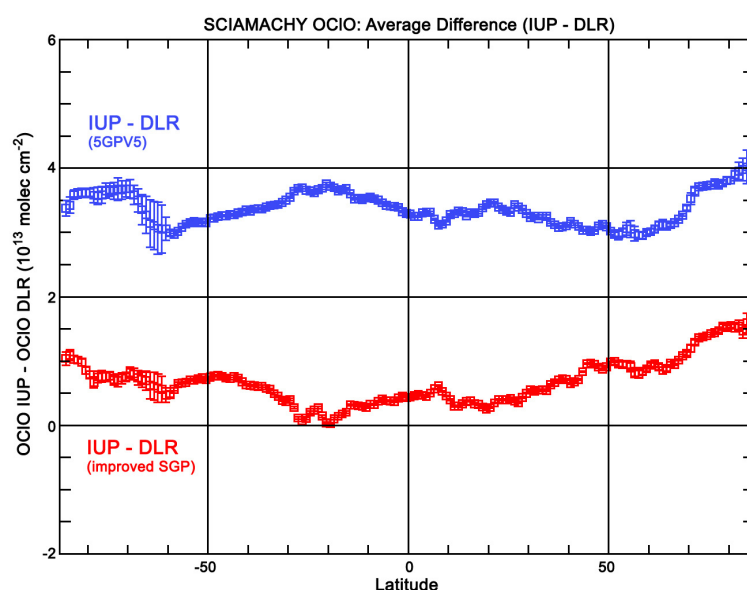


Fig. 3-7: Differences between OCIO slant columns as retrieved with the IUP reference versus the current operational (blue) and versus the improved algorithm (red).

The SQWG also recommended the implementation of two new products into V6 of the off-line processor – formaldehyde (HCHO) and glyoxal (CHOCHO). Both species play a role in pollution since they are formed during the oxidation of volatile organic compounds (VOCs) emitted by plants, anthropogenic activities (not unambiguously determined yet), and biomass burning. Formaldehyde and glyoxal can also be directly emitted by fires without an intermediate oxidation step. Although the later process represents only a small part of the global emission for both species, it can nevertheless be locally important during intense fire events. Due to a rather short lifetime of formaldehyde and glyoxal, their distribution maps, obtained by the SCIAMACHY, represent the emission fields of their precursors, VOCs.

The descriptions of reference algorithm as well as all the cross-sections for formaldehyde and glyoxal retrievals were delivered to DLR by the Belgian Institute for Space Aeronomy (BIRA) (*De Smedt et al. 2008*) and by the IUP (*Wittrock et al. 2006*), respectively. Both retrievals are based on the DOAS technique. For the formaldehyde retrieval the spectral region of 328.5-346 nm was recommended to avoid any correlation with an instrument polarization structure around 360 nm. The absorption cross-sections of HCHO, O₃, NO₂, BrO, OClO, a Ring spectrum, which accounts for Raman scattering, and a polynomial of the fifth order are included in the fitting procedure. Before conversion to the vertical columns, the slant columns have to be normalized by subtracting the slant columns measured over the Pacific Ocean (180°-220° longitude), where the only source of formaldehyde is methane oxidation. After the conversion to the vertical columns, part of HCHO, 'stolen' during the previous procedure, has to be re-added to the final vertical column by adding of the mean vertical column calculated by the tropospheric chemistry model IMAGES (*Müller and Brasseur 1995*). This normalization is necessary to compensate for the offsets introduced by the solar reference measurements and interferences by other absorbers. The very preliminary comparison of uncorrected HCHO slant columns retrieved by the reference and off-line processors is shown on fig. 3-8.

For the determination of glyoxal columns, the spectral region 435-457 nm was selected. In this case, the absorption cross-sections of CHOCHO, O₃, NO₂, H₂O, O₄, a Ring spectrum and a cubic polynomial are included in the fitting procedure. The normalization of the CHOCHO slant columns is performed in the same way as for formaldehyde.

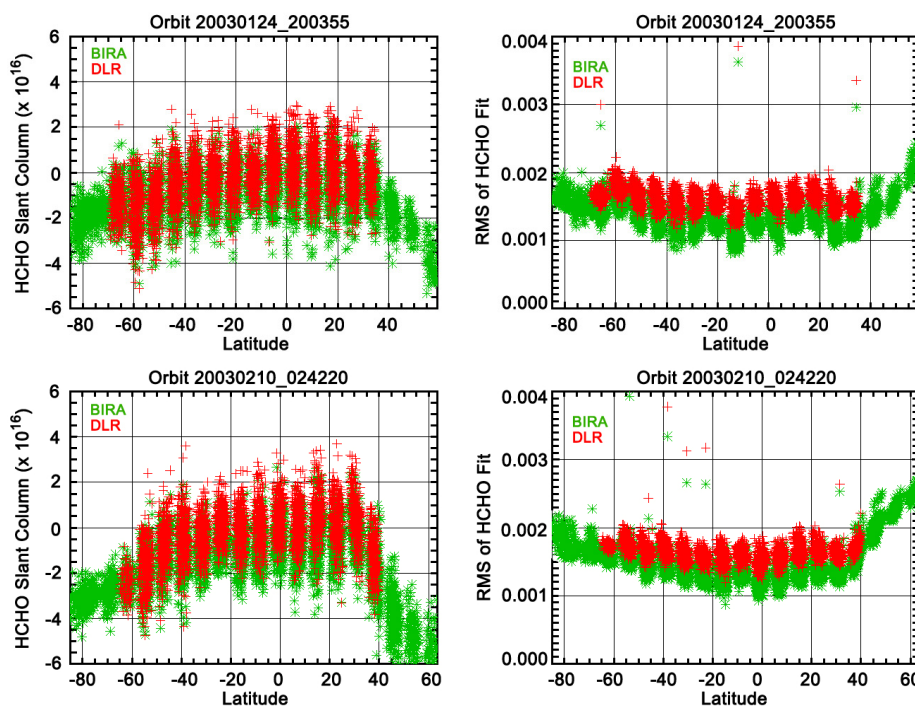


Fig. 3-8: Differences between HCHO slant columns as retrieved with the BIRA reference (green) and the operational algorithm (red) for two orbits.

References

De Smedt, I., Müller, J.-F., Stavrou, T., van der A, R., Eskes, H., and M. Van Roozendaal: Twelve Years of Global Observation of Formaldehyde in the Troposphere Using GOME and SCIAMACHY Sensors, Atmospheric Chemistry and Physics, 4947-4963, 2008

Müller, J.-F., and G. Brasseur: IMAGES: A three-dimensional chemical transport model of the global troposphere, J. Geophys. Res., 100, 1995

Richter, A.: Algorithm description SCIAMACHY OClO slant columns, Technical Note, 2006, available at http://www.iup.physik.uni-bremen.de/doas/manuals/ad_iup_bremen_oclo_nadir.pdf

Wittrock, F., Richter, A., Oetjen, H., Burrows, J. P., Kanakidou, M., Myriokefalitakis, S., Volkamer, R., Beirle, S., Platt, U., and T. Wagner: Simultaneous global observations of glyoxal and formaldehyde from space, *Geophys. Res. Lett.*, 33, L16804, doi:10.1029/2006GL026310, 2006

3.5 Carbon Monoxide and Methane Retrievals from SCIAMACHY Nadir IR Observations

S. Gimeno García, F. Schreier, G. Lichtenberg, S. Slijkhuis, B. Aberle

Carbon monoxide (CO) is an important trace gas affecting air quality and climate. It is highly variable in space and time. Methane (CH₄) is the second most important greenhouse gas after carbon dioxide (CO₂). Due to their importance for the Earth's atmosphere, CO and CH₄ are target species of several spaceborne instruments, e.g. AIRS, MOPITT, and TES from NASA's EOS satellite series, IASI on MetOp, and MIPAS and SCIAMACHY on ESA's ENVISAT mission.

The Beer InfraRed Retrieval Algorithm (BIRRA) is designed to retrieve vertical column densities (VCD's) of atmospheric gases in the near infrared (NIR) region of the electromagnetic spectrum. Recently, it has been successfully incorporated into the operational SCIAMACHY processor for retrieval of carbon monoxide Vertical Column Densities (VCD) from nadir observations in channel 8. Furthermore, BIRRA can be used to gain information on other gases absorbing in the SCIAMACHY NIR channels, the most important among them being methane and carbon dioxide.

The standard approach to estimate the unknown \mathbf{x} from a measurement vector \mathbf{y} relies on (nonlinear) least squares $\min_{\mathbf{x}} |\mathbf{y} - \mathbf{F}(\mathbf{x})|^2$ where $\mathbf{F}(\mathbf{x})$ denotes the forward model describing radiative transfer and instrument. In the near infrared the forward model essentially describes atmospheric radiative transfer through Beer's law

$$I(\nu) = r(\nu) I_{Sun}(\nu) \exp\left(-\sum \alpha_m \tau_m(\nu)\right) \otimes S(\nu, \gamma) + b(\nu)$$

where τ_m is the optical depth of the molecule 'm' along the entire line-of-sight (Sun-ground-satellite) for the reference atmosphere, $S(\nu, \gamma)$ is the spectral response function, and r and b denote surface reflectivity and baseline correction. The state vector \mathbf{x} to be retrieved comprises the scaling factors α_m for the molecular VCDs, the slit function half width γ , and polynomial coefficients for reflectivity and baseline.

Carbon Monoxide

For the retrieval of carbon monoxide vertical column densities with BIRRA, level 1 data of SCIAMACHY channel 8 applying an improved dynamical bad & dead pixel mask have been used. Surface reflectivity was modelled with a second order polynomial, whereas the baseline was ignored. Scaling factors for CO, CH₄, and H₂O were fitted along with the Gaussian slit function half widths and the reflectivity coefficients. To compensate for changes in photon path length due to scattering with aerosols and clouds as well as for variations in meteorological conditions, the CO VCD is scaled by the CH₄ VCD according to

$$x_{CO} = N_{CO}^{ref} \alpha_{CO} / \alpha_{CH4}$$

where N_{CO}^{ref} is the reference CO VCD.

Apart of the instrument bad & dead pixels, the CO VCD retrieval is sensitive to the spectral pixels chosen for the fit. The 4283-4302 cm⁻¹ fitting window comprises six CO absorbing lines with strong interferences from overlapping CH₄ and H₂O lines. So, if either the spectroscopic data or their vertical distribution is not properly treated, CH₄ or H₂O absorption features can be misinterpreted as belonging to CO, thus leading to wrong CO estimates. Fig. 3-9 shows results of CO VCDs and their fit errors averaged over February 2004. Including all CO lines in the fit ('1/2/3/4/6'), the absolute values of the errors are the highest. Excluding CO line no. 3 from the fit leads to better CO results. However, the

masking of the extra CO spectral lines ('2' and '5') which also overlap with H₂O lines is unclear. The combination '1/2/4/5/6' produces the smallest errors, whereas the combination '1/4/6' captures the North-South gradient the best.

The solar spectrum used in the radiative transfer model impacts the retrievals. The use of the Kurucz model solar spectrum instead of the SCIAMACHY measured sun mean reference (SMR) affects α_{CO} whereas it leaves the proxy α_{CH_4} almost unchanged.

CO VCDs have been processed for several years from 2003 to 2009 using the BIRRA algorithm and a new version of the bad and dead pixel mask. Fig. 3-10 illustrates the annual mean of CO vertical columns for the years 2003, 2004, and 2005. All annual averages exhibit high densities at South East Asia due anthropogenic emissions and at Central Africa due to high density of biomass burnings.

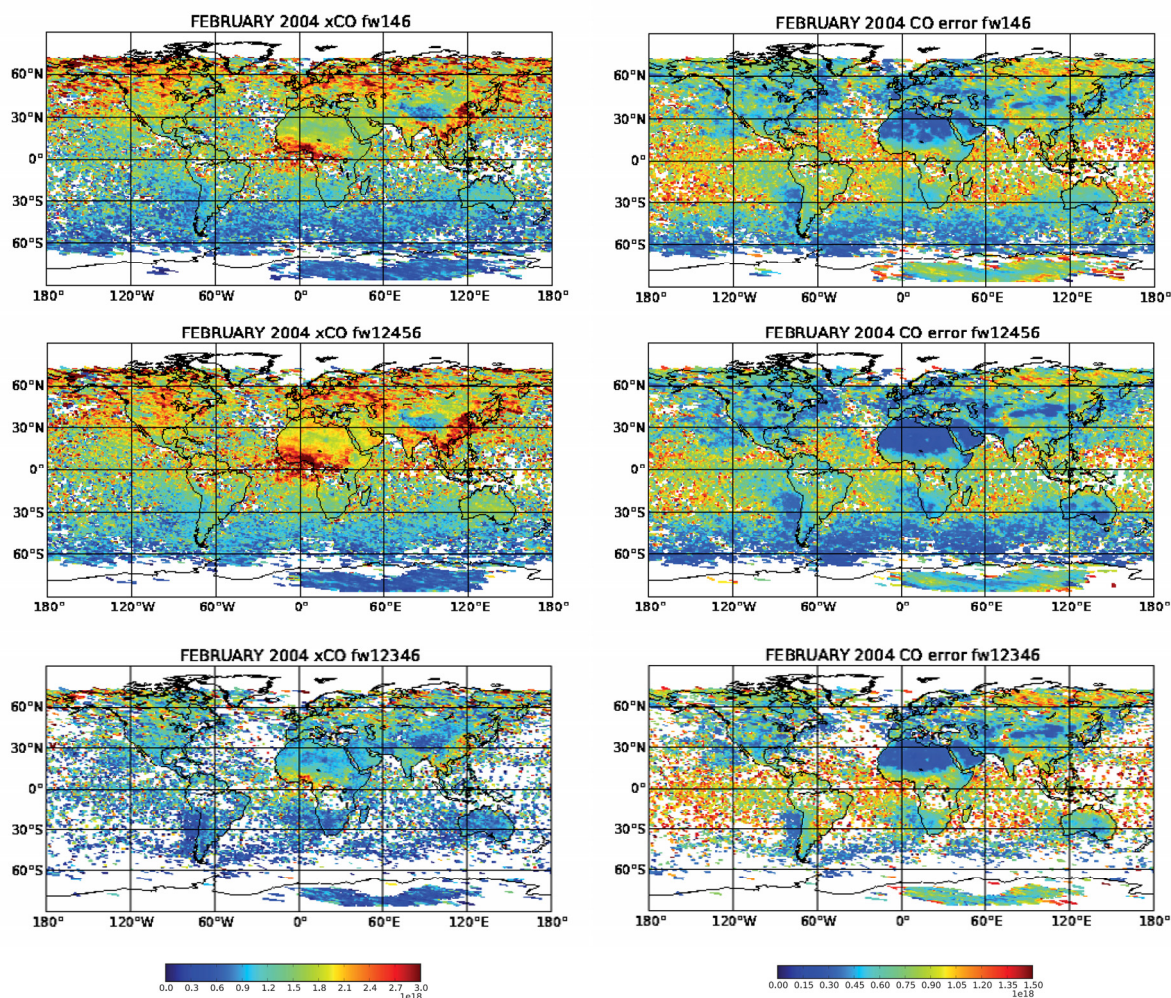


Fig. 3-9: Retrievals using the CO lines 1/4/6 (top), 1/2/4/5/6 (middle) and 1/2/3/4/6 (bottom). The left column refers to xCO and the right column to the xCO retrieval error.

Methane

For the retrieval of methane vertical column densities with BIRRA, level 1 data of SCIAMACHY channel 6 applying the same improved dynamical bad & dead pixel mask as in the case of carbon monoxide have been used. Again, surface reflectivity was modelled with a second order polynomial and the baseline was ignored. Scaling factors for CH₄, CO₂ and H₂O were fitted along with the Gaussian slit function half width and the reflectivity coefficients. CH₄ and specially CO₂ are well-mixed atmospheric gases. Hence, for the methane retrieval, CO₂ can be used as a proxy for changes in photon path lengths, climatological conditions, etc.

The results presented here correspond to retrievals using only the spectral fitting window 1629-1671 nm containing one weak carbon dioxide absorption band and much stronger CH₄ and H₂O absorption

lines. This makes the retrieval of accurate vertical column densities of CO₂ using only this spectral information quite difficult thus leading to insufficient and inappropriate results. Fig. 3-11 shows that the errors of α_{CO_2} are one order of magnitude higher than those of α_{CH_4} . Since the accuracy requirements for CH₄ are quite strict, i.e. errors should not exceed a few percent, the excessive CO₂ errors prevent accomplishing such demanding requirements. The xCH₄ errors follow a similar pattern of the errors of α_{CO_2} , or, in other words, the errors in the CO₂ VCD estimation are the main contribution to the errors in xCH₄. Hence, CO₂ retrieval in the fitting window 1629-1671 nm seems not to be suitable to be used as a proxy. A better option would be to use the CO₂ 1.58 μ m stronger absorption band. Thus an enhanced version of BIRRA allowing fitting several micro-windows simultaneously is currently under development.

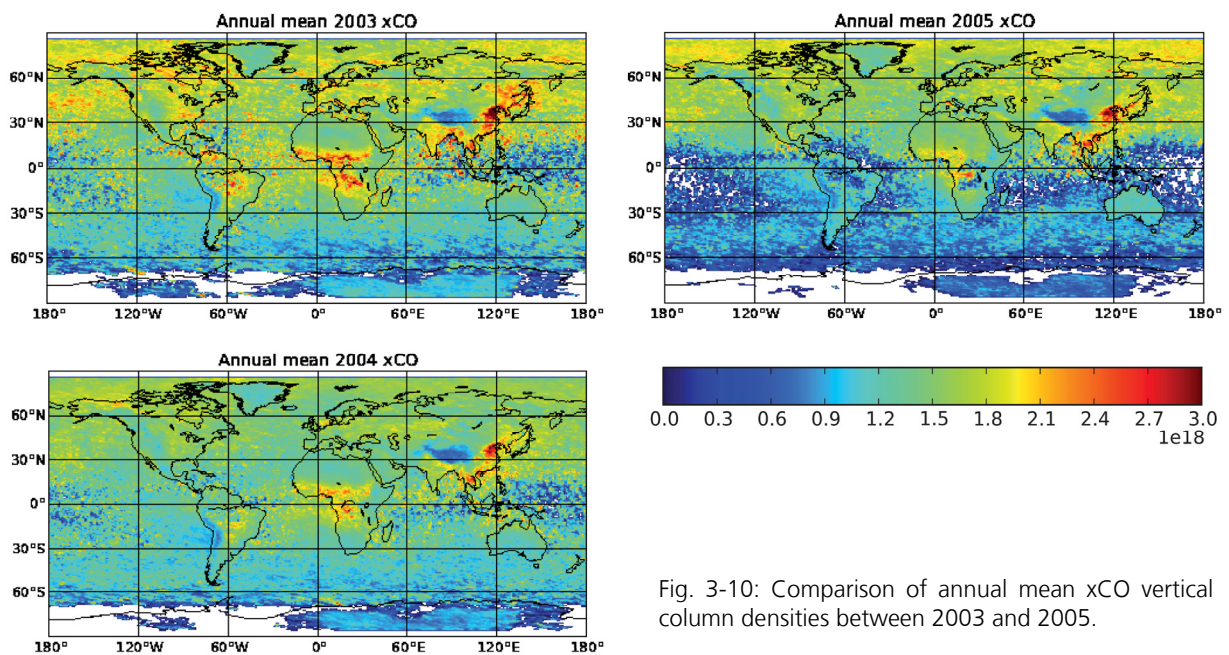


Fig. 3-10: Comparison of annual mean xCO vertical column densities between 2003 and 2005.

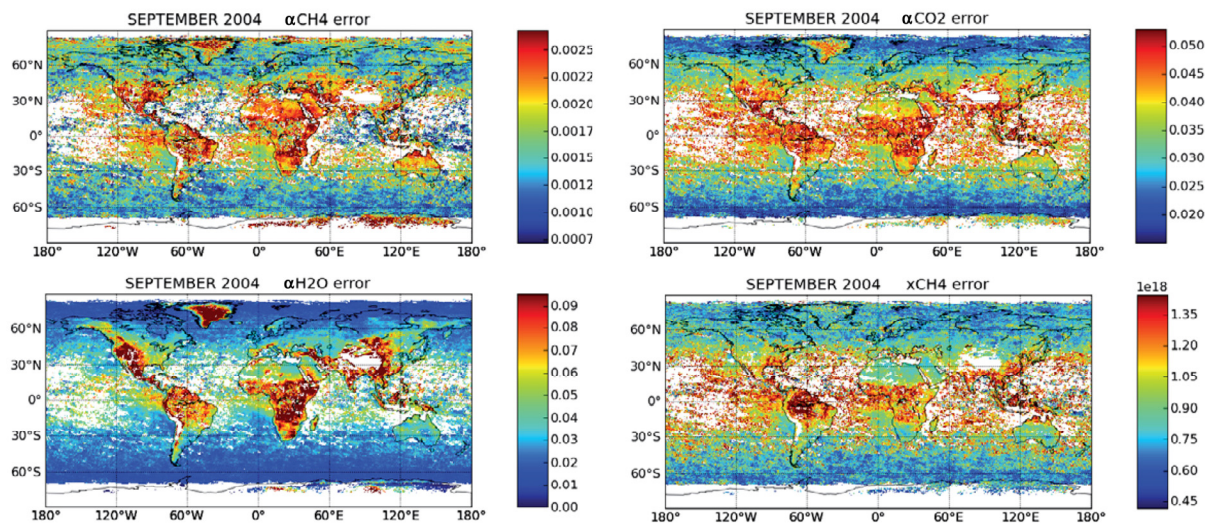


Fig. 3-11: The errors of α_{CH_4} , α_{CO_2} and xCH₄.

3.6 Comparing Carbon Monoxide Retrievals from SCIAMACHY and AIRS Nadir Observations

F. Schreier, S. Gimeno García, G. Lichtenberg, P. Hoffmann (University of Leipzig)

Verification and validation is mandatory in computational science and has been established as an integral part when assessing atmospheric sounding missions. Whereas verification ('is the code correct?') is frequently performed by means of code intercomparisons (e.g. von *Clarmann et al. 2002*, *Melsheimer et al. 2005*), a comparison of retrieval results with independent characterizations of the atmospheric state is essential for validation ('is it the correct code?'). Clearly the true state of the atmosphere is difficult to obtain, so comparisons with retrievals using other remote sensing instruments are frequently used.

Nadir sounding of molecular concentrations is well established in atmospheric remote sensing. Concentration profiles and/or vertical column densities (VCD) are successfully retrieved from data recorded by infrared (IR) as well as UV instruments. For the operational level 2 data processing of SCIAMACHY near IR observations, the Beer InfraRed Retrieval Algorithm (BIRRA) has been implemented as our standard method but also retrieves certain trace gases in the operational processor (see also previous chapter 3-5). In view of the similarities between column density retrievals in the near and mid IR, a modified version of BIRRA called CERVISA (Column Estimator Vertical Infrared Sounding of the Atmosphere) has been developed recently for level 1-2 processing of nadir thermal IR sounding data.

The BIRRA and CERVISA forward models are based on MIRART/GARLIC, a line-by-line code for arbitrary observation geometry (up, down, limb), instrumental field-of-view and line shape. It provides Jacobians by means of automatic differentiation and has been verified in extensive intercomparisons (e.g. von *Clarmann et al. 2002*, *Melsheimer et al. 2005*). The intensity (radiance) I at wavenumber ν received by an instrument is described by the equation of radiative transfer. The instrument is taken into account by convolution of the monochromatic intensity spectrum with a spectral response function. In the NIR, reflected sunlight becomes important, whereas thermal emission is negligible. For clear sky observations scattering can be neglected, hence the monochromatic radiation is essentially described by

$$I(\nu) = r(\nu) I_{Sun}(\nu) \exp\left(-\sum \alpha_m \tau_m(\nu)\right)$$

where r is surface reflectivity, τ_m is the climatological reference optical depth of molecule m along the entire line-of-sight (Sun-ground-satellite) for the reference atmosphere, and α_m are the density scaling factors to be retrieved. In the mid (thermal) infrared solar irradiance can be neglected, and the monochromatic intensity is a combination of attenuated surface emission and thermal emission of the atmosphere,

$$I(\nu) = \varepsilon(\nu) B(\nu, T_{Surf}) e^{-\tau} + \int B(\nu, T) \exp^{-\tau'(\nu)} d\tau' \quad \text{with } \tau = \sum_m \alpha_m \tau_m$$

Carbon monoxide (CO) is an important trace gas affecting air quality and climate and highly variable in space and time. CO is a target species of several space-borne instruments, e.g. AIRS, MOPITT, and TES from NASA's EOS satellite series, and MIPAS and SCIAMACHY on ESA's ENVISAT.

This intercomparison is based on SCIAMACHY Level 1c data of October 2003. In this observation period large biomass fire existed, particularly in Mozambique. We expected them to be clearly visible in CO densities derived from nadir sounding instruments. For the retrieval of CO VCDs with BIRRA, level 1 data of SCIAMACHY channel 8 have been used; a single spectrum comprises 51 data points in the interval 4282.686 to 4302.131 cm^{-1} . The surface reflectivity was modelled with a second order polynomial, baseline was ignored. Scaling factors for CO, CH₄ and H₂O were fitted along with the Gaussian slit function half width and the reflectivity coefficients. CO column density retrievals from AIRS were performed for three orbits (7868, 7889, and 7996 at October 26, 27, and 28) passing over Mozambique. Note that the October 26 and 28 data originate from dayside observations, whereas orbit 7889 is nighttime. In accordance with *McMillan et al. (2005)* the 2181-2220 cm^{-1} micro-window containing 42 spectral points was used. In addition to CO, CO₂, H₂O and N₂O scaling factors, surface temperature was fitted, too.

In fig. 3-12 a comparison of SCIAMACHY and AIRS monthly mean carbon monoxide vertical column densities for October 2003 are shown. Note that a single AIRS L1 granule has 9×1350 spectra, so an AIRS orbit gives more than 20 000 observations; On the other hand, a SCIAMACHY state typically consists of 260 spectra, resulting in about 2000 spectra per orbit.

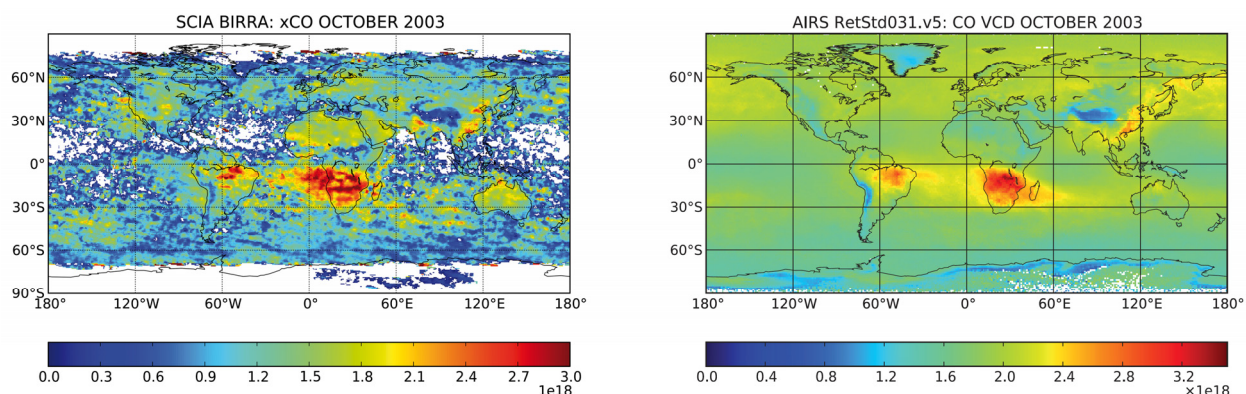


Fig. 3-12: Comparison of October 2003 CO vertical column densities. Single observations have been regridded and averaged into a $2.5^\circ \times 2.5^\circ$ global grid. AIRS CO VCD represent the field *CO total column A* of the official level 3 product version v.5.

In fig. 3-13 results of CERVISA retrievals using AIRS L1 data (AIRIBRAD) from three orbits overpassing south-east Africa are compared with the 'official' AIRS L2 data distributed by NASA (AIRX2RET). CO column densities, given as a function of latitude and longitude, have been averaged in 1° latitude bins, with 'bad' retrieval results (e.g. least squares return code indicating failure, $VCD_{CO} > 10^{19} \text{ cm}^{-2}$) filtered out. A reasonable good agreement between CERVISA and AIRX2RET is only found for low latitudes, whereas for high latitudes discrepancies become evident. For October 27th the corresponding results derived from SCIAMACHY orbit 8663 are shown, too. The CO averaged over all longitudes within a 1° latitude bin displays larger scatter (see discussion above). The enhanced CO is significantly higher and slightly shifted to the south. Clearly a perfect match of AIRS and SCIAMACHY derived VCDs cannot be expected for several reasons, such as e.g. different altitude sensitivities of near and mid infrared spectra, SCIAMACHY daytime versus AIRS night time observations, slightly different spatial coverage.

Ongoing work on CERVISA will focus on code improvement, e.g. aerosol/cloud and spectral response function modelling and optimization, and retrievals using AIRS Level 2 water profiles.

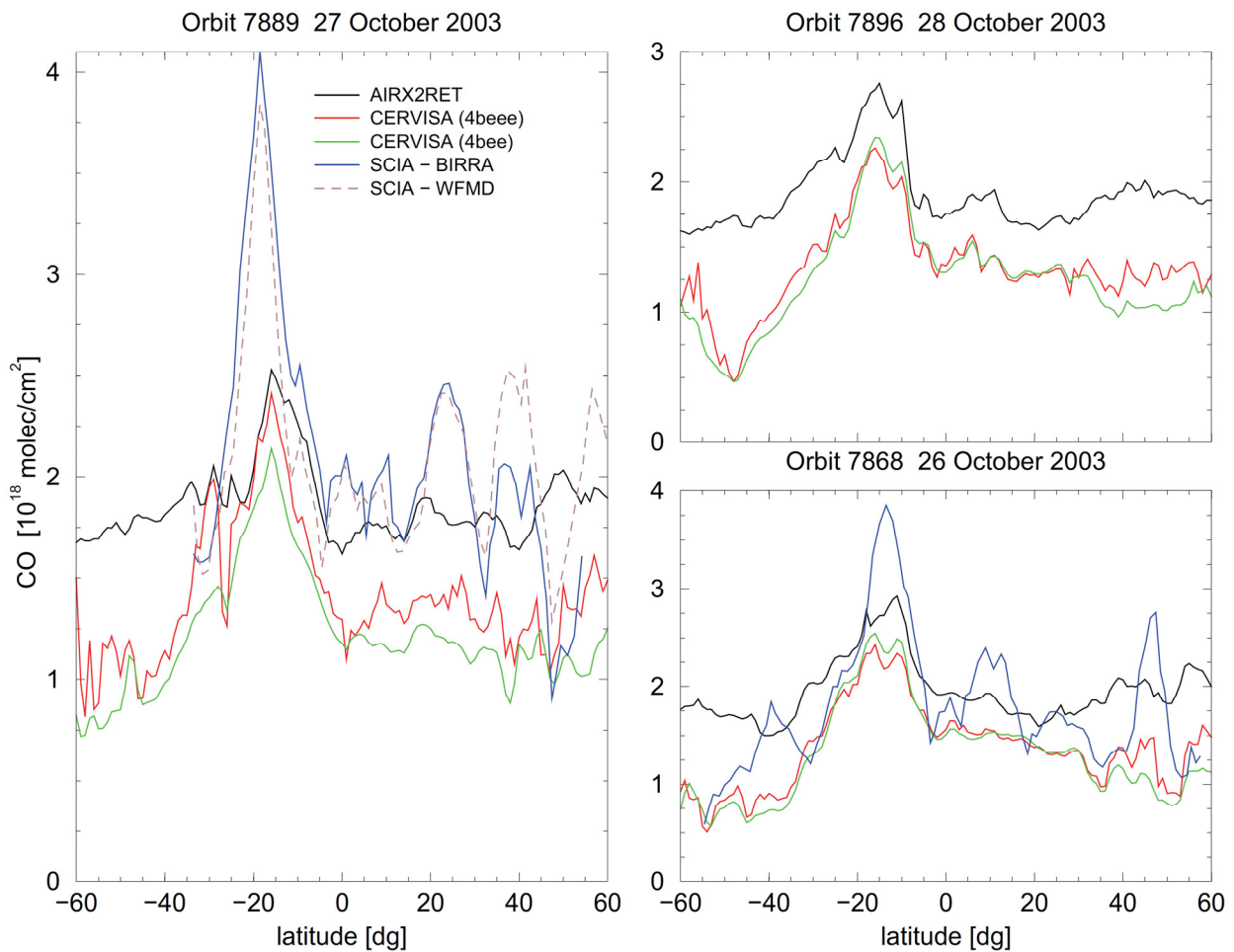


Fig. 3-13: Comparison of CO vertical column densities as a function of latitude. For CERVISA 4 gases, a constant baseline correction, and surface emissivity as a linear or quadratic polynomial in wavenumber were fitted (labels "4bee" and "4beee").

References

von Clarmann, T., M. Höpfner, B. Funke, M. López-Puertas, A. Dudhia, V. Jay, F. Schreier, M. Ridolfi, S. Ceccherini, B.J. Kerridge, J. Reburn, and R. Siddans: Modeling of Atmospheric Mid Infrared Radiative Transfer: The AMIL2DA Algorithm Intercomparison Experiment. *JQSRT* 78, 381-407, doi: 10.1016/S0022-4073(02)00262-5, 2002

Melsheimer, C., C. Verdes, S.A. Bühler, C. Emde, P. Eriksson, D.G. Feist, S. Ichizawa, V.O. John, Y. Kasai, G. Kopp, N. Koulev, T. Kuhn, O. Lemke, S. Ochiai, F. Schreier, T.R. Sreerekha, M. Suzuki, C. Takahashi, S. Tsujimaru, and J. Urban: Intercomparison of General Purpose Clear Sky Atmospheric Radiative Transfer Models for the Millimeter/Submillimeter Spectral Range. *Radio Science*, 40, RS1007, doi:10.1029/2004RS003110, 2005

McMillan, W.W., C. Barnett, L. Strow, M.T. Chahine, M.L. McCourt, J.X. Warner, P.C. Novelli, S. Korontzi, E.S. Maddy, and S. Datta: Daily global maps of carbon monoxide from NASA's Atmospheric Infrared Sounder. *Geophys. Res. Letters*, 32, L11801, 2005

3.7 Constrained Regularization Methods for Ozone Profile Retrieval from UV-VIS Nadir Sensors

O. Schüssler, A. Doicu, D. Loyola

Modern spaceborne Ultraviolet and Visible (UV-VIS) nadir atmospheric chemistry instruments like GOME/ERS-2, SCIAMACHY/ENVISAT, OMI/AURA and GOME-2/MetOp measure the backscattered radiation from the Earth-atmosphere system with a relatively high spectral resolution. These measurements are used for the routine retrieval of atmospheric composition quantities such as total column amounts of ozone, NO₂, SO₂, BrO, H₂O, HCHO and OCIO. Additionally, it is also possible to derive height-resolved information about the atmospheric ozone concentration by using appropriate retrieval algorithms. The inversion in the current algorithms is typically performed by using the method of Tikhonov regularization.

In the Tikhonov regularization, the objective function involves an additional penalty term in order to stabilize the solution. The penalty term depends on the regularization matrix and the regularization parameter. Usually, the regularization matrix is chosen as the Choleky factor of a priori profile covariance matrix, in which case, it controls the smoothness of the profile as the discrete approximations to the first-order and the second-order derivative operators do. The computation of an appropriate estimate of the regularization parameter, is a crucial issue of Tikhonov regularization. With too little regularization, reconstructions deviate significantly from the a priori and the solution is said to be 'underregularized'. With too much regularization, the reconstructions are too close to the a priori and the solution is said to be 'overregularized'. Currently there is unfortunately no fail-safe regularization parameter choice method which guarantees small solution errors in any circumstance, that is, for any noisy data vector.

In the last year we designed a class of regularization methods for ozone profile retrieval which are less susceptible to the selection of the regularization parameter over a large range of values. The idea was to incorporate additional constraints into the classical regularization method which should come into play especially when the regularization parameter is too small and large deviations from the a priori profile are expected. The additional constraints are imposed on the integrated ozone profile, i.e., the vertical column, which can be computed with sufficiently accuracy by an independent algorithm like DOAS or GODFIT. Essentially, in this class of regularization methods, we control the smoothness of the profile through the regularization matrix and the magnitude of the profile through the vertical column.

In the equality-constrained version of Tikhonov regularization we formulated an optimization problem with a linear equality constraint: At the iteration step k , compute the profile deviation x_{k+1} by solving the quadratic programming problem

$$\begin{aligned} \min_x \quad & g^T x + \frac{1}{2} x^T G x \\ \text{subject to} \quad & \sum_{i=1}^n [x]_i = c \end{aligned}$$

Here G , is the Hessian matrix of the Tikhonov function, g is the gradient and c is the difference between the vertical columns corresponding to the 'exact' state vector and the a priori. For solving the above quadratic programming problem we used the null-space method, and assumed that c is a free parameter of the retrieval ranging in a chosen interval $[c_{min}, c_{max}]$. The problem to be solved was the computation of the strengths of the constraints, or more precisely, of the regularization parameter, which controls the smoothness of the solution, and of the relative vertical column, which controls the magnitude of the solution. For this purpose we adopted a simple strategy: we used an a priori chosen regularization parameter but computed the relative vertical column by using an approach which is similar to the L-curve method.

An inequality-constrained version of Tikhonov regularization has been derived by assuming that the total column is known with sufficient accuracy. The information on the total column should be the result of an independent retrieval, which can be performed in a distinct spectral interval by using

appropriate algorithms like DOAS or GODFIT. As opposed to the equality-constrained method, the vertical column is not a free parameter of the retrieval which is optimized by using an internal selection criterion. The proposed inequality-constrained Tikhonov regularization is of the form of the following model algorithm: At the iteration step k , compute the profile deviation x_{k+1} by solving the quadratic programming problem

$$\min_x \mathbf{g}^T \mathbf{x} + \frac{1}{2} \mathbf{x}^T \mathbf{G} \mathbf{x}$$

$$\text{subject to } \sum_{i=1}^{n_t} [x]_i \leq c_{max} \quad \wedge \quad \sum_{i=1}^n [x]_i \geq c_{min}$$

Here, the layer n_t delimits the tropospheric from the stratospheric region, while the quantities c_{min} and c_{max} represent a lower and an upper bound imposed on the vertical column. The reasons for this choice of constraints are the following:

- In general, the constraints should be linearly independent since otherwise one of the constraints can be omitted without altering the solution.
- As the nadir radiance is less sensitive to profile variations in the troposphere, the first constraint does not allow large profile deviations in the stratospheric region.
- The second constraint ensures a sufficiently large deviation of the profile (with respect to the a priori) over the entire altitude range.

The above quadratic programming problem has been solved by using a dual active set method. This method generates dual-feasible iterates by keeping track of an active set of constraints and does not have the possibility of cycling. An extensive numerical analysis evidenced that:

- The constrained versions of Tikhonov regularization are more stable than Tikhonov regularization with respect to underestimations of the regularization parameter.
- For equality constraints, the selection of the bounds c_{min} and c_{max} is uncritical, and the value of the relative vertical column is only informative. By contrast, for inequality constraints, the information about the relative vertical column should be sufficiently accurate.
- The computing time of the equality-constrained Tikhonov regularization with an inner loop resembles that of the ordinary method.

The application of the constrained regularization methods showed significant improvements in ozone profile retrieval and seems to be a promising tool for ozone retrieval from UV-VIS backscatter measurements as provided by the GOME family of instruments.

3.8 Data Processing for Limb Emission Sounding

F. Schreier, J. Xu, M. Birk (IMF-EV), G. Wagner (IMF-EV)

Due to its high vertical resolution and high sensitivity to minor trace gases, limb sounding is a superior approach for atmospheric remote sensing. In contrast to UV-VIS instruments such as SCIAMACHY employing back-scattered solar radiation, infrared (IR) and microwave limb emission sounding is also advantageous because of its day/night independence. In the past we already had been involved in IR limb sounding radiative transfer and retrieval, e.g. for MIPAS (Michelson Interferometer for Passive Atmospheric Sounding) aboard ENVISAT.

TELIS (TeraHertz Limb Sounder) – a further development of the airborne THOMAS system – is a balloon borne three channel heterodyne spectrometer (DLR, SRON, RAL cooperation) that has been flown successfully together with MIPAS-B in March 2009 in Kiruna. In the framework of the SMILES validation campaign another successful flight occurred recently in January 2010. SMILES (Superconducting Submillimeter-Wave Limb-Emission Sounder) has been launched September 2009 and is flown onboard

the Japanese experiment module KIBO onboard the International Space Station (ISS). Personnel of IMF-AP is contributing to the SMILES algorithm team.

In preparation of the analysis of the TELIS campaign in Kiruna, March 2009, simulations using the FASCODE line-by-line code (with the help of the PFUI interface, see our Annual Report 2007) have been performed. This sensitivity study clearly illustrates the importance of 'correct' pressure, temperature, and water vapour profiles for the far infrared spectra that will be used for retrieval of hydroxyl (OH) concentrations. The limb sequence on the left of fig. 3-14 has been computed using profiles from the 'Subarctic Winter' model atmosphere, whereas on the right hand side temperature and H₂O data retrieved from the MIPAS-B thermal infrared limb emission sensor (G. Wetzel, FZK-IMK, private communication) have been used. For tangent points at high altitudes this leads to a much better agreement with the observed spectra (shown in green); for the low altitude tangent spectra the discrepancies are most likely due to problems modelling of the water continuum.

Data processing for the TELIS 1.8 THz channel developed by DLR as well as for SMILES is performed by constrained nonlinear least squares optimization, where the forward model required for simulation of IR/microwave limb spectra is based on the MIRART/GARLIC line-by-line code, and the inversion will utilize the DRACULA regularization package. For the iterative solution of – constrained or unconstrained – nonlinear least squares problems derivatives of the model function with respect to the unknown fit parameters to be determined are required. In case of atmospheric emission spectroscopy these *Jacobians* are essentially the derivatives of the modelled IR/microwave radiation intensity (radiance) with respect to the (discretized) concentration profile of the considered molecule. The simplest approach to generate these derivatives, relying on finite difference (FD) approximations; unfortunately is computationally time consuming and inaccurate (i.e. the appropriate amount of perturbation is hard to predict). Alternatively the Jacobian can be obtained analytically by 'manually' evaluating the derivatives starting from e.g. Schwarzschild's equation for the intensity, and implementing the new formulas in the radiative transfer code. However, this is as well a tedious and error-prone process.

Automatic (or algorithmic) differentiation (AD) provides a pleasant alternative to quickly generate derivative-enhanced versions of computer codes. This approach is based on the observation that every model implemented as a computer program is essentially formulated in terms of elementary mathematical operations (sums, products, powers) and elementary functions. In contrast to integration, differentiation is based on a few simple recipes such as the chain rule, and these can be performed automatically by some kind of precompiler, taking a computer code as input and delivering a code that additionally produces derivatives with respect to some chosen variables. Furthermore AD is advantageous as it provides exact derivatives (as far as the underlying model function to the differentiated is exact.)

For limb sounding retrievals a variant of GARLIC called PILS (Profile Inversion for Limb Sounding) is currently developed. Jacobians have been implemented using the TAPENADE AD tool for Fortran 90. The new code has been verified by intercomparisons with FD derivatives, clearly demonstrating the sensitivity of FD approximations to the appropriate perturbation (fig. 3-15). Moreover the tests showed the efficiency of this approach: Computing a Jacobian for a molecular concentration profile discretized at 12 altitudes increases computing time by about a factor 2 compared to the spectrum evaluation alone, whereas the FD Jacobian with 12 columns would have increased the time by a factor 13. These results confirm earlier experience with MIRART augmented by the ADIFOR Fortran77 AD.

This promising new code appears to be an accurate, yet efficient program ready to solve the nonlinear inverse problems arising in the analysis of recent atmospheric limb sounding measurement data from ODIN, TELIS, or SMILES missions.

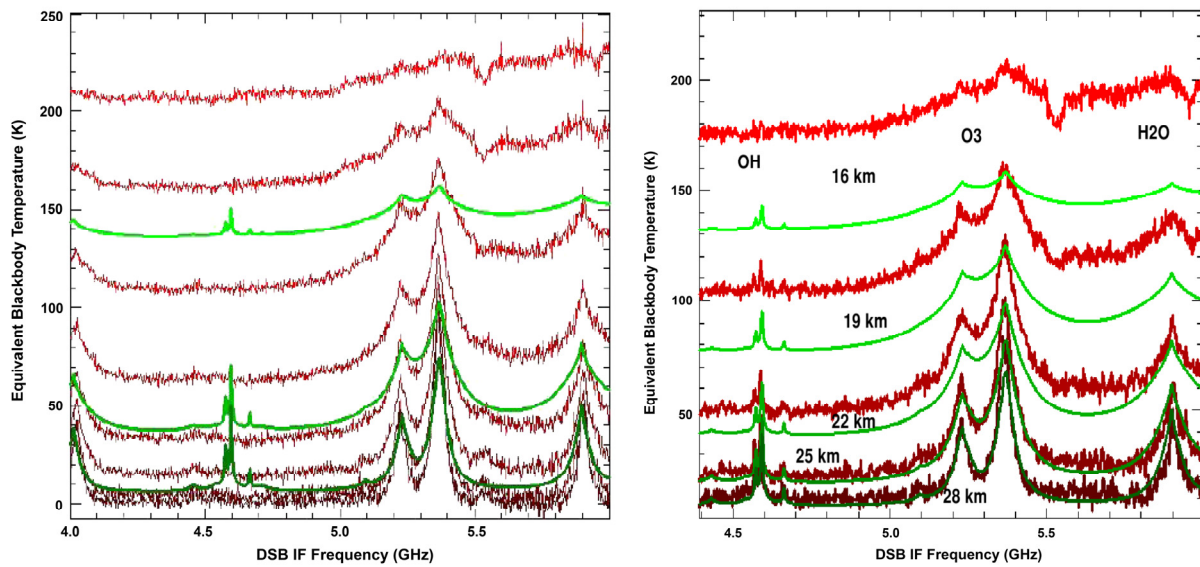


Fig. 3-14: Comparison of infrared spectra (micro-window around the OH triplet at 1842 GHz) observed with TELIS (red) with simulated spectra (green). The left panel illustrates simulations using model atmosphere data. In the right panel simulations were based on atmospheric data/profiles retrieved from MIPAS observations.

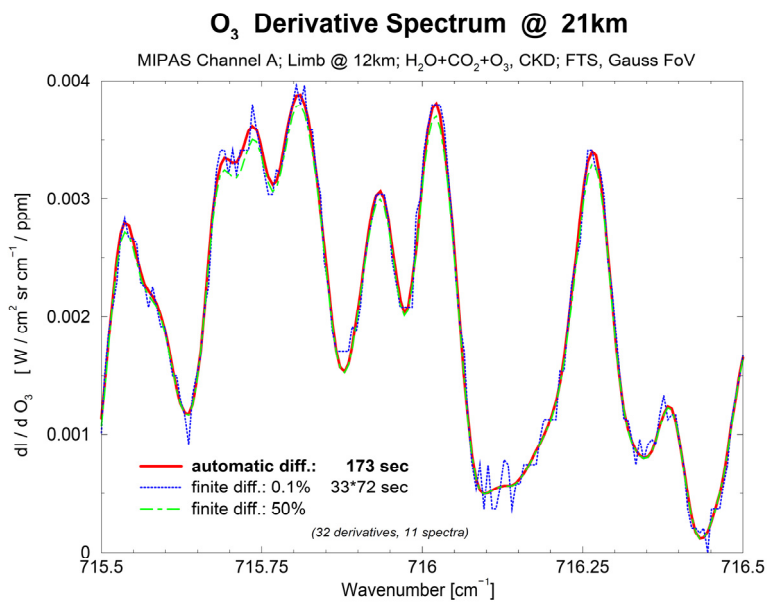


Fig. 3-15: Comparison of derivatives computed by Automatic Differentiation versus finite difference (for details see text).

3.9 First Results of a Runge-Kutta Type Inversion Method for SCIAMACHY and IASI Retrievals

M. Szopa, A. Doicu, F. Schreier, T. Trautmann, C. Böckmann (University Potsdam)

Regularization methods for the inversion of infrared sounding observations are currently investigated. An iterative Runge-Kutta type method for nonlinear ill-posed problems has been implemented and its performance has been studied using synthetic measurements in 2009. Comparisons with Tikhonov type inversion with a priori regularization parameter selection indicate that both methods are of similar accuracy; however, the Runge-Kutta method is less sensitive to regularization parameter variations. We had shown that this method can be successfully applied both to limb (SCIAMACHY) and nadir (IASI on MetOp) infrared sounding instruments.

Regularization

The standard approach to estimate the unknown \mathbf{x} from a measurement vector \mathbf{y} relies on (nonlinear) least squares

$$\min_x \|\mathbf{y} - \mathbf{F}(\mathbf{x})\|^2$$

Here \mathbf{F} denotes the forward model, and the unknown state vector \mathbf{x} is comprised of the geophysical and auxiliary (e.g., instrumental) parameters. Typically, only noisy data are available due to measurement errors. Therefore we distinguish the 'correct' data \mathbf{y} from the available noisy data $\mathbf{y}^\delta = \mathbf{y} + \delta$. Thus only an estimate \mathbf{x}^δ of the correct state vector \mathbf{x} can be obtained.

Because of the ill-posed nature of vertical sounding inverse problems, regularization is indispensable, i.e.,

$$\min_x \left(\|\mathbf{y} - \mathbf{F}(\mathbf{x})\|^2 + \lambda \|\mathbf{L}(\mathbf{x} - \mathbf{x}_a)\|^2 \right)$$

Where \mathbf{x}_a is an a priori state vector, \mathbf{L} is a regularization matrix, and λ is a regularization parameter.

For linear inverse problems Tikhonov regularization with various parameter choice methods (e.g., L-curve, GCV, etc.) has been used extensively. For nonlinear Tikhonov regularization the Iteratively Regularised Gauss-Newton (IRGN) method and the regularized Levenberg-Marquardt method have been utilized as efficient solvers (Doicu et al., 2002; Doicu et al., 2003). These and further methods have been implemented in the DRACULA (Advanced Retrieval Atmosphere Constrained & Unconstrained Least squares Algorithms) library (Doicu et al., 2004).

Runge-Kutta Regularization

The Runge-Kutta method is a popular family of algorithms for solving initial value problems (IVP). Applied to a problem of the form $\dot{\mathbf{x}}(t) = \Psi(t, \mathbf{x}(t))$, with $\mathbf{x}(0) = \mathbf{x}_0$, it is characterized by the following iterative procedure:

$$\mathbf{x}_{k+1} = \mathbf{x}_k + \tau_k \sum_{i=1}^s b_i \Psi(t + c_i \tau_k, \mathbf{v}_i),$$

$$\mathbf{v}_i = \mathbf{x}_k + \tau_k \sum_{j=1}^s a_{ij} \Psi(t + c_j \tau_k, \mathbf{v}_j)$$

with method-specific parameters

$$\mathbf{A} \equiv (a_{ij}) \in \mathbb{R}^{s \times s}, \mathbf{b} \equiv (b_1 \dots b_s)^T \in \mathbb{R}^{s \times 1} \text{ and } \mathbf{c} \equiv (c_1 \dots c_s)^T \in \mathbb{R}^{s \times 1}.$$

Tautenhahn (1994) has shown that solving a nonlinear inverse problem $\mathbf{F}(\mathbf{x}) = \mathbf{y}$ is equivalent to solving an IVP.

$$\begin{aligned}\dot{\mathbf{x}}^\delta(t) &= \mathbf{K}^T(\mathbf{x}^\delta(t))[\mathbf{y}^\delta - \mathbf{F}(\mathbf{x}^\delta(t))], \quad 0 < t < T, \\ \mathbf{x}^\delta(0) &= \mathbf{x}_a\end{aligned}$$

where \mathbf{K} is the Jacobian. This differential equation can be readily solved using the Runge-Kutta formalism (Böckmann and Pornsawad 2008), where T plays the role of a regularization parameter. Applying the two stage ($s = 2$) scheme to (5) results in

$$\mathbf{x}_{k+l}^\delta = \mathbf{x}_k^\delta + \tilde{\mathbf{b}}^T \tilde{\mathbf{A}}^{-1} (\alpha_k \mathbf{I}_{2n} + \mathbf{B}_k)^{-1} \tilde{\mathbf{A}} \mathbf{s}_k^\delta$$

where $\alpha_k = \frac{1}{\tau_k}$ is the inverse step length, and

$$\begin{aligned}\tilde{\mathbf{b}} &= \mathbf{b} \otimes \mathbf{I}_n \\ \mathbf{s}_k^\delta &= \begin{pmatrix} \mathbf{K}_k^T(\mathbf{y}^\delta - \mathbf{F}(\mathbf{x}_k^\delta)) \\ \mathbf{K}_k^T(\mathbf{y}^\delta - \mathbf{F}(\mathbf{x}_k^\delta)) \end{pmatrix} \\ \tilde{\mathbf{A}} &= \begin{pmatrix} a_{11} & a_{12} \\ a_{21} & a_{22} \end{pmatrix} \otimes \mathbf{I}_n \\ \mathbf{B}_k &= \begin{pmatrix} a_{11} & a_{12} \\ a_{21} & a_{22} \end{pmatrix} \otimes \mathbf{K}_k^T \mathbf{K}_k\end{aligned}$$

Here \mathbf{I}_n denotes the $n \times n$ identity matrix, and the Kronecker product for two matrices $\mathbf{A} \equiv (a_{ij}) \in \mathbb{R}^{m \times n}$ and $\mathbf{B} \in \mathbb{R}^{k \times p}$ is defined as

$$\mathbf{A} \otimes \mathbf{B} = \begin{pmatrix} a_{11}\mathbf{B} & \cdots & a_{1n}\mathbf{B} \\ \vdots & \ddots & \vdots \\ a_{m1}\mathbf{B} & \cdots & a_{mn}\mathbf{B} \end{pmatrix}$$

Numerical implementations of the 1- and 2-stage Runge-Kutta type iterative regularization methods along with three test cases are described in (Böckmann and Pornsawad, 2008). Recently, this method has also been added to the DRACULA library.

Results

The Runge-Kutta regularization has been tested with synthetic spectra for both limb and nadir passive atmospheric soundings, including comparisons with the Tikhonov-type methods with a priori regularization parameter.

For testing SCIAMACHY measurements, limb observations of ozone (wavelength 520-580 nm) and BrO (337-357 nm) in the UV and carbon monoxide (wavenumber 4280-4305 cm^{-1}) in the NIR were simulated. A limb sequence starting at a tangent altitude of 13.6 km with $\Delta h_t = 3.3$ km was assumed. Gaussian noise has been added: $\text{SNR} = 300$ for O_3 and 10^3 for BrO and CO. The NIR spectra were also used to test the performance of various regularization methods for temperature sounding (with $\text{SNR} = 10^4$). In fig. 3-16 a comparison of Runge-Kutta retrieval results with the exact profile used to generate the synthetic measurements is shown. The relative error $\|\mathbf{x}^\delta - \mathbf{x}^{\text{true}}\| / \|\mathbf{x}^{\text{true}}\|$ and the number of

iterations for O_3 and BrO as a function of the regularization strength p are shown in fig. 3-17. Note that a small exponent p corresponds to strong regularization.

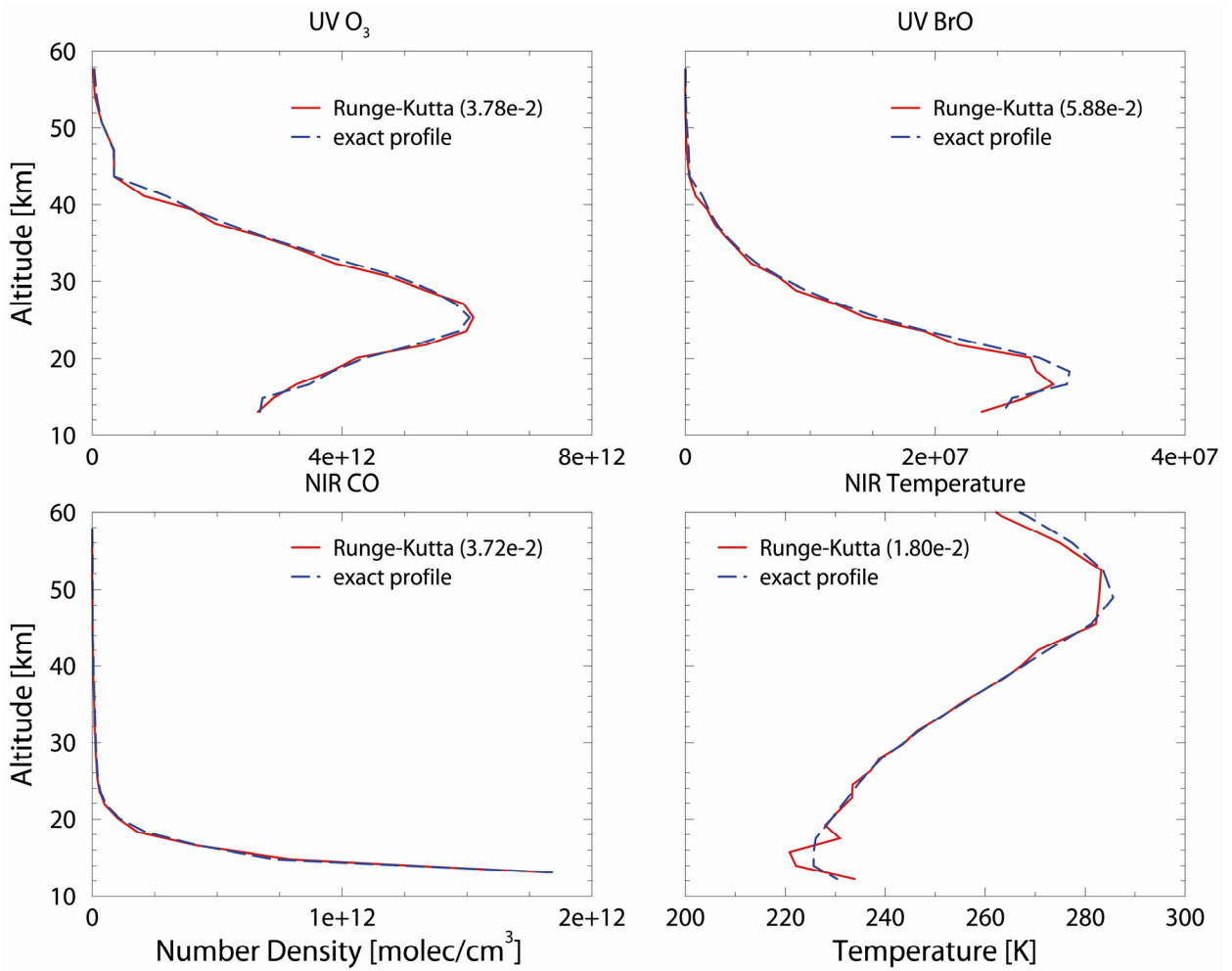


Fig. 3-16: SCIAMACHY limb sounding test cases showing the comparison of profiles retrieved with the Runge-Kutta regularization scheme with the exact profile.

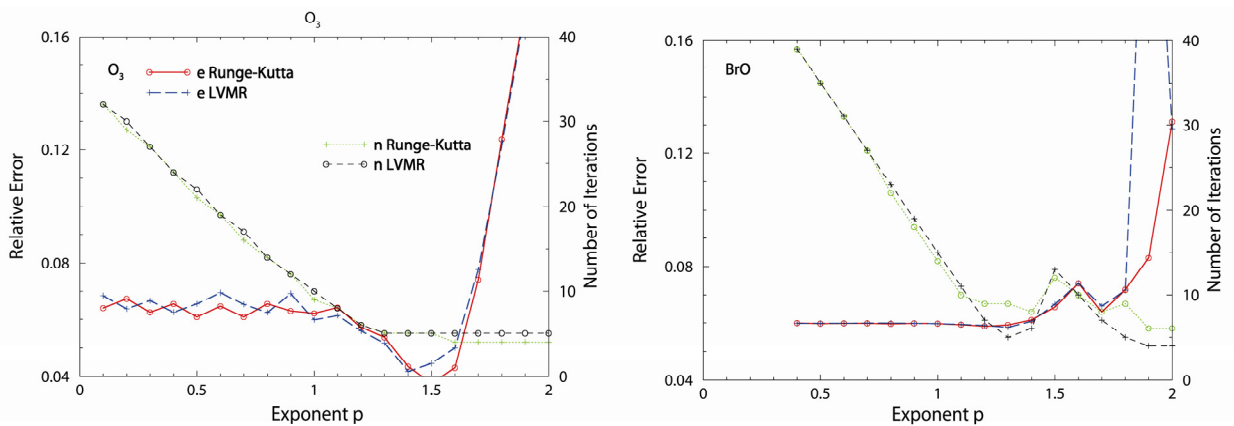


Fig. 3-17: Runge-Kutta vs. regularized Levenberg-Marquardt for the SCIAMACHY limb UV test cases. The regularization parameter is chosen as $\alpha = \sigma^p$ where σ is the noise standard deviation.

Synthetic IASI spectra in the wavenumber range $1000-1070 \text{ cm}^{-1}$ were used to test the new scheme for nadir infrared sounding. Gaussian noise with $\text{SNR} = 10^3$ was added to the synthetic spectra; H_2O and

CO₂ were considered as interfering species. Fig. 3-18 illustrates the performance of the Runge–Kutta scheme compared to the nonlinear Tikhonov regularization method.

A new regularization scheme for nonlinear inverse problems based on Runge-Kutta methods has been implemented and tested with synthetic spectra for limb and nadir sounding. In comparison to other regularization schemes Runge-Kutta is less sensitive to the correct choice of the regularization parameter w.r.t. accuracy, albeit typically a higher number of iterations is required in case of bad parameter choice. For analysis of real measurement spectra the DRACULA library with Tikhonov-type and Runge-Kutta regularization schemes is currently combined with the MIRART/GARLIC radiative transfer code providing optimized line-by-line computations and algorithmic derivatives.

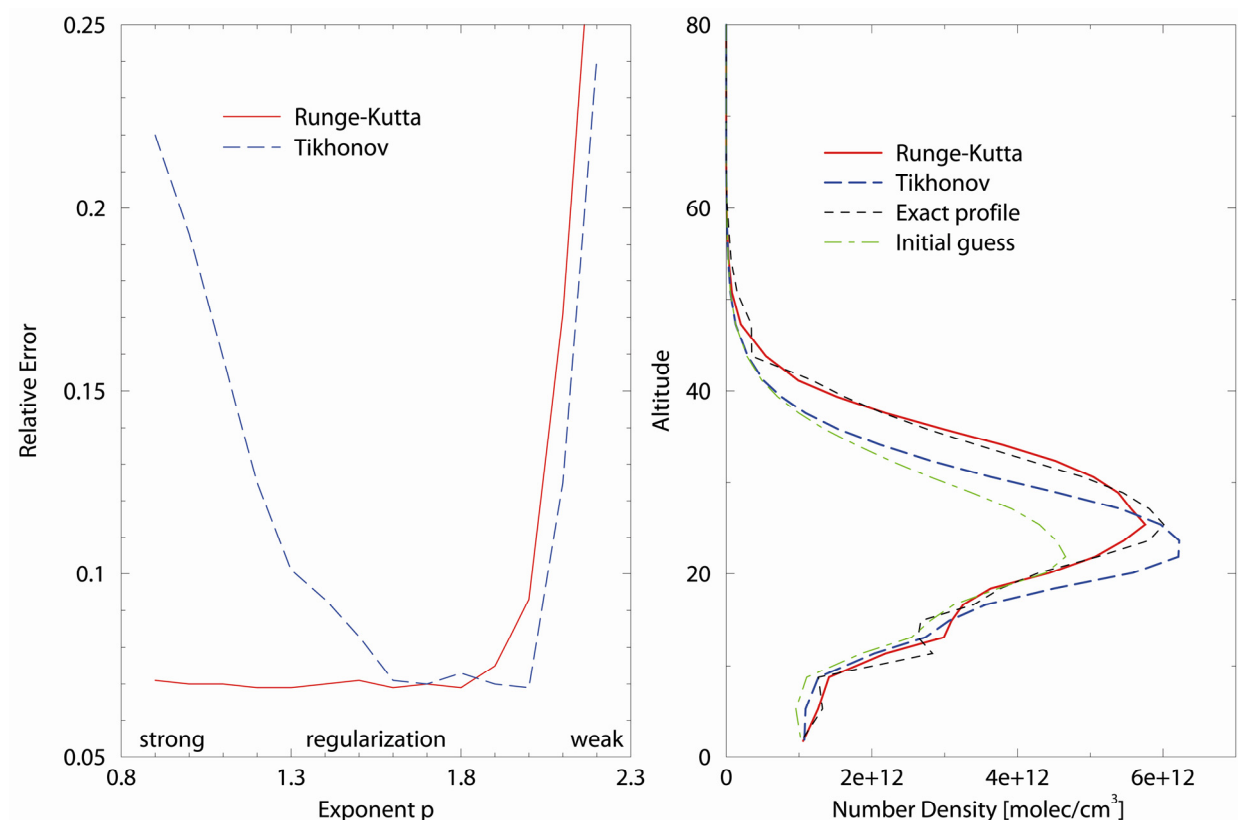


Fig. 3-18: Comparison of Runge-Kutta vs. Tikhonov regularization scheme for ozone retrievals in the infrared based on a synthetic IASI spectrum.

References

- Böckmann, C. and P. Pornsawad: Iterative Runge-Kutta-type methods for nonlinear ill-posed problems. *Inverse Problems*, 24, 025002, 2008
- Doicu, A., F. Schreier and M. Hess: Iteratively regularized Gauss-Newton method for atmospheric remote sensing. *Comp. Phys. Comm.*, 148, 214-226, doi: 10.1016/S0010-4655(02)00555-6, 2002
- Doicu, A., F. Schreier and M. Hess: Iteratively regularized Gauss-Newton method for bound-constraint problems in atmospheric remote sensing. *Comp. Phys. Comm.*, 153(1), 59-65, doi: 10.1016/S0010-4655(03)00138-3, 2003
- Doicu, A., F. Schreier and M. Hess: Iterative regularization methods for atmospheric remote sensing. *J. Quant. Spectrosc. Radiat. Transfer*, 83, 47-61, doi: 10.1016/S0022-4073(02)00292-3, 2004
- Tautenhahn, U.: On the asymptotical regularization of nonlinear ill-posed problems. *Inverse Problems*, 10, 1405-1418, 1994

3.10 Radiative Transfer in Highly Variable Cloud Scenarios

S. Gimeno García, F. Schreier, T. Trautmann

The accurate calculation of the radiative transport in the system Earth-Atmosphere is of prime importance, since the whole atmospheric and oceanic dynamics are driven by the radiative energy stored in the system. Approximative approaches have been and are currently being used for the computation of the radiative transfer (RT) in remote sensing and climate/weather modelling applications:

- Fast routines: Radiative transfer models are one-dimensional (1D), such that the impact of the neighbouring atmospheric columns is neglected.
- Coarse distributions: Spatial resolution of cloud scenes is coarse, particularly at the horizontal dimension.

Since progress in space-borne remote sensing permits accessing smaller scale structures and new computer technologies allow the handling of vast data arrays describing optical properties it might be the time to overcome the limits of the approximations listed above. The associated applications should be ready to deal with more complexity in optical fields and with the general solution of the radiative equation in order to be able to reproduce the real radiance and flux fields. In the past year work has continued to examine the errors introduced when calculating one-dimensionally the solar radiative fluxes within coarse cloudy atmospheres.

Cloud datasets

For our investigations we use two different datasets of cloud optical properties. The first represents a diurnal cycle of shallow cumulus clouds developing over land. To produce this cloud set, the data collected at the Southern Great Plains (SGP) site of the Atmospheric Radiation Measurement (ARM) Program on 21 June 1997 was used to initialize a large-eddy model that supplied 51 highly resolved scenes of the evolving cloud every 20 minutes (*Brown et al. 2002*). The number of grid cells the cloudy scene is divided into is 64 by 64 in the horizontal and 122 in the vertical dimension. The spatial resolution amounts to 100 m (horizontally) \times 40 m (vertically). The second dataset corresponds to three different runs (29 scenes in total) of a large-eddy model simulating the evolution of a polluted marine stratocumulus at noon. The model was initialized with measurements over the Atlantic Ocean at the north of the Canary Islands within the second Aerosol Characterisation Experiment (ACE-2) on 9 July 1997 (*Chosson et al. 2007*). The supplied cloud scenes have 35 layers with a vertical resolution of 10 m, from which we use only the layers between 685 and 1025 m. Horizontally, the number of grid cells is 200 by 200 with a resolution of 50 m \times 50 m.

These two cloud datasets were used as reference for a stochastic cloud generator able to consistently add subscale variability (*Venema et al. 2009*) to the fields. Using this cloud generator, we could associate coarse resolved clouds (as used in restrictive cloud resolving models – CRM, e.g. weather and climate models) to their corresponding fine resolved surrogates (representing an approach to ‘reality’).

Radiative transfer simulations

The RT simulations were performed using the Monte Carlo Radiative Transfer model (MoCaRT, see *Gimeno García and Trautmann (2003)* for a description of the predecessor model), a flexible and versatile code that can be conveniently set for carrying out the radiation computations in several manners: either 3D ‘exact’ solution of the RT equation or a variety of approximative methods.

The radiation simulations comprised the whole solar range. Only the troposphere and the lower stratosphere (top of the atmosphere at 30 km) were considered. The gas absorption was taken into account through the correlated k-distribution (CKD) proposed by *Fu and Liou (1992)*, where the solar range is divided in 6 bands. The cloud optical properties were calculated from the microphysical properties using the Slingo parameterization (*Slingo, 1989*). The particle scattering phase function was approximated by the Henyey-Greenstein phase function. The scenario was considered to be aerosol free and the broadband surface albedo was considered to be from an agricultural region (*Henderson-Sellers and Wilson 1983*). The sun was assumed to be at the zenith.

Study

The cumulus clouds were horizontally coarsened to 16 by 16 pixels (i.e. the resolution was decreased four-fold down to 400 m), representing clouds in a restrictive cloud resolving model. Additionally, fine surrogate clouds were generated from the coarsened clouds sharing the main statistics with them (liquid water content, power spectrum, cloud cover, etc.), but including variability at the subscale. These fine surrogates represent here 'nature' and were validated with the original fine templates (Venema *et al.* 2009). The stratocumulus clouds were also horizontally coarsened 10× to 20 by 20 pixels of 500 m resolution. Again, fine surrogates of the coarsened clouds were generated at the original fine resolution.

We simulated both the RT as it would be performed in a restrictive cloud resolving model (Independent Pixel Approximation (IPA) calculations in atmospheres with coarse resolved clouds) and we carried out fully 3D calculations in atmospheres with fine resolved surrogate clouds, attempting to mimic reality.

Results

One of the results of our studies was estimating the error made by restrictive cloud resolving models when calculating the RT. We refer to the IPA calculations in coarse clouds as 'CRM' (cloud resolving model), and to the 3D calculations in the related fine clouds as 'exact'. For the comparison we have selected three quantities: transmission to the surface, albedo (reflection) at the top of the atmosphere (here at 30 km) and absorption within the whole atmospheric scene. We compared separately the results for the cumulus and for the stratocumulus clouds.

As the coarse and the related – generated – fine clouds share the main statistical properties, the radiation differences can solely arise from the resolution at which the properties are given and from the nature of the radiative transfer computations itself. The coarse clouds are technically smoother than their fine counterparts leading to overestimating albedo (albedo bias). IPA simulations neglect the horizontal transport between atmospheric columns and introduce big errors at cloud edges.

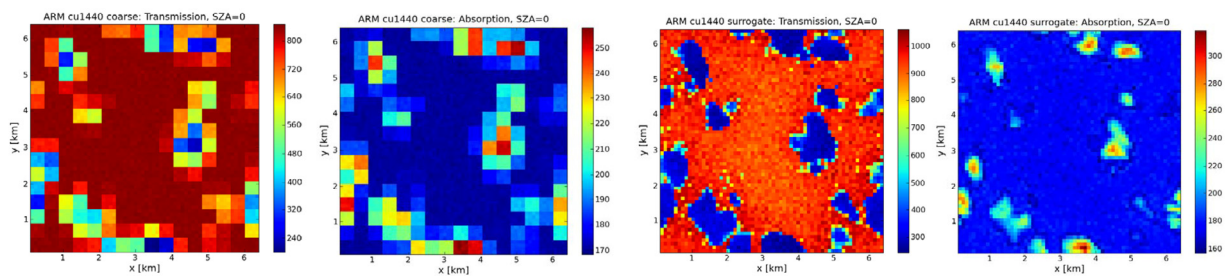


Fig. 3-19: The panels represent (from left to right) the spatially resolved IPA transmission through the coarse cumulus cloud labelled 'cu1440', the corresponding IPA absorption field within the embedding atmosphere (up to 30 km), the 3D transmission through the generated cumulus cloud with subscale variability added and the corresponding 3D absorption.

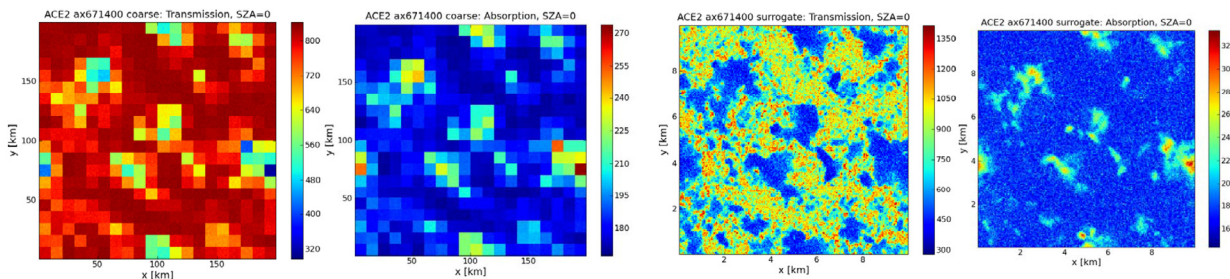


Fig. 3-20: Same as fig. 3-19 but for the coarse stratocumulus cloud labelled 'ax671400'.

Fig. 3-19 and fig. 3-20 display the spatially resolved transmission and absorption fields within the cumulus 'cu1440' and the stratocumulus 'ax671400' scenes, respectively. The results on the left refer to the CRM and those on the right to the exact case. The higher transmission maximum values for the fine clouds are obvious. These maxima happen to be near cloud edges and can be explained as an enhancement due to scattered photons in cloud free regions which are reflected at the cloud side and photons inside the cloud which leave the cloud through the side after scattering.

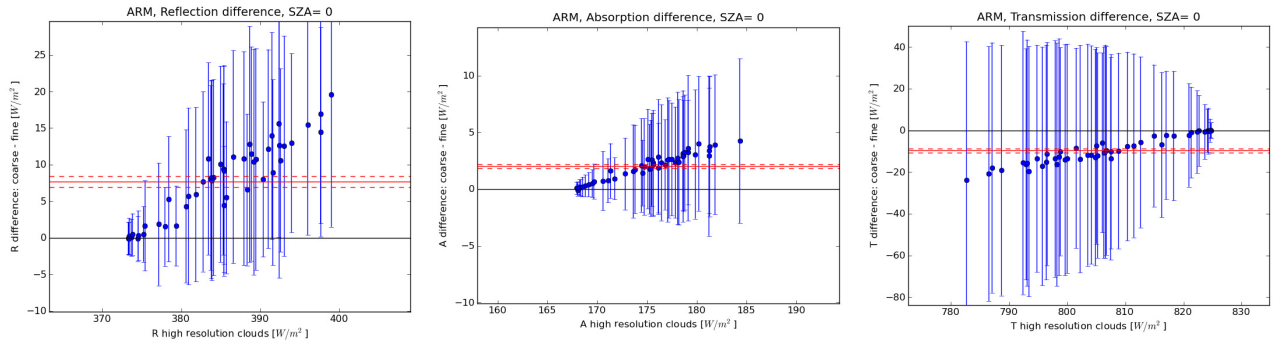


Fig. 3-21: The panels represent (from left to right) the difference of the reflection, absorption and transmission corresponding to the coarse and the fine cumulus clouds. Each point represents the mean value over the whole domain of the 51 distinct cloud scenes, whereas the error bars represent the error of the mean. Further details see text.

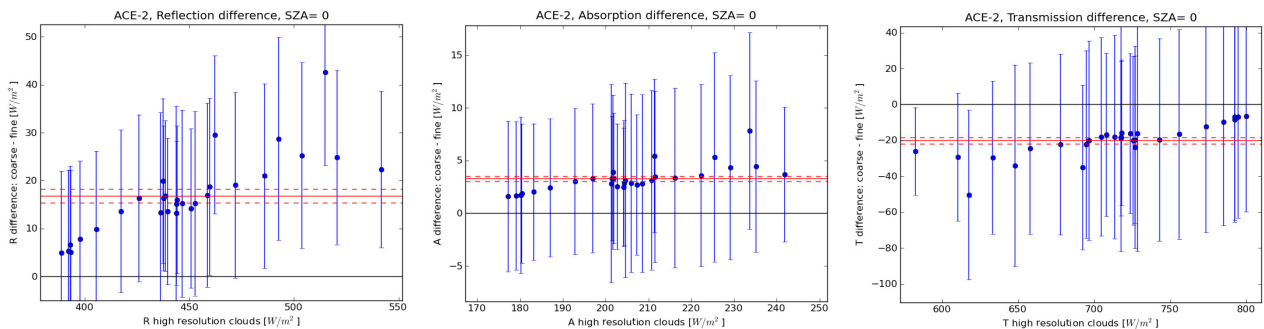


Fig. 3-22: Same as fig. 3-21 but for the stratocumulus clouds (29 distinct cloud scenes).

Fig. 3-21 and fig. 3-22 illustrate the differences between CRM and exact simulations for the cumuli and the stratocumuli, respectively. As the quantities of interest in CRM's are frequently domain averaged fluxes or heating rates, we decided to compare the domain averaged albedo (left), domain averaged absorption (middle) and domain averaged transmission (right). The blue points represent the differences of the domain averages of all cloudy scenes (51 in case of the cumuli and 29 in case of the stratocumuli) and the error bars the errors of the means. The solid red line indicates the mean difference of the domain averages averaged over all cloud scenes and the dashed red lines the error of this mean. The results demonstrate that the CRM calculations are biased: they produce higher albedo, higher absorption and lower transmission. The magnitude of this bias is of the order of tens of W/m^2 . Therefore the treatment of clouds in climate and weather prediction models (CRM's) is one of the main sources of uncertainties, comparable or bigger than, for instance, the popular CO_2 -doubling.

References

Brown, A.R., R.T. Cederwall, A. Chlond, P.G. Duynkerke, J.C. Golaz, M. Khairoutdinov, D.C. Lewellen, A.P. Lock, M.K. MacVean, C.H. Moeng, R.A.J. Neggers, A.P. Siebesma, and B. Stevens: Large-eddy simulation of the diurnal cycle of shallow cumulus convection over land, Q. J. R. Meteorol. Soc., 128 (582), 1075-1093, 2002

Chosson, F., J.-L. Brenguier, and L. Schüller: Entrainment-mixing and radiative Transfer Simulation in Boundary-Layer Clouds, J. Atmos. Res., 64 (7), 2670-2682, 2007

Fu, Q., and K.N. Liou: On the correlated k-distribution method for radiative transfer in nonhomogeneous atmospheres, J. Atmos. Sci., 49, 2139-2156, 1992

Gimeno García, S. and T. Trautmann: Radiative transfer modeling in inhomogeneous clouds by means of the Monte Carlo method. *Wissenschaftliche Mitteilungen aus dem Institut für Meteorologie der Universität Leipzig*, 30, Meteorological Institute of Leipzig University, Germany, ISBN 3-9808822-0-9, 2003

Henderson-Sellers, A. and M.F. Wilson: Surface albedo data for climatic modeling, *Reviews of Geophysics*, 21 (8), 1983

Slingo, A.: A GCM Parameterization for the Shortwave Radiative Properties of Water Clouds, *J. Atmos. Sci.*, 46 (10), 1419-1427, 1989

Venema, V., S. Gimeno García, C. Simmer: A new algorithm for the downscaling of 3-dimensional cloud fields, (*In print*), 2009

3.11 PIRATES, the Programmer's Interface to Radiative Transfer Algorithms

C.H. Köhler

Over the last years our department has gained a high level of expertise in radiative transfer solutions and inversion algorithms leading to the development of several radiative transfer models. However it is not only hard to determine which model to choose for a given problem, but even more difficult to adapt an existing model to a new problem if required. This is due to the fact that the models are often poorly documented and very few of them make use of object oriented design, which generally improves the re-usability of software. When a fast and accurate radiative transfer forward model was needed but no suitable solution was available because of the reasons outlined above, it was decided to implement many of the existing algorithms into a new project, with the intention to create an (advanced) Programmer's Interface to Radiative Transfer algorithms (PIRATES²). PIRATES is designed to meet the following requirements:

- modular design to keep modifications simple
- thorough documentation
- shared memory parallel processing capabilities
- re-usability of implemented routines

The whole project is currently realized as a dynamically linked library containing the essential modules such as atmosphere definitions, gas absorption processors or solvers of the radiative transfer equation. Additionally an ensemble of tools exists, which allow for simple modification and manipulation of model parameters, e.g. the incorporation of a temperature, pressure or relative humidity profile (as measured by a radiosonde) into an existing atmosphere or the convolution of output radiances with an instrument function.

In order to allow for a modular intrinsically thread-safe design, PIRATES is written in (object oriented) C++. Additionally existing algorithms already implemented in FORTRAN were incorporated into PIRATES whenever possible, since it is both cumbersome and error-prone to re-write existing software, which has already proven its reliability. All input and output operations are performed using the open source Hierarchical Data Format HDF5, which provides efficient ways to read write and store large amounts of data. Furthermore HDF5 includes interfaces to all major programming languages, which should simplify the passing of data among different users. The documentation is generated with the *Doxygen* software package which is widely used and accepted and which allows for a simple and yet effective documentation of the source code, including html and LaTeX code. A schematic overview of PIRATES is displayed in fig. 3-23.

Two groups of individual classes within the PIRATES library can be identified in fig. 3-23: Processors perform the elaborate and time consuming numerical calculations, such as evaluation and addition of spectral absorption lines or the numerical solution of the radiative transfer equation. All processors are capable of running multi-threaded with a variable number of threads, thus taking full advantage of modern multi-processor architectures. Storage classes are used to store, access and manage data acting either as input or output to the processors. An example for a storage object is an atmosphere, which stores for a number of user-defined levels temperature, pressure, relative humidity and gas concentration profiles, as well as aerosol concentration and size distribution parameters. Another example is a radiation field, which stores the radiance and integrated fluxes for each atmospheric level on an user defined wavenumber grid. Dotted lines indicate features which have yet to be implemented

² PIRATES is not only an abbreviation but also describes the author's tendency to "commandeer" existing algorithms and software and re-implement them into PIRATES

into the forward model. One of those is the scattering database developed by *J. Wauer and C. Schmidt* (see previous annual reports), which shall allow a direct lookup of particle scattering properties for user defined aerosols. This new feature is planned to be implemented in January 2010.

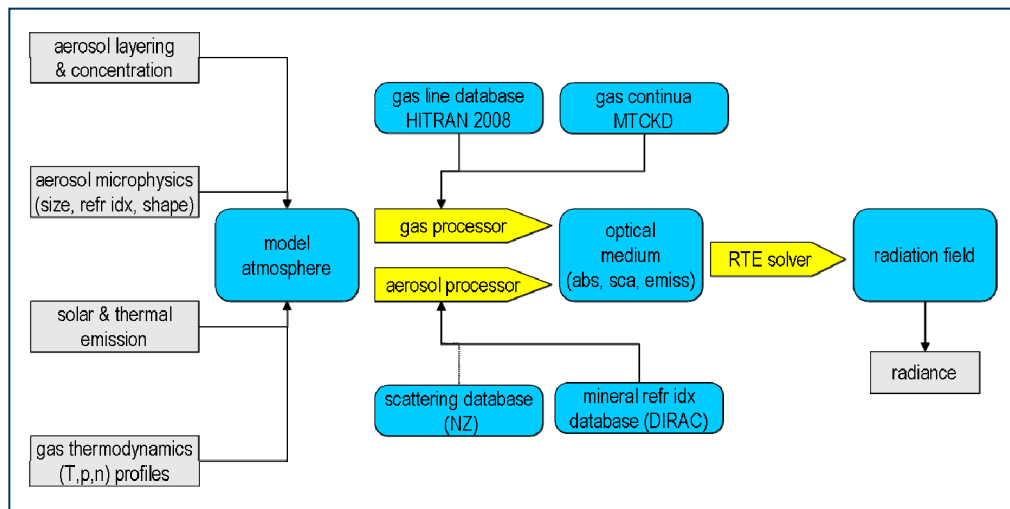


Fig. 3-23: A schematic overview of PIRATES components: Blue boxes indicate data-storage objects and yellow boxes indicate processor objects. Grey boxes symbolize physical quantities serving as input to, or output by, PIRATES.

As described above, modularity is a key design feature of PIRATES. Assume for example a user desires to exchange the current RTE solver, which is a slightly modified version of DISORT, against a faster two-stream model or a solver of the Schwarzschild equation. In this case it should be straightforward to derive a new class from the RTE solver base-class and just implement the algorithm needed for the new solver. All input, output and parallelization routines are provided by the base class and do not need to be implemented again.

So far the model has been validated against some high spectral resolution FTIR measurements and against FASCOD3 in the thermal infrared domain. More validations are planned for the future. In the long term view it is hoped that PIRATES will grow thus becoming a useful tool for the radiative transfer community. In this case it will be actively maintained by IMF-AP.

3.12 Multiple Scattering of Scalar Waves on an Ensemble of Non-penetrable Particles

K. Schmidt

Multiple scattering of waves on particle systems plays an important role in many fields of science and technology. Corresponding algorithms cannot only be applied to describe the scattering on ensembles but also on single complex and composed objects. The basic equations to be solved are the multiple scattering equations. Within a generalization of the self-consistent Green function formalism for acoustic and light scattering on single particles, developed by *Rother (2005a, 2005b, 2006, 2007)*, they read as follows.

$$\vec{W}_i = \vec{T}_i^t + \vec{T}_i^t \sum_{j=1, j \neq i}^N \vec{S}_1^t(a_i - a_j) \cdot \vec{W}_j \cdot \vec{S}_2^*(a_i - a_j)$$

Here, \vec{W}_i denotes the matrix belonging to the interaction operator of the i th particle, $i = 1, \dots, N$. \vec{T}_i^t designates the transpose of the T-matrix \vec{T}_i of the i th isolated particle. All T-matrices have to be computed in advance with respect to an arbitrarily chosen local coordinate systems within the particles. The matrices \vec{S}_1 and \vec{S}_2 are transformation matrices of the normalized spherical wave functions from one coordinate system into another (see e.g. *Martin 2006*). Their arguments (a_i, a_j) are vectors pointing from the origin of a global coordinate system outside the particles at the origins of the local coordinate systems within the i th and j th particle, respectively. The matrices \vec{S}_1 and \vec{S}_2 contain sums over products of spherical wave functions and the so-called 'Gaunt' coefficients. Note that the Gaunt coefficients are related to the Clebsch-Gordan coefficients as well as to the Wigner 3j symbols (see e.g. *Xu 1996, Mishchenko, Travis, and Lacis 2002, Martin 2006*). Thus, a numerical implementation of the multiple scattering equations requires efficient algorithms for computing these coefficients and the spherical wave functions, beside those for the T-matrices.

The former task has been realized by coding the fast algorithm of *Xu (1996)*. Several investigations have then been performed to test the corresponding routine. They include the reproduction of known values from the literature, the computation of Clebsch-Gordan coefficients on the basis of the Gaunt coefficients and comparing them with other results, the verification of the fulfilment of certain symmetries, and the verification of the fulfilment of the corresponding linearization formula for the spherical harmonics (see e.g. *Martin 2006*).

The crucial part in computing spherical wave functions is the determination of spherical Bessel functions. Here, the algorithm proposed by *Wang and van de Hulst (1991)* has been implemented. It is based on upward and downward recurrences for ratios of spherical Bessel functions, and has been proven to yield stable and accurate results for size parameters up to 50000, at least. This is demonstrated in fig. 3-24. It has been generated by using our Mie program for spherical scatterers after incorporating the above mentioned Bessel routines.

Certain symmetry properties of the Gaunt coefficients lead to corresponding symmetry relations for the transformation matrices \vec{S}_1 and \vec{S}_2 (*Martin 2006*). Their fulfilment has been used to test the routines for \vec{S}_1 and \vec{S}_2 . Additionally, the reproduction of special values and the fulfilment of the addition theorems for the spherical wave functions confirmed their reliability. In the next step, we will tackle the problem of simulating the multiple scattering on particle ensembles.

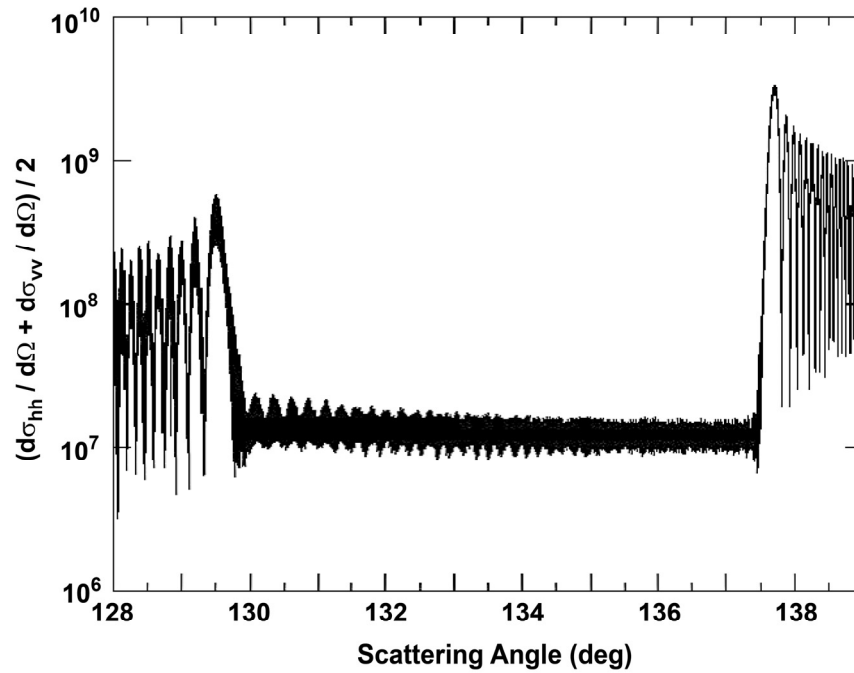


Fig. 3-24: Total scattered intensity of a water sphere having a radius of 5 mm and a complex refractive index of (1.331,-1.3e-8) at a plane wave incidence with a wavelength of 0.65 μm (size parameter of about 48332.2) in the rainbow region. The primary rainbow is seen at an angle of about 137.5° and the secondary rainbow lies at about 129.5°. Between both, Alexander's dark band can be observed.

References

Martin, P.A.: Multiple Scattering – Interaction of Time-Harmonic Waves with N Obstacles, Cambridge University Press, Cambridge, 2006

Mishchenko, M.I., Travis, L.D., and Lacis, A.A.: Scattering, Absorption, and Emission of Light by Small Particles, Cambridge University Press, Cambridge, 2002

Rother, T.: Self-consistent Green's function formalism for acoustic and light scattering, Part 1: Scalar notation, *Opt. Commun.*, 251, 254-269, 2005(a)

Rother, T.: Self consistent Green's function formalism for acoustic and light scattering, Part 2: Dyadic notation, *Opt. Commun.*, 251, 270-285, 2005(b)

Rother, T.: Self-consistent Green's function formalism for acoustic and light scattering, Part 3: Unitarity and Symmetry, *Opt. Commun.*, 266, 380-389, 2006

Rother, T.: Scalar Green's function for penetrable or dielectric scatterers, *Opt. Commun.*, 274, 15-22, 2007

Wang, R.T., and van de Hulst, H.C.: Rainbows: Mie computations and the Airy approximation, *Appl. Opt.* 30, 106-117, 1991

Xu, Y.-L.: Fast evaluation of the Gaunt coefficients, *Math. Comp.* 65, 1601-1612, 1996

3.13 Iterative T-Matrix Approach for Spheres with an Impressed Surface Irregularity

T. Rother, J. Wauer

In a former paper (see *Rother et al. 2006*) we could demonstrate that higher-order Chebyshev particles are appropriate to estimate the effect of a weak surface roughness in the resonance region. 'Weak' in this context means that the roughness is considered as a small perturbation of the underlying smooth geometry. Although the Chebyshev geometry is more likely to show a higher degree of regularity than actual rough surfaces, it was indeed possible to obtain satisfactory results.

For the numerical computations, we have used our T-matrix approach. However, the calculations have been restricted to lower size parameters, so far. This restriction is caused by the appearance of an ill-conditioned matrix which must be inverted in the T-matrix approach. To overcome this problem we started to consider an iterative T-matrix scheme which is closely related to a Lippmann-Schwinger equation. It was an essential goal of our effort in 2009 to apply this iteration procedure to the scalar scattering problem of ideal metallic and dielectric spheres to estimate the range of applicability with respect to the size parameter and the degree of roughness as well as to establish appropriate convergence criteria. The results we obtained recently look very promising.

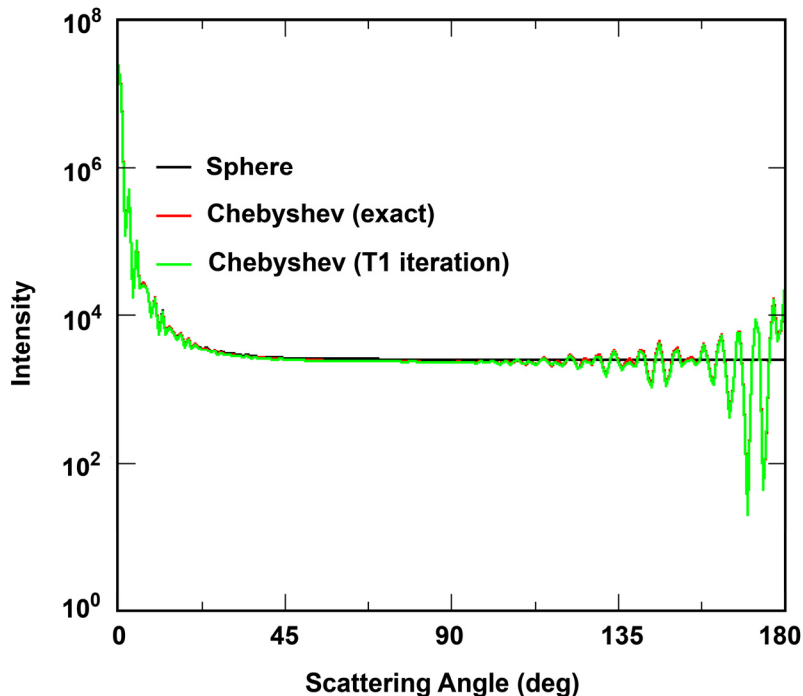


Fig. 3-25: Ideal metallic sphere versus Chebyshev particle (order: 151, deformation parameter: 0.003) at a size parameter of $ka=100$.

In fig. 3-25 and fig. 3-26 the results for an ideal metallic sphere at a size parameter of $ka=100$ (with 'k' and 'a' being the free-space wave number and the radius of the sphere) and for a dielectric sphere at a size parameter of $ka=50$ are presented. The impressed surface irregularity in both examples is given by a Chebyshev polynomial of higher order. Both figures illustrate the scattering behaviour of the underlying smooth sphere, the result of the sphere with an impressed surface roughness obtained by use of the rigorous T-matrix approach, and the result of the iteration scheme obtained by use of a first order iteration. The latter requires only an inversion of the matrix related to the smooth sphere. This can be done analytically. Obviously, the result of the first order iteration agrees very well with the result of the rigorous T-matrix approach. It becomes also obvious that there are essential differences in the scattering behaviour of the smooth sphere and the sphere with an impressed surface irregularity especially in the backward direction. We are looking forward to apply the derived iteration scheme successfully also at higher size parameters where the rigorous T-matrix approach begins to fail.

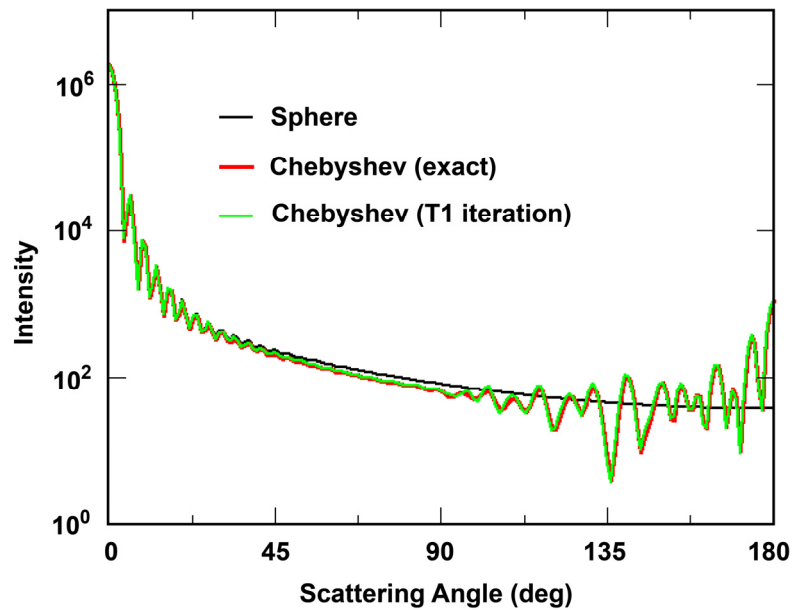


Fig. 3-26: Dielectric sphere ($n=1.4717+i\ 0.389$) versus Chebyshev particle (order: 75, deformation parameter: 0.008) at a size parameter of $ka=50$.

To estimate the reliability of the results obtained we proved the reciprocity condition in the far-field. We could show that this condition is an appropriate convergence criterion.

The proposed iteration scheme has two essential advantages if compared to approaches used so far in the context of surface roughness. Firstly, it can be numerically adopted without any problems by any existing T-matrix approach. Secondly, the analytical invertibility of the matrix related to rough spheres seems to permit application of the 'complex angular momentum' method developed by *Nussenzweig* (1965) for very high size parameters

References:

Rother, T., Schmidt, K., Wauer, J., Scherbakov, V. and Gayet, J.-F.: Light scattering on Chebyshev particles of higher order, *Applied Optics* 45, 6030-6037, 2006

Nussenzweig, H.M.: High-Frequency Scattering by an Impenetrable Sphere, *Annals of Physics*, 34, 23-95, 1965

4. Atmospheric Remote Sensing – Applications

4.1 Total Ozone Trends from the 14-Years GOME/SCIAMACHY/GOME-2 Data Record

D. Loyola, M. Coldewey-Egbers, W. Zimmer, M. Koukoulis (Aristotle University Thessaloniki), D. Balis (Aristotle University Thessaloniki), C. Lerot (BIRA-IASB), M. Van Roozendaal (BIRA-IASB), M. Dameris (DLR-PA)

The stratospheric ozone layer is affected by a variety of factors including natural fluctuations as well as the emission of ozone depleting substances. Although the Montreal Protocol now controls the production and release of those substances, the time scale of ozone recovery is still unclear. Space-borne atmospheric remote sensing is a valuable tool for monitoring the evolution of the stratospheric ozone layer. Therefore, in the past year, we merged the total ozone columns from three European satellite sensors – GOME, SCIAMACHY and GOME-2 – into a long-term ozone data record starting in 1995. Global ozone trends were then derived by applying statistical methods.

Total Ozone datasets

Fourteen years, covering the period from June 1995 to April 2009, of monthly means of total ozone columns from three different data sources were used in this study. They formed two homogenized global data records: one from the European satellite sensors GOME/ERS-2, SCIAMACHY/ENVISAT, and GOME-2/MetOp-A (see *Loyola et al. 2009*) labelled 'GOME' dataset and another one from a combination of TOMS, SBUV(2), and OMI measurements (see *Stolarski and Frith 2006*), referred to as 'TOMS' dataset. Corresponding measurements from over 70 globally distributed Dobson and Brewer ground stations served as reference. This well-established network covers a wide geographical extent and has often been used for both validations of satellite data as well as trend studies (*Balis et al. 2007*). Fig. 4-1 displays how both space-borne datasets relate to the ground based time series. The ratioed data exhibit a distinct seasonal cycle within $\pm 5\%$, and a slight positive drift of about $+1.2\%$ per decade for the GOME data with respect to ground data and $+1.9\%$ per decade for the TOMS data, respectively.

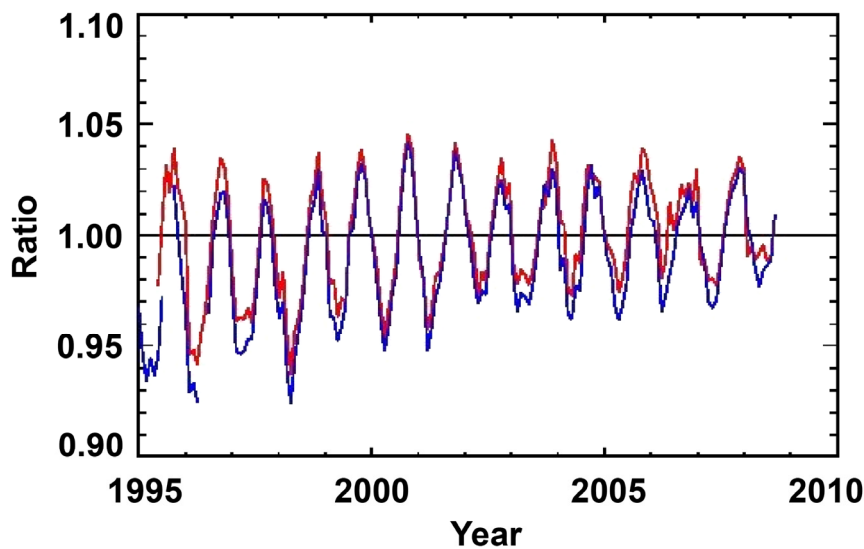


Fig. 4-1: Ratio of the GOME dataset to ground-based monthly ozone data averaged from 60°N - 60°S (red). In blue the equivalent TOMS data is given.

Merged GOME total ozone

From products based on the GDP 4.x algorithm (*Valks and Loyola 2009, Lerot et al. 2009, Van Roozendaal et al. 2006*) we computed monthly means for the single GOME, SCIAMACHY and GOME-2 total ozone measurements as area-weighted averages of daily composites on a grid of $0.33^{\circ} \times 0.33^{\circ}$. For analyses with a coarser spatial resolution also data on grids of $1^{\circ} \times 1^{\circ}$ and $5^{\circ} \times 5^{\circ}$ were generated together with 1° zonal averages and the entire 60°N - 60°S average. Table 4-1 provides the composition of this dataset.

Since the GOME data record is very stable we used it as a standard and adjusted SCIAMACHY and GOME-2 data in periods of instrument overlap. Thus a homogeneous long-time series was established. The adjustment applied to SCIAMACHY comprised two parts: a basic latitudinal correction for each month of the year averaged from 2002 to 2009, and a time-dependent offset for each individual month, which accounts for the slight decreasing drift ($< 0.5\%$ per year) found in the SCIAMACHY SGP v3.01 ozone columns compared to GOME (Lerot et al. 2009). On average GOME-2 ozone columns are 2-3% lower than GOME values. As their overlap period is limited to 28 months from January 2007 to April 2009, the adjustment applied to GOME-2 is a latitude dependent correction factor for each single month. In case of instrument overlap periods, data are averaged weighted by the number of available observations. Due to the GOME tape recorder failure and the consequent loss of global coverage, no GOME data were used after June 2003.

Time period	Data / Instruments
06/1995 - 07/2002	GOME
08/2002 - 06/2003	GOME and SCIAMACHY
07/2003 - 12/2006	SCIAMACHY
01/2007 - 04/2009	SCIAMACHY and GOME-2

Table 4-1: Composition of the merged GOME/SCIAMACHY/GOME-2 total ozone dataset

Merged TOMS total ozone

NASA's Merged Ozone Data sets (MOD) are monthly-mean zonal (5°) and gridded ($5^\circ \times 10^\circ$) products constructed by merging individual TOMS, SBUV(2), and OMI V8 satellite measurements. An external calibration adjustment has been applied to each satellite dataset in an effort to calibrate all the instruments to a common standard. The Earth Probe TOMS calibration from launch through summer 1999 is used as a reference standard, and all the other instruments are adjusted externally to match that calibration. The data cover almost continuously the period from November 1978 to April 2009, see Stolarski and Frith (2006) for more details.

Trend analysis

We used a linear statistical model similar to that from Vyushin et al. (2007) for describing observations of monthly mean total ozone data. It is expressed as

$$\Omega(t) = \mu + A(t) + T(t) + Q(t) + S(t) + N(t)$$

where $\Omega(t)$ denotes total ozone, t is the number of months after June 1995, μ is the overall mean, $A(t)$ represents the seasonal cycle, $T(t)$ the linear long-term trend, $Q(t)$ the quasi-biennial oscillation (QBO), $S(t)$ the solar cycle, and $N(t)$ are the residuals (noise). The unknown coefficients of the model are identified by multi-linear regression on the total ozone observations using a least squares method. For the unexplained portion of the data the noise $N(t)$ is assumed to be autoregressive of the order of 1, i.e. $N(t) = \phi N(t-1) + \alpha(t)$, where $\alpha(t)$ are independent, normally distributed random errors. A Cochrane-Orcutt transformation 0 is applied to the regression equation using an estimate of the auto-correlation coefficient ϕ with time lag of one month in order to ensure that the remaining residuals fulfil this assumption. The fit uncertainty σ is the variance of the noise $N(t)$. Sine and Cosine terms in $A(t)$, $Q(t)$, and $S(t)$ account for their seasonal dependence. The QBO signal is represented using winds at both 30 and 50 hPa. $S(t)$ is the solar flux measured at a wavelength of 10.7 cm. The starting point of our analysis is June 1995 which is very close to the expected turning point and beginning of recovery of total ozone. Therefore we decided to use at first a simple linear trend model instead of a piecewise linear trend.

Fig. 4-2 provides an example of fitting the merged GOME 60°N-60°S time series from June 1995 to April 2009. The estimated linear trend is 0.44% ($\pm 0.6\%$) per decade. The coefficient of multiple determination R^2 is equal to 0.963, indicating that the selected proxies represent about 96% of the variability in the ozone data. The auto-correlation coefficient with time lag of one month of the residual using the transformed model is 0.03, whereas it is 0.56 without transformation.

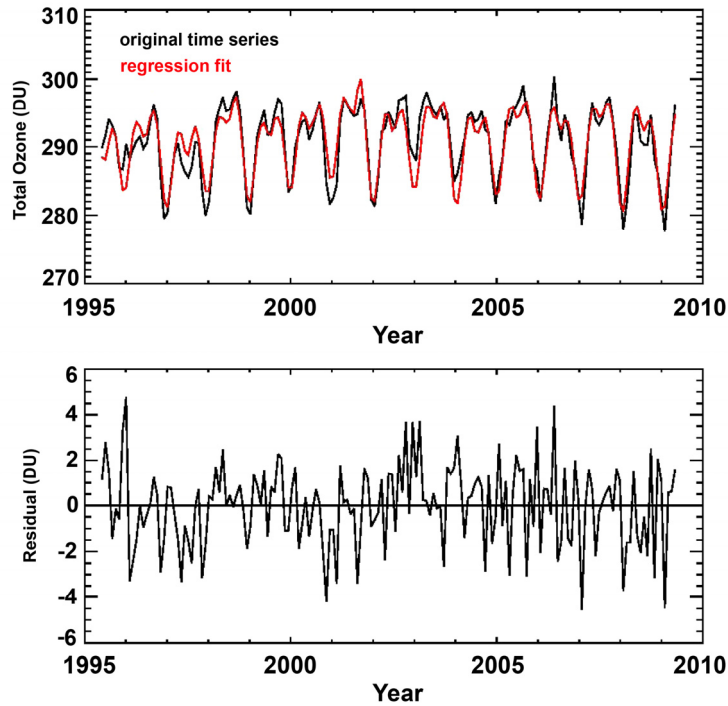


Fig. 4-2: Example of fitting the merged GOME/SCIAMACHY/GOME-2 60°N-60°S time series (top panel) and the remaining residuals (bottom panel).

Global Trends

Fig. 4-3 illustrates linear global (5° × 5°) total ozone trends from June 1995 to April 2009 for the GOME/SCIAMACHY/GOME-2 and the TOMS/SBUV(2)/OMI datasets, respectively. In general the patterns of both regressions are very similar. Significant positive trends appear in the tropics and in the northern hemisphere over Europe and Canada. The negative trend in the ocean region south from Africa is more marked in the merged GOME than in the merged TOMS results. In the same way the positive trends in the northern part of South America, India and Indonesia are more prominent in the merged GOME than in the merged TOMS results.

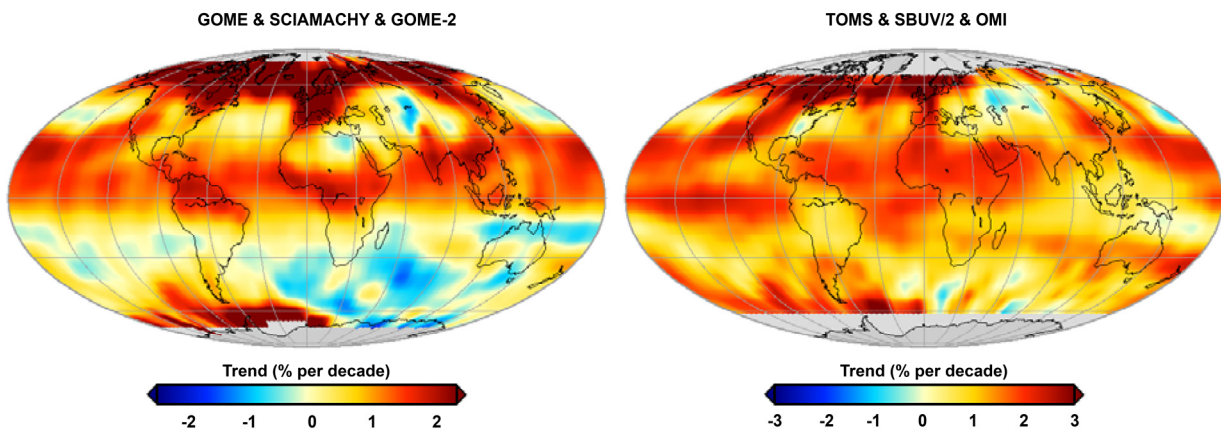


Fig. 4-3: Global total ozone trend in % per decade for GOME/SCIAMACHY/GOME-2 (left) and TOMS/SBUV/OMI (right)

Fig. 4-4 shows the number of years required to detect a trend of 1% per decade in the merged GOME dataset following the approach of *Tio et al. (1990)*. The number of required 'measurement years'

increases with increasing fit uncertainty (σ) and increasing autocorrelation in the noise term $N(t)$ as introduced above.

The merged GOME dataset can already detect real trends at the level of 5% per decade from 60°N to 60°S with a 95% confidence level. The number of required measurement years increase considerable for detecting trends at the level of 1% per decade with a 95% confidence level. In the tropics 10 to around 20 years of GOME data are required, i.e. the merged GOME time series, which now completes 14 years, is already on the verge of it. In high latitudes more than 30 years of measurements are needed, whereas in the Polar Regions even more years of measurements are required. This is due to the polar night periods which reduce the effective periods with UV-VIS measurements considerably.

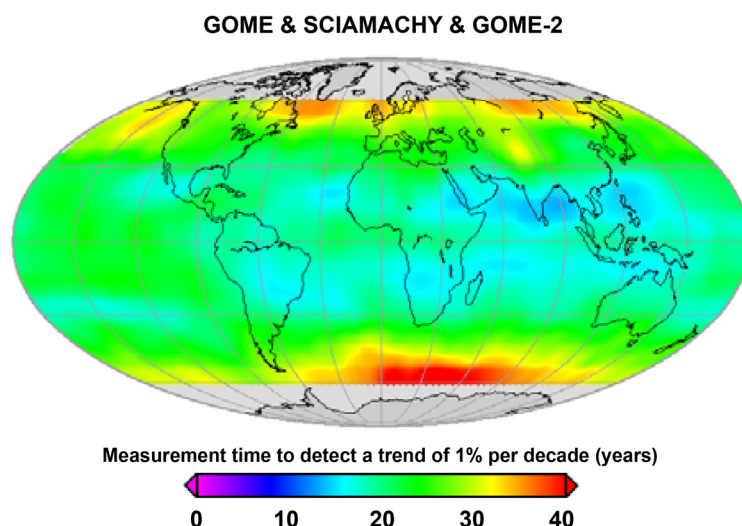


Fig. 4-4: Number of years required to detect a trend of 1% per decade with a 95% confidence level using the merged GOME dataset.

In summary a global slightly positive trend ($< 1\%$ per decade) in the total ozone since June 1995 from the merged GOME dataset was found, with marked positive and negative regional patterns. This trend agrees well with both an independent satellite dataset and ground-based measurements. Our statistical analysis showed that the amount of merged GOME data available already gives a 95% confidence level to detect a trend of the order of 1% per decade in the tropical region and a trend of the order of 5% from 60°N to 60°S. Additional years of measurements are needed to reach the same confidence level for high latitudes and even more for the Polar Regions.

References

- Balis, D., M. Kroon, M. Koukouli, E.J. Brinksma, G. Labow, J.P. Veefkind, R.D. McPeters: Validation of Ozone Monitoring Instrument total ozone column measurements using Brewer and Dobson spectrophotometer ground-based observations. *Journal of Geophysical Research*, 112, D24546, DOI:10.1029/2007JD008796, 2007
- Lerot, C., M. Van Roozendael, J. van Geffen, J. van Gent, C. Fayt, R. Spurr, G. Lichtenberg, and A. von Bargaen: Six years of total ozone column measurements from SCIAMACHY nadir observations. *Atmos. Meas. Tech.*, 2, 87-98, 2009
- Loyola, D., M. Coldewey-Egbers, M. Dameris, H. Garny, A. Stenke, M. Van Roozendael, C. Lerot, D. Balis, M. Koukouli: Global long-term monitoring of the ozone layer – a prerequisite for predictions. *International Journal of Remote Sensing*, 30, 15-16, 4295–4318, 2009
- Stolarski, R.S. and S.M. Frith: Search for evidence of trend slow-down in the long-term TOMS/SBUV total ozone data record: the importance of instrument drift uncertainty. *Atmos. Chem. Phys.*, 6, 4057-4065, 2006
- Tiao, G.C., G.C. Reinsel, D. Xu, J.H. Pedrick, X. Zhu, A.J. Miller, J.J. DeLuisi, C.L. Mateer, D.J. Wuebbles: Effects of autocorrelation and temporal sampling schemes on estimates of trend and spatial correlation. *Journal of Geophysical Research*, 95, 20507-20517, 1990

Valks, P., D. Loyola: Algorithm Theoretical Basis Document for GOME-2 Total Column Products of Ozone, Minor Trace Gases and Cloud Properties (GDP 4.2 for O3M-SAF OTO and NTO). DLR/GOME-2/ATBD/01, Iss./Rev.: 2/A, January 2009

Van Roozendaal, M., D. Loyola, R. Spurr, D. Balis, J.C. Lambert, Y. Livschitz, P. Valks, T. Ruppert, P. Kenter, C. Fayt, and C. Zehner: Ten years of GOME/ERS-2 total ozone data. The new GOME data processor (GDP) version 4: 1. Algorithm description. Journal of Geophysical Research, 111 Doi:10.1029/2005JD006375, 2006

Vyushin, D.I., V.E. Fioletov, T.G. Sheperd: Impact of long-range correlations on trend detection in total ozone. Journal of Geophysical Research, 112, D14307, DOI:10.1029/2006JD008168, 2007

4.2 Air Quality Measurements During the Beijing Olympic Games with GOME-2

N. Hao, P. Valks, M. Rix (TUM), D. Loyola, W. Zimmer, S. Emmadi (TUM)

Beijing is one of the world's largest mega-cities with more than 17 million residents and more than 3 million vehicles. The dense traffic, construction, industry, coal-fired power plants and city's geography result in severe air pollution in Beijing. To improve the air quality during the Beijing Olympic Games in August 2008, systematic long- and short-term measures were implemented before and during the Olympic Games. These included strict vehicular emissions standards, removing half of the cars from the road (about 1.5 million) through an odd/even plate number rule from July 20 to September 20, closing or relocating pollution emitting factories and freezing construction activities. Since surrounding areas contribute significantly to Beijing's air pollution, emission controls on large industrial sources were also applied in surrounding provinces such as Hebei, Shanxi, Shandong and Tjian city. At IMF-AP, we have assessed the effectiveness of these controls and studied the impact on pollutants over Beijing and neighboring provinces during the Olympic Games using operational GOME-2 tropospheric NO₂, SO₂ and formaldehyde measurements, as processed by DLR in the framework of the O3M-SAF.

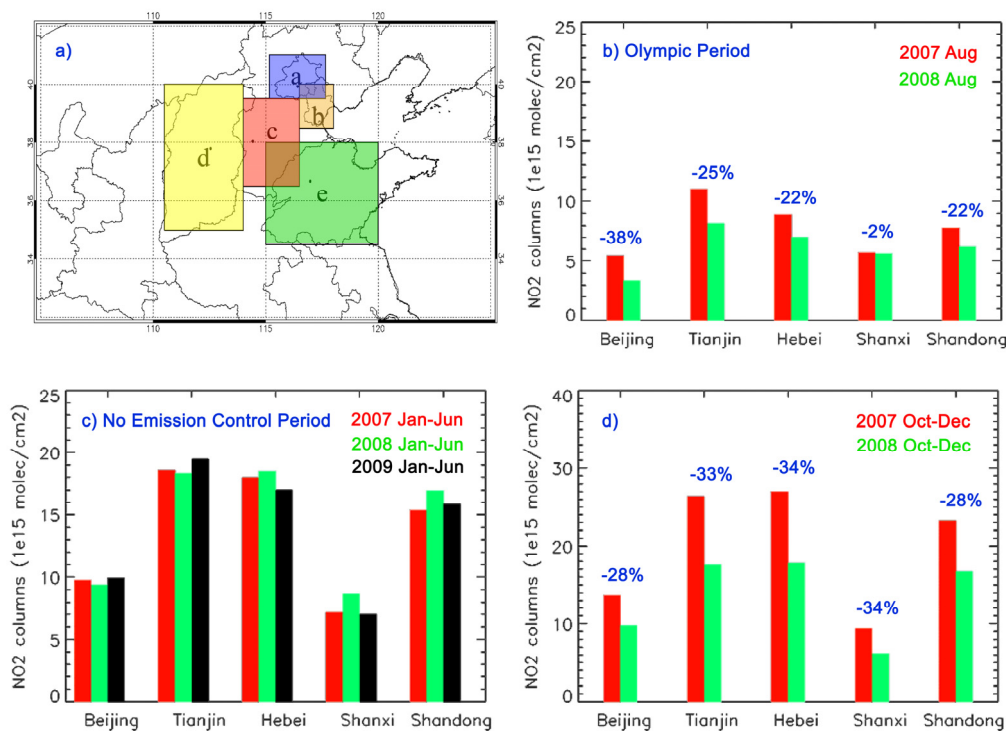


Fig. 4-5: Results of NO₂ monitoring. Monitored regions are given in a) with Beijing (blue), Tianjing (orange), Hebei (red), Shanxi (yellow) and Shandong (green). GOME-2 tropospheric NO₂ column concentrations over Beijing and surrounding areas in during the Olympic Games (b) and during periods without emission control (c, d).

First, we compared GOME-2 tropospheric NO₂ columns over Beijing and surrounding provinces between the Olympic period (August, 2008) and the same period in 2007.

Fig. 4-5 shows that tropospheric NO₂ has decreased by about 38%, 25%, 22%, 2% and 22% over Beijing, Tianjin, Hebei, Shanxi and Shandong respectively during the Olympic period, compared to the same period in the previous year. Furthermore, we compared GOME-2 tropospheric NO₂ for the period January-June 2008 when no emission control measures were applied, with the same period in 2007 and 2009. As shown in fig. 4-5c, there is no clear decrease of NO₂ over Beijing and surrounding areas during this period before the Olympic Games, compared to 2007 and 2009. These results indicate that the emission control measures played an important role in the NO₂ reduction during the Olympic period. Here, it is important to note that besides the emission reductions, the meteorological conditions have a large effect on the NO₂ concentrations as well. *Mijling et al. (2009)* and *Wang et al. (2009a)* have used chemistry transport models to separate the effect of the emission control measures and the meteorological conditions on the NO₂ concentrations. Their model analysis illustrates that the reductions of NO₂ during the Olympic period were mainly an effect of the emission control measures over Beijing and surrounding areas, while the favorable meteorological conditions played a minor role. To analyze the NO₂ pollution after the Olympic Games, we compared GOME-2 tropospheric NO₂ for October - December 2008 with the same period in 2007. Fig. 4-5d indicates that for all areas, the satellite observed over 20% less NO₂ during this post Olympic period (compared to 2007). Similar decreases in the PM₁₀ concentrations in Beijing were reported by *Wang et al. (2009b)*. A possible reason is the down turn in the economy and energy production in China during the second half of 2008.

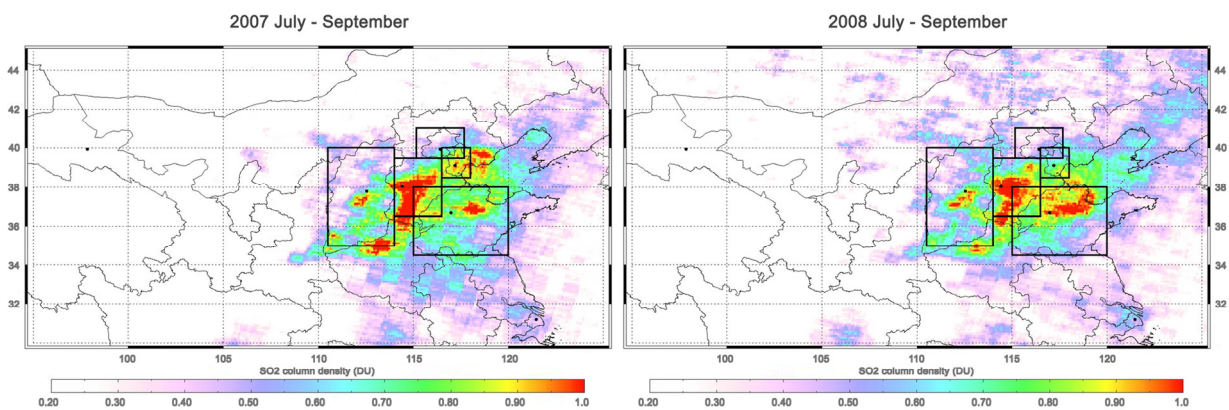


Fig. 4-6: GOME-2 SO₂ column densities for Beijing and surrounding areas in July - September 2007 and 2008.

The GOME-2 SO₂ column for Beijing and surrounding areas during the Olympic Games are shown in fig. 4-6. SO₂ is a short-lived gas primarily produced by volcanoes, power plants, refineries, metal smelting and burning of fossil fuels. It is obvious from fig. 4-6 that the SO₂ concentration over Beijing decreased to a lesser extent than the concentration of traffic related pollutants, such as NO₂ and CO. However, the SO₂ concentrations over East China are much larger in winter, than during the Olympic Games in summer. Therefore, we analyzed the SO₂ concentrations in the period January/February for the years 2007, 2008 and 2009 (fig. 4-7). From 2007 to 2009, a clear reduction of SO₂ is found for Beijing and the surrounding regions. This reduction is probably related to the installation of desulphurization equipment in coal-fired power station and boilers, and the shutting down of small coal-fired boilers, which started in 2007.

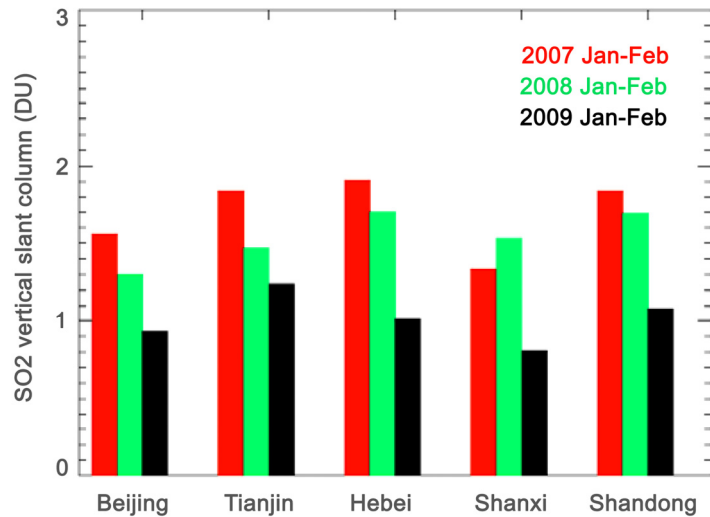


Fig. 4-7: GOME-2 SO₂ column densities in January/February for the years of 2007-2009 over Beijing and surrounding areas.

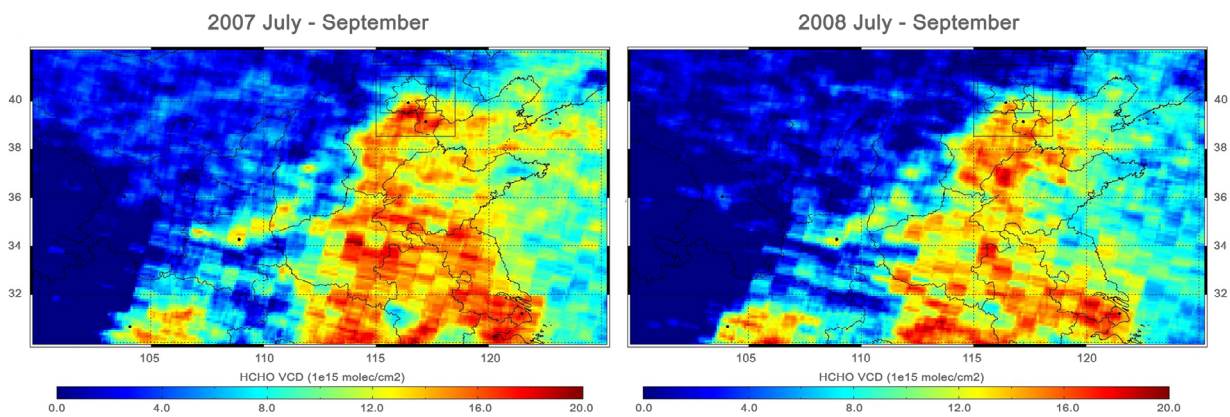


Fig. 4-8: GOME-2 HCHO column densities in July - September 2007 and 2008 over Beijing and surrounding areas.

Formaldehyde (HCHO) is a new operational GOME-2 product developed at IMF-AP in 2009 (see chapter 3-2). For the Olympic period, we found a reduction in HCHO over Beijing and Tianjin, compared to the same period in 2007 (fig. 4-8). This is most likely a consequence of emission control measures implemented on industrial and power plant facilities, since fossil fuel combustion is one of the main sources of HCHO, especially in East China.

References

Mijling, B., R.J. van der A, K.F. Boersma, M. Van Roozendaal, I. De Smedt, and H.M. Kelder: Reductions of NO₂ detected from space during the 2008 Beijing Olympic Games, *Geophys. Res. Lett.*, 36, L13801, doi:10.1029/2009GL038943, 2009

Wang Y., J. Hao, M.B. McElroy, J.W. Munger, H. Ma, D. Chen and C.P. Nielsen: Ozone air quality during the 2008 Beijing Olympics: effectiveness of emission restriction, *Atmos. Chem. Phys.*, 9, 5237-5251, 2009a

Wang W.T., T. Primbs, S. Tao and S.L.M. Simonich: Atmospheric Particulate Matter Pollution during the 2008 Olympics, *Environ. Sci. Technol.*, 43, 5314-5320, 2009b

4.3 Monitoring of Volcanic Sulfur Dioxide Emissions for Early Warning of Volcanic Hazards

M. Rix, P. Valks, D. Loyola, N. Hao, W. Zimmer, S. Emmadi (TUM)

Most of the world's potentially active volcanoes are not monitored on a regular basis, of the ones known to have erupted in historic times less than twenty-five percent have basic monitoring and little more than 20 volcanoes a well established monitoring network. Furthermore many of the most explosive eruptions since 1800 have occurred at volcanoes that had not shown any activity for several thousand years. The danger associated with volcanoes is not restricted to eruptions, further volcanic hazards are earthquakes, dangerous gases (e.g. Lake Nyos, Cameroon), flank movements and ground deformation, tsunamis, landslides and climatic changes (e.g. Mount Pinatubo, Philippines, 1991). Monitoring and forecasting of volcanic activity in combination with early warning of volcanic risk is therefore of major importance.

The project *Exupéry*, as part of the German GEOTECHNOLOGIEN program, aims at developing a mobile volcano fast response system. This is intended to support countries in case of volcano related disasters. The system is especially dedicated to supporting third world countries in dealing with volcanic risk. The *Exupéry* system (www.exupery-vfrs.de) is designed for operating standalone or as a supplement to an existing monitoring network providing additional information on volcanic activity parameters that are not routinely observed (see below). Using this additional information further insight into the volcanic processes is possible. Apart from traditional monitoring techniques like seismology, the system includes ground based observations of gas fluxes and surface deformation. One of the novelties of the system is the utilization of space-based observations, including monitoring of ground deformation, thermal anomalies and volcanic SO₂ emissions, based on GOME-2 measurements. All acquired data are stored in a central data base together with data from an existing monitoring network. Maps of total SO₂ columns are generated automatically. IMF-AP supplies them daily to the database together with additional information concerning the SO₂ measurements such as location and maximum SO₂ value observed. Threshold levels for the SO₂ are determined to yield special SO₂ alerts in case of high SO₂ amounts, indicating exceptional SO₂ degassing levels. The information is visualized in a GIS system. Data is supplied for the two volcanic test regions 'Azores' and 'Italy'. They are available in the GIS approximately 7 hours after sensing. The whole *Exupéry* prototype system was installed and tested at Fogo volcano on the Azores during summer 2009.

Further activities at IMF-AP included the implementation of the SO₂ retrieval algorithm into the operational GOME-2 O3M-SAF system at DLR. Corrections for the dependence on total ozone, the solar zenith angle and the temperature dependence of the SO₂ cross-sections are now routinely applied during the retrieval of SO₂ columns. The SO₂ column is retrieved for 3 different heights (2.5 km, 6 km, 15 km), as the AMF strongly depends on the plume height which is rarely available at the time of measurement. The three altitudes represent typical volcanic events: passive degassing of low volcanoes, moderate volcanic eruptions or passive degassing of high volcanoes and explosive eruptions.

During 2009 several volcanic eruptions have been detected by GOME-2 including major ones like the Mt. Redoubt eruption (Alaska) starting with five major explosions on 23 March and lasting until June 2009 and the eruption of Sarychev Peak (Kamchatka) in June 2009 (fig. 4-9). Both eruptions emitted high amounts of SO₂ into the atmosphere. An initial validation of the GOME-2 total SO₂ columns with ground-based observations and other satellite measurements has been carried out in 2009. SO₂ columns for an explosive volcanic eruption reaching stratospheric heights (Kasatochi, Alaska – see the annual report for 2008) and for an effusive eruption (Kilauea, Hawaii) were compared with results from SCIAMACHY and ground based Brewer spectrometer measurements. Comparisons for the volcanic SO₂ plumes from Kasatochi and Kilauea show that the two satellite instruments capture the structure of the SO₂ cloud very well: the locations of the peak SO₂ values and the dimensions of the SO₂ cloud match nicely (fig. 4-10). Differences in the observed total SO₂ columns can mostly be explained by differences in the retrieval methods for the two instruments. Brewer spectrometer measurements in Uccle and Manchester, that captured the enhanced SO₂ concentrations related to the overpass of the Kasatochi SO₂ cloud, match very well with the GOME-2 SO₂ measurements. Furthermore a comparison of SO₂ pollution measurements using a MAX-DOAS instrument in Beijing, operated by BIRA-IASB, with GOME-2 observations in that region has been carried out. The results of the MaxDOAS instrument display good

agreement with the SO₂ amounts observed by GOME-2. Both instruments show enhanced SO₂ values during the winter months (fig. 4-11).

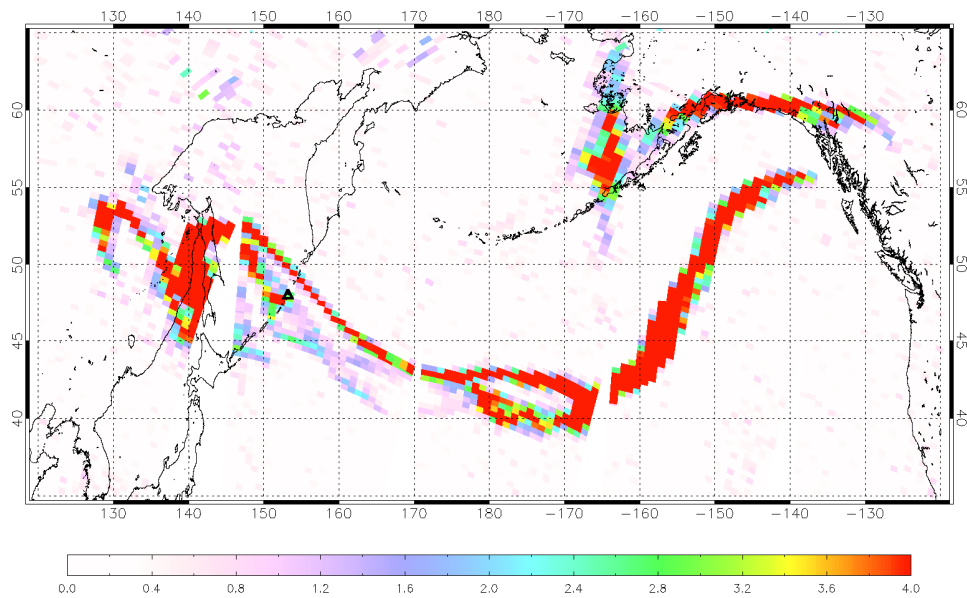


Fig. 4-9: SO₂ cloud from Sarychev Peak eruption (Kamchatka), detected by GOME-2 on 17th June 2009

The SO₂ columns retrieved at IMF-AP are used for several early warning services related to volcanic hazards, such as the Support to Aviation Control Service (SACS) which is part of the GMES (Global Monitoring for Environment and Security) Service Element for the Atmosphere (PROMOTE) and ESA/DUE project GlobVolcano, which aims at using satellite monitoring services to support volcanological observatories in their monitoring activities.

Further research activities focused on the determination of the correct plume height, as this is of major importance for the correct retrieval of the total SO₂ amount as well as for aviation safety. First tests have been carried out concerning the retrieval of the plume height from measured spectra. Using the SO₂ and O₃ results of the DOAS analysis as input parameters, spectra are simulated with the radiative transfer model RRS-LIDORT for different plume heights. They matched with the measured spectra. The plume height can then be determined using an iterative approach. First tests and comparisons with plume heights retrieved by trajectory matching provided promising results.

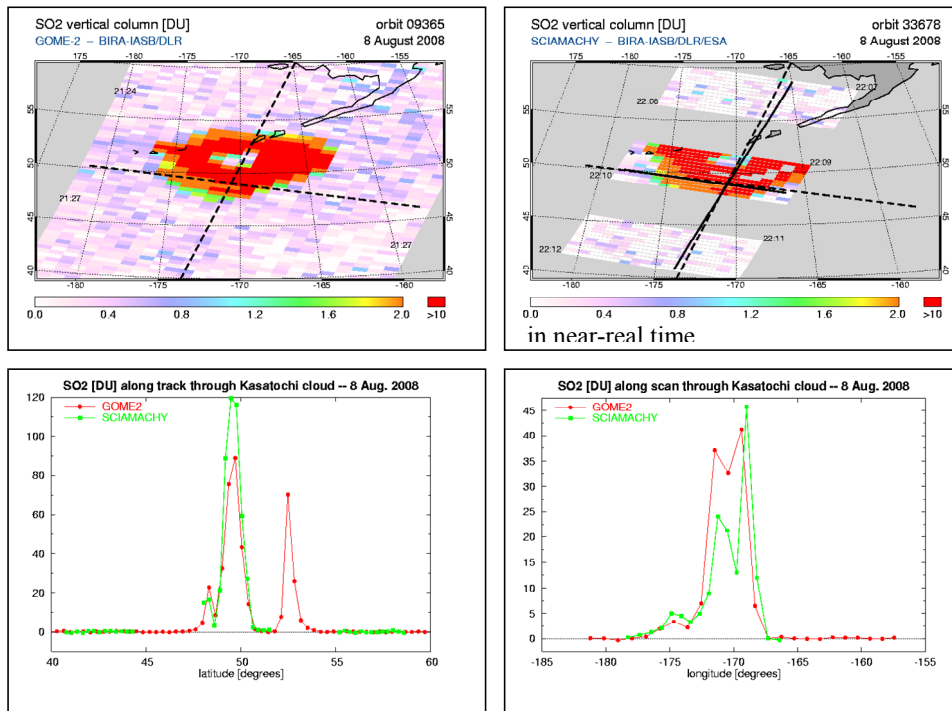


Fig. 4-10: Along-track and along-scan lines in the GOME-2 (dashed) and SCIAMACHY (solid) orbit used for a direct pixel-to-pixel comparison of data on 8 August 2008 (top) and comparison of the total SO₂ column (bottom). Differences in the observed total SO₂ columns can mostly be explained by differences in the retrieval methods for the two instruments. An interesting feature can be observed in the measurements. The erupted SO₂ was distributed into a circular pattern by atmospheric winds. The lack of SO₂ in the center is clearly visible in the along track observations.

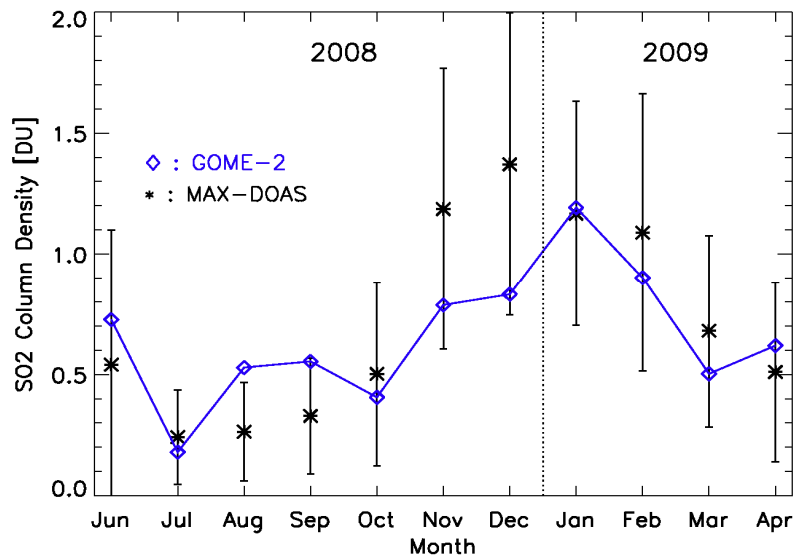


Fig. 4-11: Comparison of GOME-2 SO₂ column measurements with MAX-DOAS measurements in Beijing, China (39.9°N, 116.4°E)

4.4 SCIAMACHY and the Goddess of Love - Venus Observations from Earth Orbit

M. Gottwald, S. Slijkhuis, E. Krieg (TwIG), F. Schreier, G. Lichtenberg, M. Vasquez, R. Snel (SRON), D. Stam (SRON), R. de Kok (SRON)

SCIAMACHY spends most of its in-orbit activities with observing the Earth's atmosphere. Regularly two extraterrestrial objects – the Sun and the moon – complement the measurement schedule. Both celestial objects are observed when the spacecraft's orbital motion causes them rising above the Earth's limb. From the horizon up to an altitude of 100 km the occultation data provide vertical profiles of atmospheric parameters. Above the top of the atmosphere at 100 km the acquired data serve calibration & monitoring needs. SCIAMACHY's specification has always suggested that bright extraterrestrial sources, such as the bright planets, might also yield useful data. With having improved the Line-of-Sight (LoS) pointing knowledge significantly over the past years the challenge to steer SCIAMACHY's narrow Instantaneous Field of View (IFoV) onto pointlike extraterrestrial sources could indeed be tackled. Together with colleagues from SRON Netherlands Institute for Space Research we selected Venus as the first target to test SCIAMACHY's extraterrestrial 'capabilities'. This planet had already in 2008 been proposed by SRON as a target for characterizing the slit width in elevation. However Venus offers more. Our solar system neighbour is one of the terrestrial planets almost identical in size and mass. As the Earth it is embedded in a dense atmosphere, although completely different in composition. The high content of CO₂ sustains a greenhouse effect much larger than on Earth. It is obvious that Venus forms an excellent target for studying the atmosphere of planetary bodies.

Venus Visibility

Venus, the third brightest object in the sky, varies its apparent brightness between $m_{vis} = -3.8$ and -4.5 mag with its apparent diameter depending on the distance from Earth. At inferior conjunction (Venus passes between the Earth and the Sun) the minimum distance of 41×10^6 km leads to a diameter of 61" while at superior conjunction (Venus is just behind the Sun) Venus is 255×10^6 km away and only 10" wide (fig. 4-12 left).

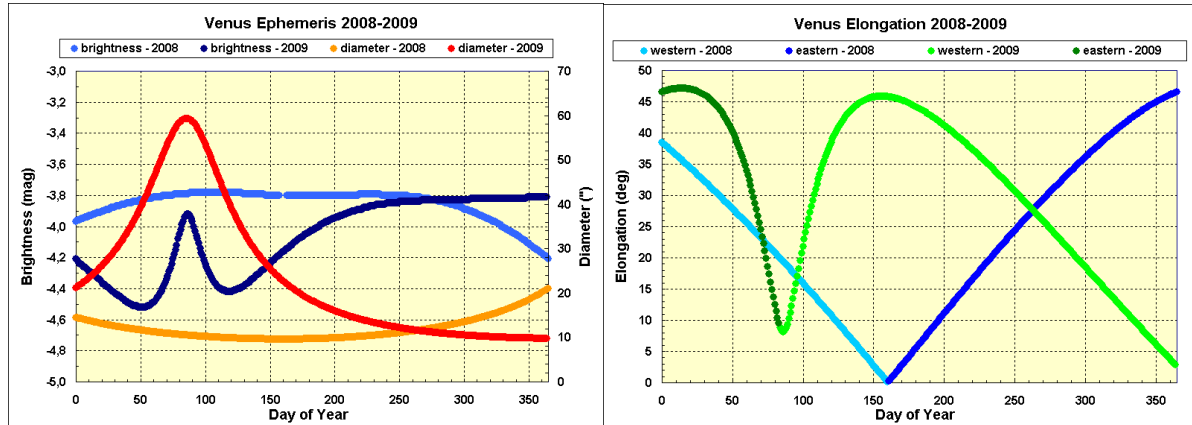


Figure 4-12: Left: Venus visual brightness and diameter in the years 2008 and 2009. Right: Venus elongation in the years 2008 and 2009. When the elongation refers to 'western' Venus leads the Sun ('morning star'), in the 'eastern' case it trails the Sun ('evening star').

As one of the two inner planets Venus can be found always in close vicinity of the Sun achieving a maximum angular distance of about 45° (fig. 4-12 right). Therefore observations with SCIAMACHY are only possible shortly before or after sunrise or close to the subsolar point. For our purpose the Solar Occultation & Calibration (SO&C) window was appropriate since it permits to actively control the Line-of-Sights (LoS) both in elevation and azimuth.

SCIAMACHY's limb Total Clear Field of View (TCFoV) measures spans azimuth angles from 316° to 44° (azimuth = 0° refers to the -Y axis of the platform, i.e. flight direction) and elevation angles 27.5° (just below the horizon) to 19.5° (altitude = 380 km). Venus had to appear in this range for being observable. Early 2009 Venus entered the TCFoV on the left side on the way to inferior conjunction. The planet was rapidly approaching the solar position at an azimuth angle of 325°. After inferior conjunction Venus moved further through the TCFoV to the right side and was visible until the end of

2009. In elevation direction Venus rose through the TCFoV in each orbit caused by the orbital motion of the spacecraft. To acquire a Venus signal undisturbed by the Earth's atmosphere the measurements had to start at a Venusian altitude of 100 km and ended 120 sec later when the planet reached the upper limit of the TCFoV. Venus could either rise prior or after the Sun. It was the preferred constellation to have Venus leading the Sun since then straylight was minimized. However this was only possible for a short period and measurements in that configuration could not always be accomplished.

Two dates, one in March 2009 and one in June 2009, were finally selected. The first date served to verify the implemented observation strategy and the second date was intended to yield the required data for the slit width calibration. Observation details can be found in table 4-2.

	March 20	June 25
Orbits	36873-36876	38261-38266
Venus brightness	-4.10	-4.07
Venus diameter	58.0"	19.5"
Venus altitude at start	100 km	100 km
Sun altitude at start	< 500 km	> 400 km

Table 4-2: Details of the SCIAMACHY Venus observations

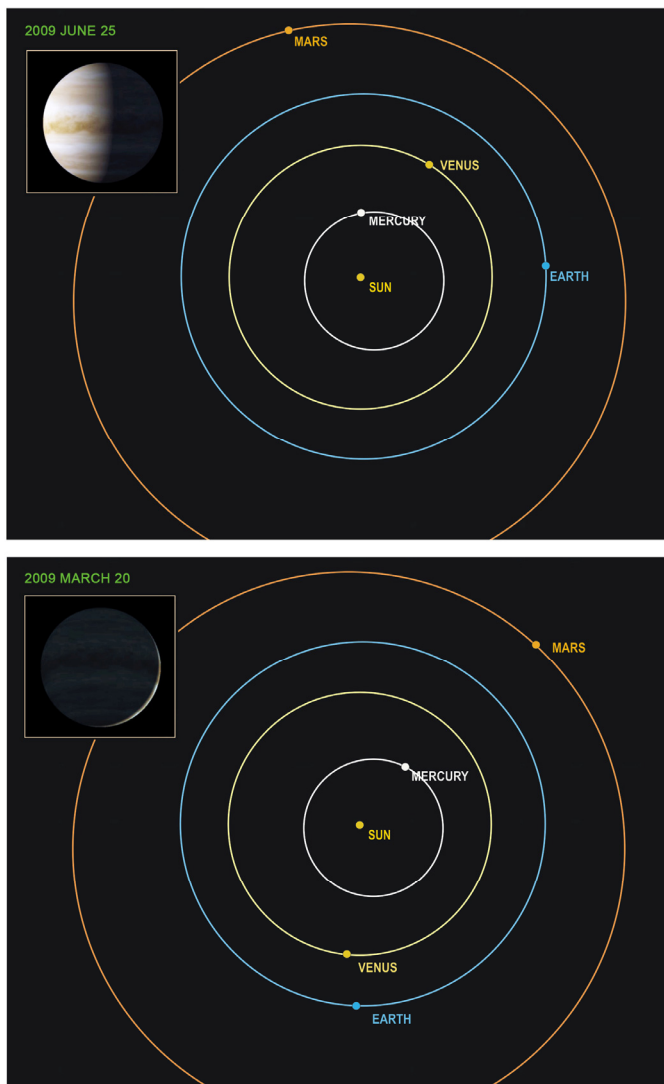


Figure 4-13: Constellations of Earth, Venus and Sun during the measurements in March and June. The illuminated part of Venus when viewed from Earth is shown in the insets.

The constellations of the inner planets are displayed in fig. 4-13. On 20th March 2009 Venus was only 7 days off inferior conjunction. Only a thin crescent of the illuminated Venusian disk could be seen from Earth. On 25th June 2009, Sun-Venus-Earth formed an almost right-angled triangle such that more than 50% of the sunlit disk was exposed to SCIAMACHY.

Measurements

Characterizing the slit in elevation required an elevation scan over Venus. Even at closest distance to Earth the apparent diameter of Venus (61") was smaller than the elevation extent of the I FoV (= slit). The specified width of the I FoV measures 1.8° in azimuth and 0.045° in elevation. In order to obtain a sufficiently high angular resolution, individual spectrometer readouts had to be acquired with an integration time of 1 sec .

March Observations

For the verification measurements in March a 'one-scan' approach was selected. At the time when Venus reached an altitude of 100 km the I FoV was placed with a margin $\Delta_{elev} = -0.040^\circ$ above the position of Venus. Venus was rising due to the spacecraft's orbital motion with an elevation rate amounting to $-0.0455^\circ/\text{sec}$. For the I FoV we commanded a slightly smaller elevation rate such that after 25 sec Venus had caught up with the I FoV and subsequently slowly overtook it. The Venus visibility time in the slit was estimated to be 50 sec with about 23 sec seeing the

disk unobscured by the edges of the slit. Total measurement duration of the corresponding state was 100 sec. This approach mimicked a downward scan of the slit over Venus.

The test measurement in March was required to verify the predicted channel dependent signal strength and the pointing accuracy both when acquiring Venus and when scanning over the planetary disk. Acquisition was particularly critical because of the known extra LoS mispointing together with the ENVISAT platform residual attitude errors in pitch, roll and yaw. These can be corrected a posteriori in data processing, if needed, but slightly degraded LoS pointing during measurement execution. In order to gain insight into the impact of the pointing accuracy 4 consecutive orbits with Venus observations were scheduled. In the first orbit on 20th March 2009, i.e. orbit 36873, the IFOV elevation angle and elevation rate was as described above. In the following 3 orbits the margin Δ_{elev} was increased and the IFOV elevation rate reduced accordingly. This ensured that Venus, although further away from the IFOV at the start of the observation, could still entirely cross the slit. In all 4 orbits Venus could be detected and the shapes of the recorded profiles were as expected (fig. 4-14 left). Only the profiles were not centered in the state which was attributed to the effect of the extra mispointing not being completely reflected in the commanded elevation angles. Additionally the thin crescent led to a shorter plateau of maximum signal.

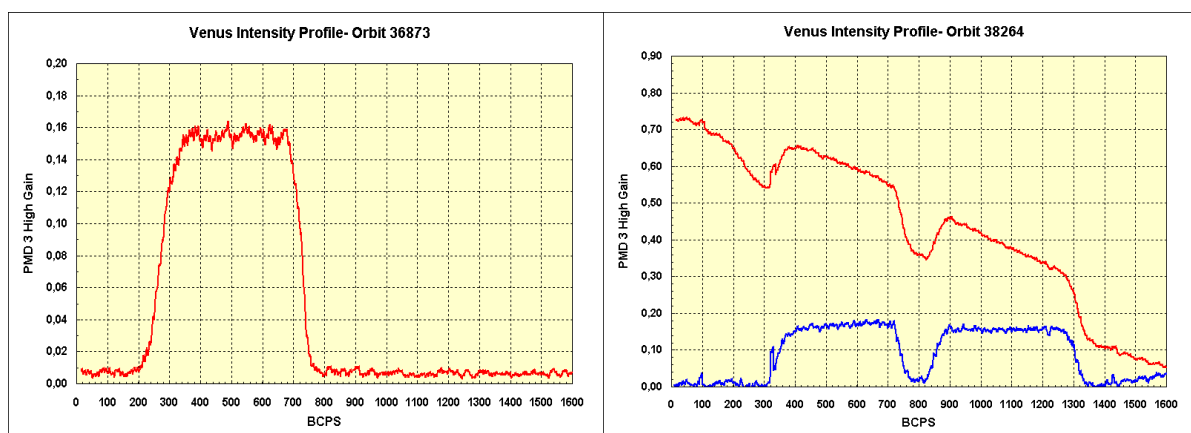


Figure 4-14: Left: Measured PMD 3 signal as a function of time (1 Broad Cast Pulse - BCPS = 0.0625 sec) in March. Venus entered the slit at about BCPS = 200 and left at about BCPS = 700. Right: Same as left panel but now from the measurements in June. In the red curve the straylight background is still present, in the blue graph its main contribution has been subtracted. The first scan over Venus is visible between BCPS = 300-800, the second between BCPS = 800-1350.

June Observations

The observation in June implemented a 'two-scan' approach. Now measurements started at a margin $\Delta_{\text{elev}} = -0.020^\circ$, i.e. closer to Venus at 100 km. Venus was rising at an azimuth angle nearer to flight direction such that the elevation rate was higher than in March. A slower IFOV elevation rate caused Venus to cross the slit lower boundary after 10 sec and 30 sec later Venus had passed the upper boundary. At 50 sec state elapsed time we commanded a faster IFOV elevation rate. Thus the IFOV caught up with Venus 10 sec later and passed it in another 30 sec. Measurements ended again 100 sec after state start. The IFOV motion now mimicked a downward scan followed by an upward scan. With the experience from the March observation we selected 6 consecutive orbits for scheduling a Venus timeline immediately after the routine Sun Occultation & Calibration (SO&C) measurement. The first three orbits, where the start of the Venus timeline was as calculated with the planning tools taking the known mispointings into account. These orbits were followed by two orbits where observing Venus occurred 1 sec earlier and one orbit where it was delayed by 1 sec. Such time shifts were introduced in case mispointing effects as observed in March would occur again. In 5 out of the 6 orbits Venus was detected. Due to the still persistent mispointing effect the first three orbits captured only a fraction of the two scans. In orbits 38264 and 38265 both scans were recorded as planned (fig. 4-14 right).

Results

The total duration with the Venusian disk filling completely the SCIAMACHY IFOV amounted to 60 sec in March and 165 sec in June. The recorded signals in the channels 1-6, averaged over all orbits of a sequence, are illustrated in fig. 4-15. In the SWIR channels 7 & 8 no significant spectrum was

detectable. Both observations produced spectra of similar strength. The larger distance of Venus in June was compensated by the much larger fraction of the sunlit planetary disk. Even the raw data of fig. 4-15 clearly show spectral features.

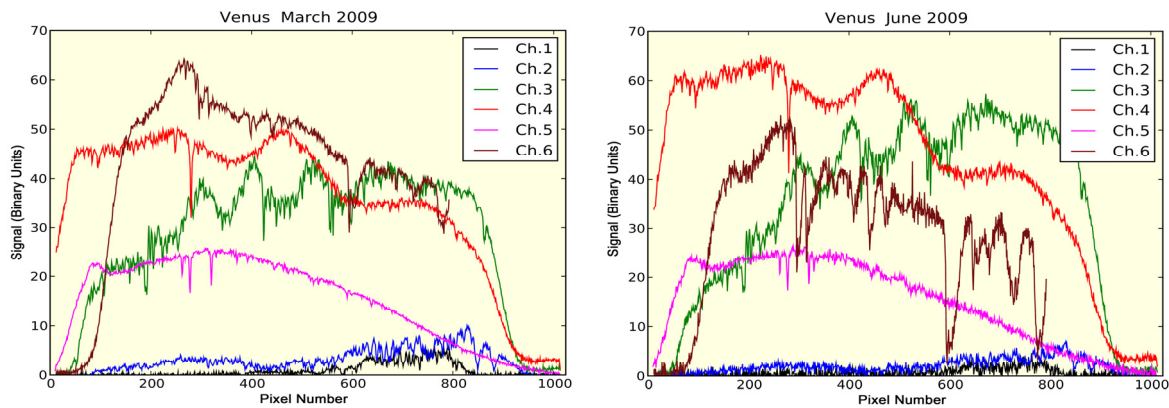


Fig. 4-15: Venus raw spectra in channels 1-6, measured with SCIAMACHY in March (left) and June (right).

Significant differences between the absorption features are obvious. In March they are less deep and sometimes at the detection limit. This difference is due to the observation geometries in March and June. In March SCIAMACHY captured light only from the limb of Venus. The LoS did not penetrate deep into the Venusian atmosphere. In June however a larger fraction of the illuminated disk was visible. This permitted the LoS to look deeper into the atmosphere.

SCIAMACHY's Venus science observations serve two purposes: Firstly they supplement close-up measurements by the instruments SPICAV (Spectroscopy for Investigation of Characteristics of the Atmosphere of Venus) and VIRTIS (Visible and Infrared Thermal Imaging Spectrometer) onboard ESA's Venus Express (VEX) mission. Since SCIAMACHY observes Venus under different illumination and viewing geometries than VEX does, it can also provide new information about the Venusian atmosphere. Secondly, and more important, they are another example of how the spectral signatures of a terrestrial planet might appear when viewed from far away. Since in 1995 the first planet around a solar-type star was discovered, finding an Earth-like planet around another star – a 'Second Earth' or 'Exo-Earth' – has become one of the big challenges in astronomy. Most of the currently known exoplanets are giant planets, like Jupiter. We hope that in the coming years, improved and dedicated instrumentation will bring smaller, terrestrial planets into reach such that their properties can be studied spectroscopically. Whether they might be suitable for harbouring life could be inferred from distinct spectral features. Appropriate interpretation of potential biomarkers requires experience gained in Solar System body test cases such as SCIAMACHY's Venus observations. Following the initial attempt in 1990 when the Galileo spacecraft on its way to Jupiter studied Earth's habitability several interplanetary probes have directed their sensors towards Earth, the 'pale blue dot'. The last in this series was VEX when VIRTIS acquired Earth spectra to 'search' for life on Earth, an undertaking just the opposite of our Venus measurements.

We modelled the expected spectrum from Venus based on the corresponding viewing geometries. The model comprised scattering by the main cloud layer (sulphuric acid – H_2SO_4) droplets and carbon dioxide (CO_2) absorption. For the June constellation a uniformly added component of 10 ppm of water vapour (H_2O) could be added. The resulting modelled spectra matched the observations quite well. Further details can be found in the next chapter which describes how the SCIAMACHY Venus data were studied using a radiative transfer model developed by IMF-AP.

References

DLR Press release: Die Venusatmosphäre im Blick – SCIAMACHY auf ENVISAT geht fremd, 17 July 2009, http://www.dlr.de/de/desktopdefault.aspx/tabid-1/86_read-18614/

ESA Press release: Earth observation goes planetary – SCIAMACHY observes Venus, 17 July 2009, http://www.esa.int/esaEO/SEMGFC7CTWF_index_0.html

4.5 Modelling the Venus Spectrum as Observed with SCIAMACHY

M. Vasquez, F. Schreier, M. Gottwald, S. Slijkhuis, E. Krieg (TwIG), S. Gimeno García, G. Lichtenberg

In the past year SCIAMACHY had successfully observed a quite unusual target for the Earth Observation mission ENVISAT. In March and June 2009 visible and near-infrared sunlight scattered and reflected from the atmosphere of our solar system neighbour Venus were acquired. Details of the SCIAMACHY Venus observations can be found in chapter 4.4. Here we concentrate on the interpretation of the spectra obtained. Particularly interesting were the viewing geometries which differed significantly on both dates. Since the March measurement saw Venus passing right between the Earth and the Sun we were observing the dark backside of Venus and only a very small part of the planet's atmosphere illuminated by sunlight. Thus, observing conditions mimicked a limb geometry. In June 2009 Venus was further away and more than 50% of its illuminated disk was exposed to SCIAMACHY. This corresponded much more to a nadir geometry.

The acquired March and June Venus spectra were simulated using a line-by-line radiative transfer model. Such modelled spectra are useful for better understanding of the Venus atmospheric composition and therefore for helping in the interpretation of the Venusian spectra as measured by SCIAMACHY. The atmosphere of Venus consists mainly of CO₂ (96.5%) and N₂ (3.5%), with thick sulfur dioxide and sulfuric acid clouds ranging from 50 to 70 km. These clouds reflect about 76% of the incident sunlight, i.e. only a small amount of sunlight penetrates further onto the surface. Thus the surface of Venus is usually obscured from regular imaging in the visible range.

GARLIC (Generic Atmospheric Radiation Line-by-line Infrared Code) is a versatile model that computes radiative transfer in a spherical atmosphere for up-, down-, and limb viewing geometries. Instrument effects relevant for remote sensing are modelled by convolution with appropriate spectral response and field-of-view functions. We used GARLIC for modelling the Venusian spectra with carbon dioxide (CO₂) concentrations for a 100 km atmospheric profile. Solar and observer zenith angles were calculated to meet the measuring geometries by considering the distances to Venus and the Sun at the time of observation. In order to simulate the illuminated area of the disk, Venus phase angle was first determined in order to obtain the fraction contributing to the amount of radiance received by SCIAMACHY. Reflecting clouds at different altitude levels were tested to match the simulated spectrum to the measured one.

Optically thick clouds, hardly penetrated by photons, can be considered as reflecting surfaces. Under these conditions, photon path lengths are directly related to the cloud top height: The lower the cloud, the longer the photon path lengths and the higher the probability for absorption events. Therefore, the depth of the absorption lines can be used as a proxy for the estimation of Venusian cloud top heights. The line depth of the modelled spectrum simulated better the observations from March when placing the cloud at an altitude of approximately 70 km. It is possible to notice the differences in the absorption lines depth of the spectra when using lower clouds below 65 km as it was expected. For the case of the data from June, the cloud altitude seems to be lower when compared to the March case. Then the modelled spectrum coincides with the observations when a reflecting cloud layer is assumed at an altitude between 60 and 65 km (see fig. 4-16).

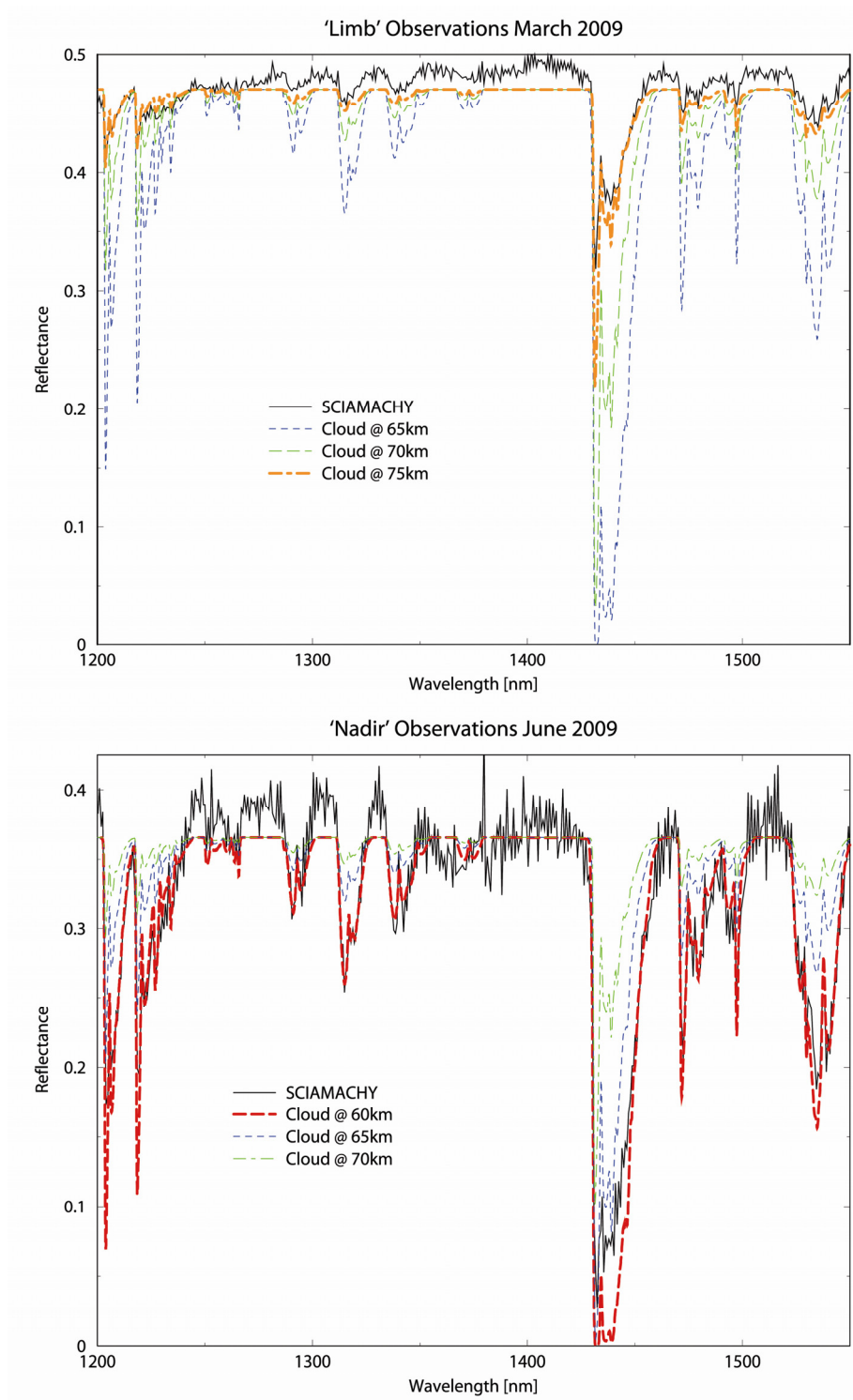


Fig. 4-16: Measured and modelled spectra from Venus in March (top) and June (bottom) 2009. The modelled spectra were tested by setting the clouds to different altitudes.

4.6 ECMWF Surface Pressure Quality Analysis and its Impact on Gravity Field Determination

E. Fagiolini, G. Schwarz (IMF-PB)

The Earth gravity field and its variations observed by gravity missions such as CHAMP, GRACE and GOCE, are closely interrelated with mass transport and mass distribution. Identification and separation of the relevant signals measured by the satellites and assimilation of complementary meteorological models are of main importance to achieve a consistent representation of the changing Earth. Due to orbit characteristics of the gravity field missions, the spatial sampling over a specific period of time, e.g. monthly, is not uniform. Therefore short-term mass variations, like high frequency mass variations in the atmosphere and in the oceans, have to be treated individually. This is known as 'de-aliasing' (Flechtner 2007). The monthly gravity fields, see solutions from GRACE, are e.g. corrected for atmospheric mass variations with frequencies from 6 hours (the highest resolution of present operational atmospheric models) to one year.

The atmospheric parameters required for the de-aliasing are extracted from global atmospheric models as provided by ECMWF, the European Centre for Medium Range Weather Forecasts (ECMWF 2009) or the National Centre for Environmental Prediction (NCEP) in the US. Until now atmospheric input parameters were assumed as being error-free but their uncertainties due, for example, to sparse data over the oceans, have some physical impact on the gravity field calculation. In particular, sensitivity analyses show that surface pressure uncertainties are an important source of geoid errors, whose effect, with respect to the GRACE baseline, is visible in GRACE error calculations.

The IDEAL-GRACE (Improving De-Aliasing for GRACE) project deals with the improvement of de-aliasing products by providing representative and realistic error measures for surface pressure data including, for the first time, their assumed uncertainties (i.e., their estimated standard deviations) so that geoid errors could be reduced. Therefore, quality and consistency analyses of surface pressure data and its standard deviations are performed. We concentrate here on ECMWF data that showed a better fit with in-situ observations (Salstein *et al.* 2008). Different meteorological models of error-scenarios from different meteorological models are currently investigated.

Time-tagged maps illustrate that surface pressure standard deviations strongly depend on location and time. Zonal transects show the impacts of continents and oceans. At higher elevations we have lower surface pressure and smaller standard deviations. High circumpolar circulation dynamics seem to be critical to data consistency (fig. 4-17).

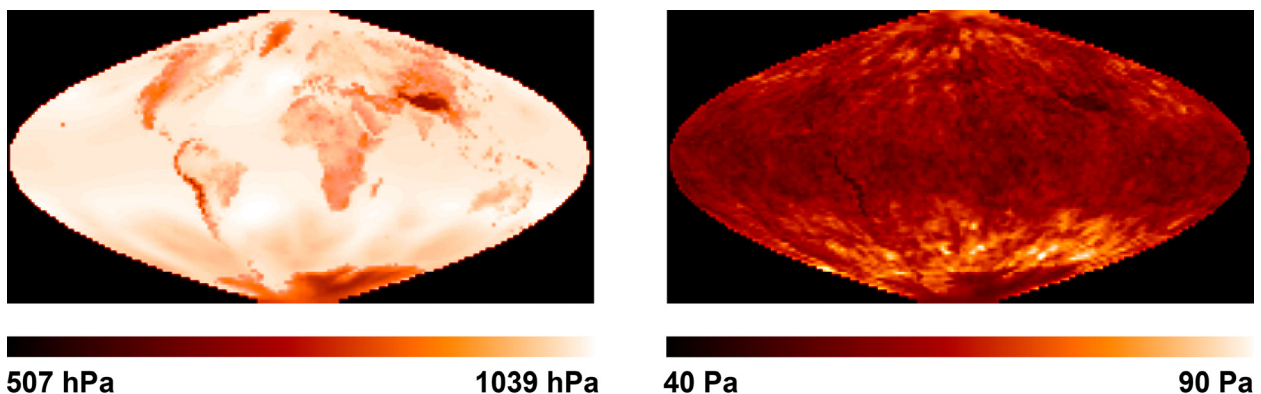


Fig. 4-17: The left panel displays a typical surface pressure while the right panel illustrates standard deviations

Global and sub-regional statistics of the standard deviations indicate their turbulent behaviour in time and space. The same result can be obtained by performing singular value decomposition analyses of adjacent data that, on the other hand, show a very regular behaviour of the surface pressure data being more homogeneous in space and time (see fig. 4-18).

Furthermore, when analyzing error-bar relationships signal dependent noise with negative slopes was sometimes observed (fig. 4-19). This is commonly an indication for insufficient quantization. With the help of land/sea masks provided by ECMWF, negative slopes were found only over water. This result

allowed us to define two classes ('water' and 'land') and to identify the 'water' class as the problematic one.

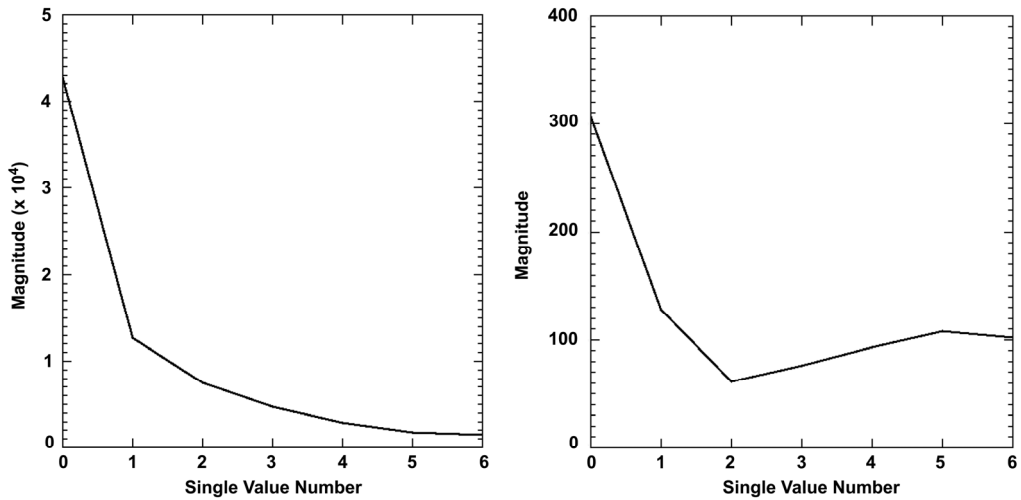


Fig. 4-18: Singular values of adjacent and distributed surface pressure data (left) and singular values of adjacent and distributed standard deviation data (right).

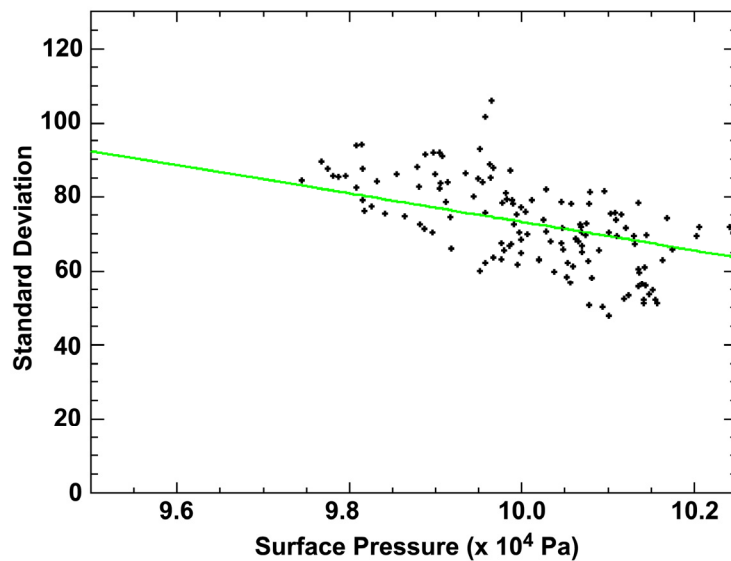


Fig. 4-19: Standard deviations versus surface pressure for a given geographical latitude (see fig. 4-24 above).

It has to be kept in mind that the ECMWF error-fields are pure results of the assimilation model and therefore might be too optimistic, but still have some impact on GRACE (Zenner *et al.* 2009). Therefore more investigations are needed to determine representative error parameters.

References

ECMWF: (2009) MARS User Guide. Technical Notes, p. 5, 2009

available under <http://www.ecmwf.int/publications/manuals/mars/guide/MarsUserGuide.pdf>

Flechtner, F.: AOD1B Product Description Document. GRACE Project Documentation, JPL 327-750, Rev. 1.0, JPL Pasadena, CA, 2007

Salstein, D.A., Ponte, R.M., and Cady-Pereira, K.: Uncertainties in atmospheric surface pressure fields from global analyses, *J. Geophys. Res.*, 113, D14107, doi:10.1029/2007JD009531, 2008

Zenner L., Gruber, T., Beutler, G., Jäggi, A., Flechtner, F., Schmidt, T., Wickert, J., Fagiolini, E., Schwarz, G., Trautmann, T.: Impact of Atmospheric Uncertainties on GRACE De-Aliasing and Gravity Field Models, to be published, 2009

5. Documentation

5.1 Books and Book Contributions

Loyola, D., T. Erbertseder, D. Balis, J.-C. Lambert, R. Spurr, M. Van Roozendael, P. Valks, W. Zimmer, J. Meyer-Arnek, C. Lerot: Operational Monitoring of the Antarctic Ozone Hole: Transition from GOME and SCIAMACHY to GOME-2. In: *Twenty Years of Ozone Decline*, Springer Publication, ISBN 978-90-481-2468-8, 2009

Rother, T.: *Electromagnetic wave scattering on nonspherical particles: basic methodology and simulations*. Springer Series in Optical Sciences, 145, ISBN 978 3 642 00703 3, 2009

Rother, T.: Green functions for plane wave scattering on single nonspherical particles. In: *Light Scattering Reviews*, 4, Springer, jointly published with Praxis Publishing, UK, 121-168, ISBN 978-3-540-74275-3, 2009

5.2 Journal Papers

Antón, M., D. Loyola, M. López, J.-M. Vilaplana, M. Bañón, W. Zimmer, C. Serrano: Comparison of GOME-2/MetOp total ozone data with Brewer spectroradiometer data over the Iberian Peninsula. *Annales Geophysicae*, 27, 1377-1386, 2009

Bierwirth, E, M. Wendisch, A. Ehrlich, B. Heese, M. Tesche, D. Althausen, A. Schladitz, D. Müller, S. Otto, T. Trautmann, T. Dinter, W. von Hoyningen-Huene, R. Kahn: Spectral surface albedo over Morocco and its impact on radiative forcing of Saharan dust. *TELLUS Series B – Chemical and Physical Meteorology*, 61(1), 252-269, DOI: 10.1111/j.1600-0889.2008.00395.x, 2009

Doicu, A., Trautmann, T.: Discrete-ordinate method with matrix exponential for a pseudo-spherical atmosphere: Scalar case. *Journal of Quantitative Spectroscopy and Radiative Transfer*, Volume 110(1-2), 146-158, 2009

Doicu, A., Trautmann, T.: Discrete-ordinate method with matrix exponential for a pseudo-spherical atmosphere: Vector case. *Journal of Quantitative Spectroscopy and Radiative Transfer*, 110(1-2), 159-172, 2009

Doicu, A., Trautmann, T.: Adjoint problem of radiative transfer for a pseudo-spherical atmosphere and general viewing geometries. *Journal of Quantitative Spectroscopy and Radiative Transfer*, 110(8), 464-476, 2009

Doicu, A., Trautmann, T.: Two linearization methods for atmospheric remote sensing. *Journal of Quantitative Spectroscopy and Radiative Transfer*, 110(8), 477-490, 2009

Doicu, A., Trautmann, T.: Picard iteration methods for a spherical atmosphere. *Journal of Quantitative Spectroscopy and Radiative Transfer*, 110(17), 1851-1863, 2009

Gottwald, M., von Savigny, C.: Exploration of noctilucent clouds in the polar mesosphere with SCIAMACHY. *Environmental Earth Sciences*, 59 (4), 949-950, DOI: 10.1007/s12665-009-0308-x, 2009

Lerot, C., van Roozendael, M., van Geffen, J., van Gent, J., Fayt, C., Spurr, R., Lichtenberg, G., von Barga, A.: Six years of total ozone column measurements from SCIAMACHY nadir observations. *Atmospheric Measurement Techniques*, 2(1), 87-98, 2009

Loyola, D., M. Coldewey-Egbers, M. Dameris, H. Garny, A. Stenke, M. Van Roozendael, C. Lerot, D. Balis, M. Koukoulis: Global long-term monitoring of the ozone layer - a prerequisite for predictions. *International Journal of Remote Sensing*, 30(15), 4295-4318, 2009

Loyola, D., E. Hilsenrath, J.S. Reid, G. Braathen: Introduction to the Issue on Fostering Applications of Earth Observations of the Atmosphere. *IEEE Journal of Selected Topics in Applied Earth Observations and Remote Sensing*, 2(3), 142-143, 2009

Otto, S., T. Trautmann: On a generalised G-function in radiative transfer theory of turbid vegetation media. *Meteorologische Arbeiten (XIV) und Jahresbericht 2008 des Instituts für Meteorologie der Universität Leipzig*, 45, 131-137, Selbstverlag, ISBN 978-3-9811114-5-3, 2009

Otto, S., E. Bierwirth, B. Weinzierl, K. Kandler, M. Esselborn, M. Tesche, A. Schladitz, M. Wendisch, T. Trautmann: Solar radiative effects of a Saharan dust plume observed during SAMUM assuming spheroidal model particles. *TELLUS Series B – Chemical and Physical Meteorology*, 61(1), 270-296, DOI: 10.1111/j.1600-0889.2008.00389.x, 2009

Rix, M., P. Valks, N. Hao, J. van Geffen, C. Clerbaux, L. Clarisse, P.-F. Coheur, D. Loyola, T. Erbertseder, W. Zimmer, S. Emmadi: Satellite Monitoring of Volcanic Sulfur Dioxide Emissions for Early Warning of Volcanic Hazards. *IEEE Journal of Selected Topics in Applied Earth Observations and Remote Sensing*, 2(3), 196-2006, 2009

Wauer, J., T. Rother: Considerations to Rayleigh's hypothesis. *Optics Communications*, 282, 339-350, DOI: 10.1016/j.optcom.2008.10.023, 2009

Schmidt, K., J. Wauer, T. Rother, T. Trautmann: Scattering database for spheroidal particles. *Applied Optics*, 48 (11) , 2154-2164, DOI: 10.1364/AO.48.002154, 2009

Schreier, F.: Comments on 'A Common Misunderstanding about the Voigt Line Profile'. *Journal of the Atmospheric Sciences*, 66(6), 1860-1864, DOI: 10.1175/2009JAS2906.1, 2009

Schreier, F.: CORRIGENDUM Comments on 'A Common Misunderstanding about the Voigt Line Profile'. *Journal of the Atmospheric Sciences*, 66(12), 3744-3745, DOI: 10.1175/2009JAS3303.1, 2009

Schymanski, E.L., M. Meringer, W. Brack: Matching structures to mass spectra using fragmentation patterns: are the results as good as they look? *Analytical Chemistry*, 81 (9), 3608-3617, ISSN 1520-6882, 2009

Theys, N., M. Van Roozendael, B. Dils, F. Hendrick, N. Hao, M. De Maziere: First satellite detection of volcanic bromine monoxide emission after the Kasatochi eruption. *Geophysical Research Letters*, 36 (L03809). DOI: 10.1029/2008GL036552, 2009

5.3 Conference Proceeding Papers and Presentations

Aberle, B., M. Coldewey-Egbers, S. Slijkhuis, P. Hoffmann, D. Loyola: The new GOME/ERS-2 Level 1 data with GDP_01 version 4. *ESA Atmospheric Science Conference, ESA SP-676, Barcelona, 2009*

Antón, M., M. Lopez, J. Vilaplana, D. Loyola, M. Kroon, R. McPeters, A. Serrano, M. Bañón, B. de la Morena: Performance of the Spanish Brewer Network assessed using satellite data from TOMS, GOME, OMI and GOME-2 instruments. *ESA Atmospheric Science Conference, ESA SP-676, Barcelona, 2009*

Antón M., M. López, D. Loyola, J.M. Vilaplana., M. Bañón, W. Zimmer, A. Serrano: Inter-comparison of total ozone column over the Iberian Peninsula: GOME/ERS2 and GOME-2/MetOp satellite observations versus Brewer measurements. *12th Biennial WMO-GAW Brewer Users Group Meeting, Rome, 2009*

Bovensmann, H., K.-U. Eichmann, S. Noel, A. Richter, M. Buchwitz, C. von Savigny, A. Rozanov, G. Lichtenberg, A. Doicu, F. Schreier, S. Hrechanyy, K. Kretschel, M. Meringer, M. Hess, M. Gottwald, A. Friker, S. Gimeno García, J.A.E. van Gijsel, L.G. Tilstra, R. Snel, C. Lerot, M. Van Roozendael, A. Dehn, H.

Förster, T. Fehr: Development of SCIAMACHY Operational ESA Level 2 Products towards Version 5 and Beyond. ESA Atmospheric Science Conference, ESA SP-676, Barcelona, 2009

Dehn, A., T. Fehr, F. Niro, L.S. de Miguel, G. Barrot, H. Bovensmann, M. Canela, R. Gessner, M. Gottwald, H. Laur, P. Lecomte, G. Perron, P. Raspollini: Calibration approaches and quality aspects for the ENVISAT Atmospheric Chemistry instruments. ESA Atmospheric Science Conference, ESA SP-676, Barcelona, 2009

Fagiolini, E: ECMWF Data Quality Analysis. Workshop on Atmospheric Effects in Space Geodesy. Vienna, 2009

Fagiolini, E., L. Zenner, F. Flechtner, T. Gruber, R. Rummel, T. Schmidt, G. Schwarz, D. Stammer, T. Trautmann, J. Wickert: Analysis of Uncertainties in Atmospheric Models & Impact on GRACE De-Aliasing. 3rd Workshop Massentransporte des SPP 1257, Eitorf, Germany, 2009

Fehr, T., G. Barrot, H. Bovensmann, M. Canela, A. Dehn, R. Gessner, M. Gottwald, H. Laur, F. Niro, G. Perron, P. Raspollini, L.S. de Miguel, ESA PLSO Team, GOMOS QWG, MIPAS QWG, SCIAMACHY QWG: Status of the ENVISAT Atmospheric Chemistry Mission. ESA Atmospheric Science Conference, ESA SP-676, Barcelona, 2009

Gimeno García, S., F. Schreier, G. Lichtenberg, S. Slijkhuis, B. Aberle: Carbon Monoxide and Methane Retrievals from SCIAMACHY Infrared Channels. ESA Atmospheric Science Conference, ESA SP-676, Barcelona, 2009

Gimeno García, S., T. Trautmann, V. Venema: Radiative Transfer in highly variable cloud scenarios. ESA Atmospheric Science Conference, ESA SP-676, Barcelona, 2009

Gottwald, M., E. Krieg, G. Lichtenberg, S. Noel, K. Bramstedt, H. Bovensmann, R. Snel: SCIAMACHY Instrument Status - from 2009 to 2013. ESA Atmospheric Science Conference, ESA SP-676, Barcelona, 2009

Gottwald, M., E. Krieg, K. Reissig, J. How, A. Dehn, T. Fehr, A. Bucarelli: The SCIAMACHY Consolidated Level 0 Master Archive. ESA Atmospheric Science Conference, ESA SP-676, Barcelona, 2009

Gottwald, M., S. Slijkhuis, E. Krieg, F. Schreier, G. Lichtenberg, M. Vasquez, R. Snel, D. Stam, R. de Kok: Venus Observations with SCIAMACHY. ESA Atmospheric Science Conference, ESA SP-676, Barcelona, 2009

Gottwald, M.: Heimat Erde - das Bild unseres Planeten. Public lecture, Rosenheim, April 27, 2009

Gottwald, M.: Heimat Erde - das Bild unseres Planeten. Public lecture, Augsburg, Mai 7, 2009

Gottwald, M.: Die Kartierung des Mondes - 400 Jahre Selenografie. Public lecture, Munich, July 3, 2009

Gottwald, M.: Die Kartierung des Mondes - 400 Jahre Selenografie. Public lecture, Trebur, June 19, 2009

Gottwald, M.: Das Bild unseres Planeten. Public lecture, Wasserburg, October 23, 2009

Gottwald, M.: Das Bild unserer Erde. Public lecture, Neumarkt, Oktober 2, 2009

de Miguel, L.S., A. Dehn, T. Fehr, F. Niro, G. Barrot, H. Bovensmann, M. Canela, R. Gessner, M. Gottwald, H. Laur, P. Lecomte, G. Perron, P. Raspollini: The ENVISAT Atmospheric Chemistry missions: monitoring status and evolution. ESA Atmospheric Science Conference, ESA SP-676, Barcelona, 2009

Hao, N., P. Valks, D. Loyola, J.-C. Lambert, G. Pinardi, M. Van Roozendaal, N. Theys: GOME-2 observations of ozone and minor trace gases. MOCA 2009, Montréal, Canada, 2009

Hao, N., P. Valks, D. Loyola, M. Rix, W. Zimmer, S. Emmadi: Air quality measurements during the 2008 Olympic Games from the GOME-2 instrument on MetOp. ESA Atmospheric Science Conference, ESA SP-676, Barcelona, 2009

Hao, N., P. Valks, M. Rix, D. Loyola, M. Van Roozendael, W. Zimmer, S. Emmadi: Two years of GOME-2 ozone and minor trace gas measurements. 11th International Conference on Atmospheric Sciences and Applications to Air Quality, Jinan, China, 2009

Hao, N., P. Valks, M. Rix, M. Van Roozendael, J. Van Geffen, D. Loyola: SO₂ over China detected with GOME-2 instrument. AT-2 Follow Up Workshop, Mainz, 2009

de Kloe, J., A. Stoffelen, G.J. Marseille, D. Tan, L. Isaksen, C. Desportes, C. Payan, A. Dabas, D. Huber, O. Reitebuch, P. Flamant, H. Nett, O. LeRille, A.-G. Straume: ADM-Aeolus ocean surface calibration and Level-2B processing. International Symposium on Tropospheric Profiling, Delft, The Netherlands, 2009

Koehler, C.H., T. Trautmann, E. Lindermeir: Measurement of mixed biomass burning and mineral dust aerosol in the thermal infrared. International Radiation Symposium (IRC/IAMAS), Foz do Iguacu, Brazil, Current Problems in Atmospheric Radiation – IRS 2008, 1100, 169-172, 2009

Koukouli, M., J.-C. Lambert, D. Balis, D. Loyola, M. Van Roozendael, C. Lerot, J. Granville, W. Zimmer: Validation of different configurations of the GODFIT/GDP5 algorithm using ground-based total ozone data. ESA Atmospheric Science Conference, ESA SP-676, Barcelona, 2009

Lichtenberg, G., S. Gimeno-Garcia, F. Schreier, S. Slijkhuis, R. Snel, R. van Hees, P. van der Meer: Impact of Level 1 quality on BIRRA CO retrieval. ESA Atmospheric Science Conference, ESA SP-676, Barcelona, 2009

Loyola, D., M. Coldewey-Egbers, W. Zimmer, C. Lerot, M. Van Roozendael, M. Dameris, M. Koukouli, D. Balis: Total Ozone Trends Derived from the 14-Year Combined GOME/SCIAMACHY/GOME-2 Satellite Data Record. ESA Atmospheric Science Conference, ESA SP-676, Barcelona, 2009

Meringer, M.: Mathematik im Einsatz für die Umwelt. 4. Tag der Mathematik, Bayreuth, 2009

Niro, F., A. Dehn, L.S. de Miguel, T. Fehr, H. Laur, P. Lecomte, M. Canela, R. Gessner, G. Perron, P. Raspollini, G. Barrot, H. Bovensmann, M. Gottwald: Seven years of data quality of the ENVISAT Atmospheric Chemistry missions: highlights, lessons learned and perspectives. ESA Atmospheric Science Conference, ESA SP-676, Barcelona, 2009

Noël, S., K. Bramstedt, H. Bovensmann, J.P. Burrows, M. Gottwald, E. Krieg: Long-Term Radiometric Performance of the SCIAMACHY Quartz Tungsten Halogen Lamp. EGU General Assembly, Vienna, 2009

Pflug B., B. Aberle, D. Loyola: Validation of spectral surface albedo derived from GOME-2/MetOp measurements. EUMETSAT Meteorological Satellite Conference, Bath, United Kingdom, 2009

Rix, M., P. Valks, J. van Geffen, C. Maerker, K. Seidenberger, T. Erbertseder, N. Hao, M. Van Roozendael, D. Loyola: Operational monitoring of SO₂ emissions using the GOME-2 satellite instrument. EUMETSAT Meteorological Satellite Conference, Bath, United Kingdom, 2009

Rix, M., P. Valks, J. van Geffen, C. Maerker, K. Seidenberger, T. Erbertseder, N. Hao, D. Loyola, M. Van Roozendael: Operational monitoring of SO₂ emissions using the GOME-2 satellite instrument. ESA Atmospheric Science Conference, ESA SP-676, Barcelona, 2009

Rix, M., J. van Geffen, P. Valks: Monitoring of volcanic SO₂ emissions using satellite instruments. GlobVolcano User Workshop 2009, San Jose, Costa Rica, 2009

Rix, M., C. Maerker, P. Valks, T. Erbertseder, K. Seidenberger: Monitoring volcanic SO₂ plumes using the GOME-2 satellite instrument. 2. Statusseminar: EWS - Frühwarnsysteme gegen Naturgefahren. Munich, 2009

Rix, M., P. Valks, N. Hao, T. Erbertseder: Monitoring of volcanic SO₂ emissions using the GOME-2 satellite instrument. EGU General Assembly, Vienna, 2009

Schreier, F., M. Szopa, A. Doicu, S. Gimeno García, C. Böckmann, P. Hoffmann: First Results of Atmospheric Composition Retrieval using IASI-METOP and AIRS-AQUA Data. 2nd EPS/MetOp RAO Workshop, ESA SP-675, Barcelona, 2009

Schreier, F., S. Gimeno García, M. Hess, A. Doicu, G. Lichtenberg: Carbon Monoxide Vertical Column Density Retrieval from SCIAMACHY Infrared Nadir Observations. International Radiation Symposium (IRC/IAMAS), Foz do Iguacu, Brazil, Current Problems in Atmospheric Radiation – IRS 2008, 1100, 327-330, 2009

Schreier, F., S. Gimeno García, G. Lichtenberg, P. Hoffmann: Intercomparison of Carbon Monoxide Retrievals from SCIAMACHY and AIRS Nadir Observations. ESA Atmospheric Science Conference, ESA SP-676, Barcelona, 2009

Schüssler, O., D. Loyola, A. Doicu: Constrained regularization methods for ozone profile retrieval from UV/VIS nadir spectrometers. ESA Atmospheric Science Conference, ESA SP-676, Barcelona, 2009

Slijkhuis, S., S. Beirle, N. Kalakoski, K. Mies, S. Noël, J. Schulz, T. Wagner: Comparison of H₂O retrievals from GOME and GOME-2. EUMETSAT Meteorological Satellite Conference, Bath, United Kingdom, 2009

De Smedt I., J. Stavrakou, J.F. Muller, M. Van Roozendael, D. Loyola, N. Hao, P. Valks: HCHO columns retrieved from GOME-2: first scientific results and progress towards the development of an operational product. EUMETSAT Meteorological Satellite Conference, Bath, United Kingdom, 2009

Spurr, R., W. Zimmer, D. Loyola, M. Coldewey-Egbers, C. Lerot, M. Van Roozendael, J.-C. Lambert, J. Granville, M. Koukouli, D. Balis: Clouds as Scattering Layers: Improved Retrieval of GOME-2 Total Column Products. EUMETSAT Meteorological Satellite Conference, Bath, United Kingdom, 2009

Valks, P., N. Hao, M. Rix, J.-C. Lambert, G. Pinardi, M. Van Roozendael, J. van Geffen, N. Theys, D. Loyola: Operational O3M-SAF trace gas column products: GOME-2 tropospheric NO₂, SO₂ and BrO. EGU General Assembly, Vienna, 2009

Valks, P., N. Hao, D. Loyola, M. Van Roozendael, J.-C. Lambert, G. Pinardi, W. Zimmer, S. Emmadi: GOME-2 total and tropospheric NO₂ products. O3M-SAF User and Algorithm Forum, Halkidiki, 2009

Valks, P., N. Hao, D. Loyola, M. Van Roozendael, J. Van Gent, W. Zimmer and S. Emmadi: Investigations for an improved GOME-2 total ozone algorithm. O3M-SAF User and Algorithm Forum, Halkidiki, 2009

Valks, P., N. Hao, M. Rix, T. Erbertseder, D. Loyola, J.-C. Lambert, G. Pinardi, M. Van Roozendael, J. Van Geffen: Tropospheric NO₂ and SO₂ Retrievals from GOME-2 Measurements. Atmospheric Composition Constellation Workshop on Air Quality (ACC-4), ESA-ESRIN, Frascati, 2009

Valks, P., N. Hao, M. Rix, J.-C. Lambert, G. Pinardi, M. Van Roozendael, N. Theys, J. van Geffen, D. Loyola: Operational GOME-2 trace gas column measurements of NO₂, BrO and SO₂. ESA Atmospheric Science Conference, ESA SP-676, Barcelona, 2009

Valks, P., N. Hao, J.-C. Lambert, D. Loyola, G. Pinardi, M. Rix, M. Van Roozendael, N. Theys, I. De Smedt, W. Zimmer, S. Emmadi: The O3M-SAF minor trace-gas column products: GOME-2 NO₂, BrO, SO₂ and H₂CO. EUMETSAT Meteorological Satellite Conference, Bath, United Kingdom, 2009

Van Roozendael, M., D. Loyola, R. Spurr, C. Lerot, D. Balis, M. Koukouli, J.-C. Lambert, J. van Gent, J. Granville, W. Zimmer, S. Otto, A. Doicu: GDP 5.0 – Improved Total Ozone Columns from GOME based on the GODFIT Algorithm. ESA Atmospheric Science Conference, ESA SP-676, Barcelona, 2009

Vasquez, M., F. Schreier, M. Gottwald, S. Slijkhuis, E. Krieg, G. Lichtenberg: Venus Modeled Spectrum and Observations with SCIAMACHY, Pathways towards habitable planets, Barcelona, 2009

Wauer, J. T. Rother, K. Schmidt: Scattering data base for nonspherical particles, European Aerosol Conference, Karlsruhe, 2009

Zenner, L., T. Gruber, G. Beutler, A. Jäggi, F. Flechtner, T. Schmidt, E. Fagiolini, G. Schwarz, T. Trautmann: Impact of Atmospheric Uncertainties on GRACE De-Aliasing and Gravity Field Models. International Association of Geodesy Scientific Assembly, Buenos Aires, Argentina, 2009

5.4 Attended Conferences and Professional Leaves

European Geoscience Union General Assembly, Vienna, Austria, April 20-24, 2009

11th International Conference on Atmospheric Sciences and Applications to Air Quality, Jinan, China, April 21-23, 2009

2nd EPS-Metop Research Announcement of Opportunity Workshop, Barcelona, Spain, May 20-22, 2009

2nd Helmholtz Alliance Week *Planetary Evolution and Life*, Berlin, Germany, June 2-5, 2009

15th Conference on the Middle Atmosphere, American Meteorological Society, Stowe, VT, United States, June 8-12, 2009

AT-2 Follow Up Workshop, Mainz, June 22/23, 2009

3rd Workshop of DFG Schwerpunktprogramm 1257 (Massentransporte und Massenverteilung im Erdsystem), Eitorf, Germany, June 30, 2009

GlobVolcano User Workshop 2009, San Jose, Costa Rica, July 7/8, 2009

4. Tag der Mathematik, Bayreuth, Germany, July 11, 2009

MOCA 2009, Joint Assembly, Montréal, Canada, July 19-24, 2009

Summer School Alpbach 2009: Exoplanets, July 21-30, 2009

European Aerosol Conference, Karlsruhe, September 6-11, 2009

ESA Atmospheric Science Conference, Barcelona, Spain, September 7-11, 2009

Pathways towards habitable planets, Barcelona, Spain, September 14-18, 2009

EUMETSAT Meteorological Satellite Conference, Bath, United Kingdom, September 21-25, 2009

Helmholtz Alliance *Planetary Evolution and Life*: Life Symposium, Berlin, Germany, September 28-29, 2009

2nd Statusseminar Geotechnologien (EWS – Frühwarnsysteme gegen Naturgefahren), Munich, Germany, October 12-13, 2009

International Symposium on Tropospheric Profiling, Delft, The Netherlands, October 18-23, 2009

Workshop on Atmospheric Effects in Space Geodesy. Vienna, Austria, November 12, 2009

5th Atmospheric Limb Conference, Helsinki, Finland, November 16-19, 2009

5.5 Diploma and Doctoral Theses

Fagiolini, E.: The impact of atmospheric variability on the determination of the gravity field of the Earth. Dissertation, Faculty of Civil Engineering and Geodesy, Technical University of Munich. (Supervisors: Prof. Dr. Reiner Rummel, Technical University of Munich and Gottfried Schwarz)

Gimeno-García, S.: Simulation of solar radiative transfer and comparison with spectro-radiometric measurements. Dissertation, Faculty of Physics and Earth Science, University of Leipzig. (Supervisor: Prof. Dr. Thomas Trautmann)

Köhler, C.H.: Observation and simulation of the longwave radiative effects for Saharan mineral dust plumes. Dissertation, Faculty of Physics, Mathematics and Computer Science, Johannes Gutenberg University of Mainz. (Supervisors: Prof. Dr. Manfred Wendisch, Johannes Gutenberg University of Mainz and Prof. Dr. Thomas Trautmann)

Otto, S.: Optische Eigenschaften von Saharamineralstaub und dessen klimarelevanter Einfluss auf den Strahlungstransport in der Erdatmosphäre. Dissertation (Supervisor: Prof. Dr. Thomas Trautmann)

Rix, M.: Observation of volcanic SO₂ plumes based on the satellite-borne GOME-2 instrument. Dissertation, Faculty of Civil Engineering and Geodesy, Technical University of Munich. (Supervisors: Prof. Dr. Richard Bamler, Technical University of Munich and Dr. Pieter Valks)

Schüssler, O.: Constrained regularization methods for ozone profile retrieval from UVVIS nadir spectrometers. Master of Science Thesis, Technical University Munich, Earth Oriented Space Science and Technology (ESPACE) Master Program, October 2009. (Supervisors: Dr. Adrian Doicu and Diego Loyola)

Szopa, M.: Inversion methods for atmospheric nadir infrared sounding. Dissertation, Faculty for Mathematics and Science, University of Potsdam. (Supervisors: Prof. Dr. Christine Böckmann, University of Potsdam and Dr. Adrian Doicu)

Tröller, A.: Theoretical and numerical aspects of the Rayleigh hypothesis related to scattering on non-spherical particles. Diploma Thesis, Faculty of Physics and Earth Science, University of Leipzig, September 2009. (Supervisors: Prof. Dr. T. Trautmann and Dr. habil. Tom Rother)

Vasquez, M.: Simulation of the radiation field in planetary atmospheres. Dissertation, Centre of Astronomy and Astrophysics, Technical University of Berlin. (Supervisors: Prof. Dr. Heike Rauer, German Aerospace Center, Institute of Planetary Research and Dr. Franz Schreier)

Xu, J.: Optimization of radiative transfer modeling for far infrared remote sensing. Master of Science Thesis, Technical University Munich, Earth Oriented Space Science and Technology (ESPACE) Master Program, November 2009. (Supervisors: Dr. Adrian Doicu, Dr. Franz Schreier, and Prof. Dr. Thomas Trautmann)

Abbreviations and Acronyms

ACE	Aerosol Characterisation Experiment
AD	Automatic Differentiation
ADF	Auxiliary Data File
AIRS	Atmospheric Infrared Sounder
AMC-DOAS	Air Mass Corrected DOAS
AOCS	Attitude and Orbit Control System
AP	Atmospheric Processors
ARM	Atmospheric Radiation Measurement
ASM	Azimuth Scan Mechanism
ATOVS	Advanced TIROS Operational Vertical Sounder
BIRA-IASB	Belgisch Instituut voor Ruimte-Aëronomie Institut d' Aëronomie Spatiale de Belgique
BIRRA	Better InfraRed Retrieval Algorithm
BU	Binary Unit
CCA	Communication Area
CCW	Counterclockwise
CEOS	Committee for Earth Observation Satellites
CERVISA	Column Estimator Vertical Infrared Sounding
CFI	Customer Furnished Item
CHAMP	Challenging Mini-Satellite Payload
CKD	Correlated K-Distribution
CLO	Consolidated Level 0
CRM	Cloud Resolving Model
CW	Clockwise
DAK	Double-Adding code KNMI
DBPM	Dead and Bad Pixel Mask
DFD	Deutsches Fernerkundungsdatenzentrum
DIMS	Data & Information Management System
DLR	Deutsches Zentrum für Luft- und Raumfahrt
DOAS	Differential Optical Absorption Spectroscopy
DRACULA	Advanced Retrieval of the Atmosphere with Constrained and Unconstrained Least-Squares Algorithms
ECMWF	European Centre for Medium-Range Weather Forecasts
ENVISAT	Environmental Satellite
EOS	Earth Observing System
ERS	European Remote Sensing Satellite
ESA	European Space Agency
ESA/DUE	ESA Data User Element
ESM	Elevation Scan Mechanism
ESOC	European Space Operation Center
ESRIN	European Space Research Institute
ESTEC	European Space Technology Center
EUMETSAT	European Organisation for the Exploitation of Meteorological Satellites
EV	Experimentelle Verfahren
FASCODE	Fast Atmosphere Signature Code
FMI	Finnish Meteorological Institute
FTIR	Fourier Transform Infrared Spectrometer
FZK-IMK	Forschungszentrum Karlsruhe – Institut für Meteorologie und Klimaforschung
GARLIC	Generic Atmospheric Radiation Line-by-Line Infrared Code
GDP	GOME Data Processor
GEOMON	Global Earth Observation and Monitoring
GMES	Global Monitoring for Environment and Security

GOES	Geostationary Operational Environmental Satellites
GOME	Global Ozone Monitoring Experiment
GPS	Global Positioning System
GRACE	Gravity Recovery and Climate Experiment
HDF	Hierarchical Data Format
IASI	Infrared Atmospheric Sounding Interferometer
IDEAL-GRACE	Improving De-Aliasing for GRACE
IFoV	Instantaneous Field of View
IFU	Institut für Umweltphysik
IMF	Institut für Methodik der Fernerkundung
IPA	Independent Pixel Approximation
IRGN	Iteratively Regularised Gauss-Newton
ISS	International Space Station
IUP-IFE	Institut für Umweltphysik / Institut für Fernerkundung
IVP	Initial Value Problem
IR	Infrared
KNMI	Koninklijk Nederlands Meteorologisch Instituut
LED	Light Emitting Diode
LIDAR	Light Detection and Ranging
LIDORT	Linearized Discrete Ordinate Radiative Transfer
LoS	Line of Sight
MAERI	Marine Atmospheric Emitted Radiance Interferometer
MCMD	Macrocommand
MERIS	Medium Resolution Imaging Spectrometer
MetOp	Meteorological Operational Polar Satellites of EUMETSAT
MIPAS	Michelson Interferometer for Passive Atmospheric Sounding
MIRART	Modular Infrared Atmospheric Radiative Transfer
MLST	Mean Local Solar Time
MO&C	Moon Occultation and Calibration
MoCaRT	Monte Carlo Radiative Transfer
MOD	Merged Ozone Data
MODIS	Moderate Resolution Imaging Spectroradiometer
MOPITT	Measurements of Pollution in the Troposphere
MPO	Meteorology and Physical Oceanography
MSG	METEOSAT Second Generation
NASA	National Aeronautics and Space Administration
NCEP	National Centers for Environmental Prediction
NDACC	Network for the Detection of Atmospheric Composition Change
NIR	Near Infrared
NIST	National Institute of Standards and Technology
NIVR	Nederlands Instituut voor Vliegtuigontwikkeling en Ruimtevaart
NLC	Noctilucent Cloud
NNT	Non-Nominal Telemetry
O3M	Ozone Monitoring
OCM	Orbit Control Manoeuvre
OCR	Operation Change Request
OCRA	Optical Cloud recognition Algorithm
OHP	Observatorium Hoenpeissenberg
OMI	Ozone Monitoring Instrument
ORR	Operational Readiness Review
PDS	Payload Data Segment
PILS	Profile Inversion for Limb Sounding
PIRATES	Programmer's Interface to Radiative Transfer Algorithms
PMD	Polarization Measurement Device
PPG	Pixel to Pixel Gain
PROMOTE	Protocol Monitoring for the GMES Service Element
PSC	Polar Stratospheric Cloud

QBO	Quasi-Biennial Oscillation
RAL	Rutherford Appleton Laboratory
ROCINN	Retrieval of Cloud Information by a Neural Network
RRS LIDORT	Rotational Raman Scattering LIDORT
RSMAS	Rosenstiel School of Marine and Atmospheric Science
RT	Radiative Transfer
SAA	South Atlantic Anomaly
SACS	Support to Aviation Control Service
SAF	Satellite Application Facility
SAMUM	Sahara Mineral Dust Experiment
SBUV	Solar Backscatter Ultraviolet Instrument
SCIAMACHY	Scanning Imaging Absorption Spectrometer for Atmospheric Chartography
SCD	Slant Column Density
SEVIRI	Spinning Enhanced Visible and Infrared Imager
SGP	Southern Great Plains
SMILES	Superconducting-Submillimeter-Wave Limb-Emission Sounder
SMR	Sun Mean Reference
SNR	Signal-to-Noise Ratio
SO&C	Sun Occultation and Calibration
SOST	SCIAMACHY Operations Support Team
SQWG	SCIAMACHY Quality Working Group
SRON	Netherlands Institute for Space Research
SSM/I	Special Sensor Microwave Imager
SWIR	Short Wave Infrared
YSM	Stellar Yaw Steering Mode
TCFoV	Total Clear Field of View
TELIS	TeraHertz Limb Sounder
TES	Thermal Emission Spectrometer
TOMS	Total Ozone Mapping Spectrometer
TOVS	TIROS Operational Vertical Sounder
UFS	Umweltforschungsstation Schneefernerhaus
UPAS	Universal Processor for Atmospheric Spectrometers
UV	Ultraviolet
VCD	Vertical Column Density
VIS	Visual
VISSR	Visible and Infrared Spin Scan Radiometer
VOC	Volatile Organic Compound
WGCV	Working Group on Calibration and Validation

DLR at a Glance

DLR is Germany's national research center for aeronautics and space. Its extensive research and development work is integrated into national and international cooperative ventures. As Germany's space agency, DLR has been given responsibility for the forward planning and the implementation of the German space program by the German federal government as well as for the international representation of German interests. Furthermore, Germany's largest project-management agency is also part of DLR.

Approximately 5,700 people are employed at thirteen locations in Germany: Köln (headquarters), Berlin, Bonn, Braunschweig, Bremen, Göttingen, Hamburg, Lampoldshausen, Neustrelitz, Oberpfaffenhofen, Stuttgart, Trauen and Weilheim. DLR also operates offices in Brussels, Paris, and Washington, D.C.

Remote Sensing Technology Institute Institut für Methodik der Fernerkundung

DLR's Remote Sensing Technology Institute (IMF) is located in Oberpfaffenhofen, Berlin-Adlershof, and Neustrelitz.

IMF carries out research and development for retrieving geo-information from remote sensing data. It conducts basic research on physical principles of remote sensing and develops algorithms, techniques, and operational processing systems for synthetic aperture radar, optical remote sensing, and spectrometric sounding of the atmosphere. The processing systems are in operational use for national, European, and international Earth observation missions.

For preparation and in support of spaceborne missions IMF operates a suite of multi- and hyperspectral optical airborne sensors. The institute contributes its expertise to novel sensor and mission concepts.

The German Remote Sensing Data Center (DFD) and IMF form DLR's Applied Remote Sensing Cluster (C-AF).



DLR

**Deutsches Zentrum
für Luft- und Raumfahrt e.V.**

in der Helmholtz-Gemeinschaft

Institut für Methodik der Fernerkundung

Oberpfaffenhofen
82234 Weßling

www.dlr.de/caf